

# Supramolecular Network Formation From Solution-based Deposition Techniques

**GEORGE GREEN LIBRARY OF  
SCIENCE AND ENGINEERING**

James Christopher Russell, MSci (Hons)

Thesis submitted to the University of Nottingham  
for the degree of Doctor of Philosophy

June 1, 2011

## Abstract

The spontaneous formation of supramolecular assemblies has been viewed as a potential route to the creation of functional nano-scale architectures for a number applications in electronics. In this thesis a number of assemblies formed from molecular constituents deposited from the solution phase have been studied.

The structures formed by two carboxylic acid derivatives on the highly oriented pyrolytic graphite (HOPG) surface from nonanoic acid solutions are presented. Quaterphenyl-tetracarboxylic acid (QPTC) molecules are observed to form a supramolecular network where all the constituents lay parallel to one another on the surface. The network is stabilised by four carboxylic acid dimer bonds per molecule in addition to admolecule-substrate interactions. Terphenyl-tetracarboxylic acid (TPTC) molecules form a much more complex structure with individuals orientating themselves in one of three directions to form a network with hexagonal symmetry but no translational order. To characterise such an unusual supramolecular morphology we introduce a rhombus tiling representation of the network where each molecule is schematically replaced with a lozenge rhombus producing a tiling. Such tilings have been studied previously in the literature and utilising this we are able to determine that the morphology is stabilised by entropic contributions to the free energy. In addition to this we present the tip-induced manipulation of the TPTC supramolecular network. The manipulation is performed by imaging the structure within a specific voltage bias range resulting the TPTC molecules reordering into a close packed structure. Returning the voltage to that conventional used for imaging causes the network to relax back into the open structure although with a different morphology.

We then discuss the changes induced in these supramolecular networks when additional molecular species are introduced to the system. First, coronene and perylene are separately codeposited with QPTC resulting in the formation of a hexagonally ordered network with coronene or perylene located at the vertices of six QPTC molecules. This new structure is observed to

form even when QPTC is deposited first. Second, the adsorption of coronene into the porous TPTC network is presented. When the TPTC network forms before the introduction of coronene we note little effect on the network morphology. However, when the molecules are mixed in the solution phase and deposited simultaneously we observe the non-uniform adsorption of coronene into the TPTC structure. At higher coronene concentrations we note the network forms with a different morphology shifted towards a more ordered state suggesting that when the molecules are deposited sequentially the system is kinetically trapped in the originally formed structure.

We then present a series of studies of molecular adsorption on the Au (111) surface. First, hexaazatrinaphthylene (HATNA) molecules are observed to form stable supramolecular structures when deposited from ethanol solutions. A core hydrogen bonding junction is identified. The network switches between two domain orientations and we identify a linear defect where the two domains meet. Second, we report the adsorption of Tri(4-bromophenyl)benzene (TBPB) on the Au (111) surface. TBPB forms three different structures at room temperature. When samples are heated during the deposition stage we observe the covalent coupling of pairs of molecules to form dimers. This reaction is confirmed by ToFSIMS experiments. The substrate is confirmed to play a significant role in the coupling process as subsequent experiments on HOPG failed to yield dimer formation. Finally we demonstrate the potential of a UHV-prepared sample by templating the adsorption of adamantanethiols.

Finally, we demonstrate the adsorption of a solubilised derivative of perylene tetracarboxylic dianhydride (PTCDA). PTCDA molecules have poor solubility in most solvents commonly used for liquid deposition. The addition of alkane chains attached to the sides of the perylene core promotes the solubility of the molecule in these solvents whilst leaving the anhydride functionality intact. Deposition is performed from 1-phenyloctance solutions on HOPG. The molecules form an ordered structure characterised by a single molecule unit cell. The results presented in this thesis show that the understanding of supramolecular networks has progressed to the point where changes in the morphology can be induced via a variety of processes.

## List of publications

- *Random Tiling and Topological Defects in a Two-Dimensional Molecular Network*, M. O. Blunt, **J. C. Russell**, M. D. Gimenez-Lopez, J. P. Garrahan, X. Lin, M. Schroder, N. R. Champness, P. H. Beton, *Science*, 322, 1077 (2008).
- *How Does Graphene Grow? Easy Access to Well-Ordered Graphene Films*, F. Muller, H. Sachdev, S. Hufner, A. J. Pollard, E. W. Perkins, **J. C. Russell**, P. H. Beton, S. Gsell, M. Fischer, M. Schreck and B. Stritzker, *Small*, 5, 20, 2291 (2009).
- *Solubilized Derivatives of Perylenetetracarboxylic Dianhydride (PTCDA) Adsorbed on Highly Oriented Pyrolytic Graphite*, **J. C. Russell**, M. O. Blunt, G. Goretzki, A. G. Phillips, N. R. Champness and P. H. Beton, *Langmuir*, 26, 6, 3972 (2010).
- *Templating molecular adsorption using a covalent organic framework*, M. O. Blunt, **J. C. Russell**, N. R. Champness and P. H. Beton, *Chemical Communications* 46, 38, 7157 (2010).
- *Guest-induced growth of a surface-based supramolecular bilayer*, M. O. Blunt, **J. C. Russell**, M. D. Gimenez-Lopez, N. Taleb, X. L. Lin, M. Schroder, N. R. Champness and P. H. Beton, *Nature Chemistry*, 3, 1, 71 (2011).
- *Dimerization of Tri(4-bromophenyl)benzene by Aryl–Aryl Coupling from Solution on a Gold Surface*, **J. C. Russell**, M. O. Blunt, J. M. Garfitt, D. J. Scurr, M. Alexander, N. R. Champness and P. H. Beton, *Journal of the American Chemical Society*, Article ASAP (2011).
- *Random Tilings of a Molecular Network Series*, A. Stannard, **J. C. Russell**, M. O. Blunt, J. P. Garrahan and P. H. Beton, (*manuscript in preparation*).

- *The Kinetic Trapping of an Absorbed Molecular System Induced by Sequential Deposition*, **J. C. Russell**, M. O. Blunt, M. D. Gimenez-Lopez, J. P. Garrahan, X. Lin, M. Schroder, N. R. Champness, P. H. Beton, (*manuscript in preparation*).
- *Tip-induced Manipulation of a Two-Dimensional Molecular Network*, **J. C. Russell**, M. O. Blunt, A. Stannard, J. P. Garrahan and P. H. Beton, (*manuscript in preparation*).

## Acknowledgements

I'd like to start by thanking my supervisor Peter for his wisdom and guidance throughout my Ph.D., reading the endless chapters of thesis and identifying all the incorrect uses of the words "where" and "were". To my adopted second supervisor Matt Blunt for putting up with my endless stream of annoying questions, doubts and STM-frustration. And to all my friends in the nanoscience group for their productive input to my work and counter-productive input to my thesis writing. Their comradery and friendship was a great comfort to me in the times when STM simply refuses to work.

I'd also like to pay a special acknowledgement to my parents. My education has been long and often bumpy journey. There was a time that I imagine even they doubted I would ever write a document more than four sides long. The fact that I have now completed a PhD thesis is a testament to their love, support and sometimes down-right stubbornness that they have ploughed into my education over the last twenty one and a half years. There is little doubt in my mind that I would never have achieved the academic heights I have without them. I'd also like to take this opportunity to thank them for always keeping my achievements separate from my wonderful, habitually over-achieving sister and congratulating me equally for my personal miles stones. I have never specifically thanked them for this, but it has meant a lot to me.

Finally I'd like to thank my partner Suzy. For always being there for me, whenever I've needed her.

*“The love of a man for a woman waxes and wanes like the moon, but the love of brother for brother is steadfast as the stars...”*

An Arabian proverb

# Contents

<b>Abstract</b>	<b>i</b>
<b>List of publications</b>	<b>iii</b>
<b>Acknowledgements</b>	<b>iv</b>
<b>1 Introduction and Scope</b>	<b>1</b>
1.1 Introduction . . . . .	1
1.2 Overview of this thesis . . . . .	4
<b>2 Supramolecular Network Formation</b>	<b>7</b>
2.1 Introduction . . . . .	7
2.2 Types of bonding interaction . . . . .	8
2.2.1 Hydrogen Bonding . . . . .	8
2.2.2 Van der Waals Interactions . . . . .	10
2.2.3 Covalent Bonds . . . . .	11
2.2.4 Pi-Pi Stacking . . . . .	12
2.3 Supramolecular architecture formation . . . . .	12
2.4 Previously reported examples of supramolecular networks . . . . .	17
2.5 Conclusions . . . . .	23
<b>3 Experimental Techniques</b>	<b>25</b>
3.1 Scanning Tunnelling Microscopy Theory . . . . .	25
3.1.1 Quantum Mechanic Tunnelling . . . . .	26
3.1.2 Tersoff-Hamann Theory . . . . .	29

3.1.3	Adsorbates on Surfaces . . . . .	32
3.1.4	Summary of Advantages and Limitations of STM . . . . .	33
3.2	From Theory to Images . . . . .	34
3.2.1	Piezoelectric Scan tubes . . . . .	36
3.2.2	STM Feedback Mechanism . . . . .	38
3.2.3	STM Tip Preparation . . . . .	40
3.3	Density Functional Theory . . . . .	41
3.4	ToFSIMS . . . . .	42
3.5	Substrate Materials . . . . .	43
3.5.1	Highly Ordered Pyrolytic Graphite . . . . .	43
3.5.2	Gold (111) . . . . .	46
3.6	Solution Deposition . . . . .	48
3.6.1	Specific solution deposition methods . . . . .	48
3.6.2	Solvents . . . . .	49
3.7	Image processing . . . . .	53
3.7.1	Distortion in STM images . . . . .	53
3.7.2	STM image flattening . . . . .	55
3.7.3	STM image enhancement . . . . .	55
3.8	Conclusion . . . . .	56
<b>4</b>	<b>The different adsorption morphologies of two carboxylic acid derivatives</b>	<b>58</b>
4.1	Introduction . . . . .	59
4.2	Experimental . . . . .	61
4.3	QPTC Results . . . . .	62
4.4	TPTC Results . . . . .	67
4.4.1	Analysis . . . . .	71
4.4.2	Network Defects . . . . .	78
4.4.3	Evolution of the TPTC network . . . . .	81
4.5	Manipulation of the TPTC network . . . . .	84
4.6	Conclusions . . . . .	91
<b>5</b>	<b>The formation of multi-component supramolecular structures</b>	<b>93</b>
5.1	Introduction . . . . .	94

5.2	QPTC bicomponent molecular systems . . . . .	95
5.2.1	Simultaneous deposition of QPTC and coronene . . . . .	96
5.2.2	QPTC-coronene drying experiments . . . . .	97
5.2.3	Simultaneous deposition of QPTC and perylene . . . . .	101
5.2.4	Guest molecule bonding geometries . . . . .	102
5.3	TPTC with coronene . . . . .	104
5.3.1	Sequential Coronene Deposition . . . . .	104
5.3.2	Simultaneous Guest Deposition . . . . .	109
5.4	Summary . . . . .	114
<b>6</b>	<b>Supramolecular networks formed on Au (111)</b>	<b>115</b>
6.1	Introduction . . . . .	116
6.2	The adsorption of Hexaazatrinaphthylene on Au (111) . . . . .	117
6.3	The adsorption and dimerisation of Tri(4-bromophenyl)benzene molecules on Au (111) . . . . .	121
6.3.1	Room Temperature Experiments . . . . .	122
6.3.2	Elevated Temperature Experiments . . . . .	125
6.4	Directing the adsorption of 1-adamantanethiols on Au (111) . . . . .	130
6.4.1	Adsorption of 1-adamantanethiols on Au (111) . . . . .	131
6.4.2	Directed adsorption of 1-adamantanethiol molecules into the TBPB covalently-bound template network . . . . .	133
6.5	Summary . . . . .	134
<b>7</b>	<b>Solubilised derivatives of perylene tetracarboxylic dianhydride adsorbed on graphite</b>	<b>136</b>
7.1	Introduction . . . . .	137
7.2	Experimental details . . . . .	138
7.3	The DPT-PTCDA network . . . . .	139
7.4	Discussion and Conclusions . . . . .	143
<b>8</b>	<b>Conclusions</b>	<b>146</b>

<b>Bibliography</b>	<b>149</b>
<b>List of figures</b>	<b>160</b>

# Chapter 1

## Introduction and Scope

*This chapter will present an introduction into nanoscience and nanotechnology including the original conception of the field and a discussion of its potential. An overview of the content of this thesis will then be presented.*

### 1.1 Introduction

Since the industrial revolution, man has slowly placed increasing priority on the space-efficiency of a wide range of consumer products. Such efficiency is logically desirable as products become easier to store and carry, increasing convenience as well packing more functionality into the same space. With the rise of mass production, this often translates into reduced material costs and increased productivity for companies. A classic example of this was the mobile phone industry at the turn of the millennium. Consumers had recognised the utility of owning a telephone that they could take anywhere with them and the market was rich with competing companies all trying to bring out

smaller and smaller handsets. It even became fashionable to have the smallest mobile phone on the market. Whilst it is true that such handsets offered increased convenience, they became so small that consumers had difficulty using them. The modern day market boasts handsets with vastly improved function including internet access, satellite navigation and personal music stereos, packing much more into the same space.

While this trend is applicable across the whole consumer electronics market, it has particular resonance with the computer industry. After the invention of the integrated circuit in 1958, the co-founder of Intel wrote to *Electronics Magazine* in 1965 observing that the number of transistors in an integrated circuit had doubled every year since invention[1]. He also stated he expected this trend to continue for at least the next 10 years. This later became known as Moore's Law. Whilst a few small changes to the exact wording of the law have been applied over the years, the law has in principle remained true for much longer than the originally anticipated duration. However, inevitably the production of smaller and smaller transistors is reaching a plateau where quantum mechanical effects are becoming important and the heat output of such devices is making them impractical for many applications. In order for significant further improvements in computational space-efficiency to be made, a fundamental change in the miniaturisation of electrical components has to occur.

In 1959, Richard P. Feynman presented a lecture to the American Physical Society entitled "Plenty of Room at the Bottom"[2] where he described the potential information storage capacity of small-scale physics. In his talk he discussed ideas such as storing the entire 24 volumes of *Encyclopedia Britannica*

in an area the size of a pin head, precise atomic manipulation and machine miniaturisation. The small or nano-scale world which Feynman described is today known as nanoscience. Whilst Feynman laid the conceptual ground work for the field of nanoscience and created interest within the academic community, it wasn't until after a book by K. Eric Drexler titled *Engines of Creation: The Coming Era of Nanotechnology*[3] was published in 1986 that the field started to receive interest in wider society. In his book Drexler explored the idea of nano-scale machines, building on Feynman's idea of miniaturised versions of the macroscopic machines used in industry. However, Drexler's ideas were controversial as many considered them physically unrealistic.

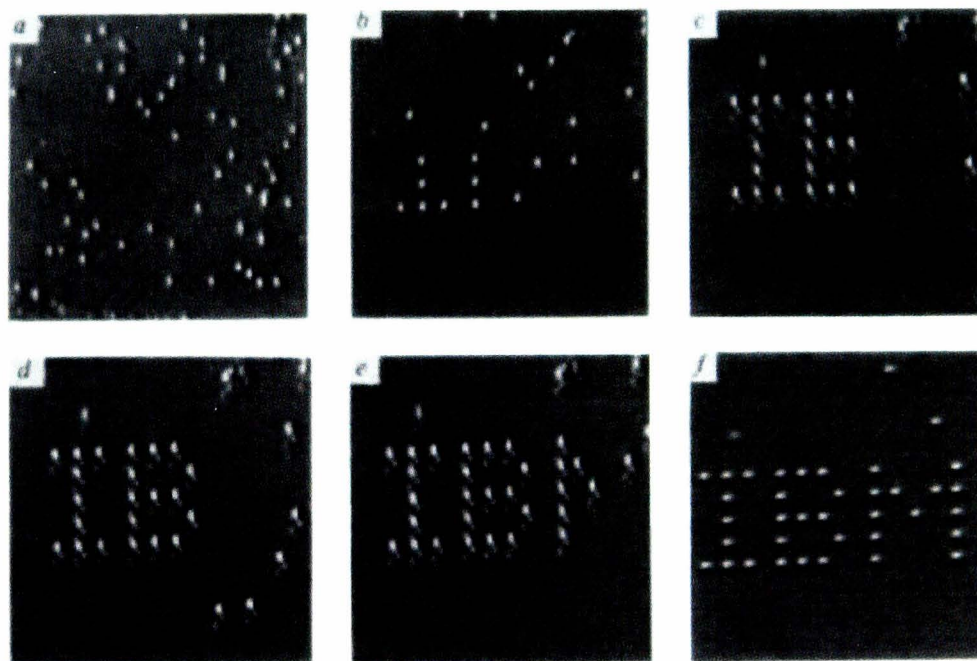


Figure 1.1: The letters IBM written with xenon atoms on a nickel (110) surface. Figure adapted from [4].

In 1990, after the invention of the scanning tunnelling microscope (STM) in 1982 by Gerd Binnig and Heinrich Rohrer, a proof of principle of single atom manipulation was demonstrated in a letter to the journal *Nature* by Don M. Eigler and Erhard Schweizer. They used an STM operating under ultra-high

vacuum (UHV) conditions at low temperature to position xenon atoms on a nickel surface to spell out the letters “IBM”, reproduced in Figure 1.1. They performed the manipulation using the tip of the STM to slide the xenon atoms one by one into the positions they desired thus demonstrating that single atom manipulation, as described by Feynman in 1959, was possible.

Whilst the manipulation presented by Eigler and Schweizer represents significant progress in realising the potential of nanoscience, extensive fabrication of nano-scale objects via this method would be extremely time consuming. A more elegant solution would be to design the system such that it is energetically favourable for the desired structure to form spontaneously out of the constituent parts. This type of fabrication is observed extensively in nature such as in the replication and recombination of deoxyribonucleic acid (DNA) cells. Feynman himself noted that if biological systems exhibit these fabrication techniques and that it should be possible for man to also use them. The spontaneous fabrication of nano-scale architectures on surfaces from solution is the primary focus of this thesis.

## **1.2 Overview of this thesis**

As described previously, this thesis is on the ‘bottom-up’ assembly of two dimensional nano-scale structures. Specifically the architectures formed by certain specially-synthesised molecules on graphite and gold surfaces for the applications of quantum dot formation, endohedral fullerene ordering and pharmaceutical applications. Chapter 2 provides an overview of the typical bonding interactions that arise between these molecules. This leads to a discussion

of how such interactions give rise to the formation of assemblies of molecules called supramolecular structures. The formation processes are related to previously reported work from the literature which forms the ground-work for this thesis. Chapter 3 discusses the experimental techniques utilised in this thesis focusing heavily on the theory and practical application of scanning tunnelling microscopy which is used extensively. In addition, details of the substrate materials used and a summary of experimental techniques are presented.

In Chapter 4 we present the adsorption of two carboxylic acid derivatives on the highly oriented pyrolytic graphite (HOPG) surface. These molecules are observed to form extended ordered supramolecular structures from nonanoic acid solutions. Quaterphenyl-tetracarboxylic acid (QPTC) forms a network where the molecules lie parallel to one another. Terphenyl-tetracarboxylic acid (TPTC) forms a network with no such translational symmetry which we determine to be stabilised by entropic contributions to the free energy. We also demonstrate the manipulation of this network by scanning it with STM with a specific range of voltage biases. Chapter 5 builds on the idea of network manipulation by looking at the changes induced in these carboxylic systems when additional guest molecular species are introduced. For QPTC, we observe the conversion to a hexagonally ordered network with the guest species adsorbed at the vertices. For the TPTC network we observe the preferential stabilisation of a specific sub-set of network vertices. However, in the case where the TPTC network is preformed, the network morphology is kinetically trapped.

Chapter 6 moves away from using HOPG as a substrate and looks at the adsorption of a number of molecules on the (111) crystallographic plane

of gold. Hexaazatrinaphthylene (HATNA) and tri(4-bromophenyl)benzene (TBPB) molecules are studied on the surface, with the latter being observed to undergo covalent bonding interactions when the substrate is heated to elevated temperatures during the deposition phase. These observations are backed up with time-of-flight scanning ion mass spectrometry experiments. Finally a UHV-prepared sample is used to direct the adsorption of adamantanethiol molecules deposited subsequently from solution. In Chapter 7 we investigate the adsorption of a solubilised perylene tetracarboxylic dianhydride (PTCDA) derivative on HOPG. The solubilising thiol ether side groups inhibit the formation of networks with the previously observed herringbone structure. The new structure is characterised by a single-molecule unit cell stabilised by double C–H···O bonds in addition to molecule-substrate contributions.

# Chapter 2

## Supramolecular Network Formation

*In this chapter a summary of the current understanding of the formation of supramolecular architectures on surfaces is presented. The networks are stabilised by contributions from a number of molecular bonding interactions the strength of which varies depending on the molecules involved. Key processes such as adsorption, desorption and diffusion are also discussed with consideration to the implications for the nucleation and subsequent growth of supramolecular structures. Finally the current state-of-the-art is presented and discussed in light of the bonding interactions and growth processes outlined previously.*

### 2.1 Introduction

Bottom-up nanoscale fabrication techniques have been viewed as a potential route to influencing matter in a predetermined and definable way on the

nanometer scale. Such methods are based on carefully controlling the parameter space so that in evolving to the free energy ground state, the system adopts a pre-targetted structure. In the case where molecules spontaneously form ordered assemblies with the internal structure governed solely by the intramolecular interactions, this is referred to as molecular self-assembly.

The focus of this chapter will be on the mechanisms by which these systems evolve into the energetic ground state. Specifically, the adsorption and subsequent diffusion of molecules on the surface will be discussed in light of the broad range of molecule-molecule and molecule-substrate interaction that can influence such processes. Crucially to bottom-up fabrication techniques, the growth of supramolecular structures will be considered with respect to thermodynamic and kinetic effects.

## **2.2 Types of bonding interaction**

Underpinning the whole of bottom-up nanoscale fabrication (and other far-reaching areas of physics) are a whole range of atomic and molecular attractive interactions that give rise to a binding energy between molecules and the surface. In this section, the interactions which are of particular relevance to the experiments carried out in this thesis will be discussed.

### **2.2.1 Hydrogen Bonding**

When a hydrogen atom is covalently bound to an electronegative atom such as fluorine or oxygen, the electron cloud becomes decentralised being drawn towards the electronegative atom [5]. This leaves the hydrogen atom with a

partial positive charge. A second electronegative atom, either connected to the same molecule or another entirely, will feel a highly-directional attractive electrostatic interaction known as a hydrogen bond. The hydrogen atom which is covalently bound to the electronegative atom is known as the hydrogen bond donor. The second electronegative atom is the hydrogen bond acceptor.

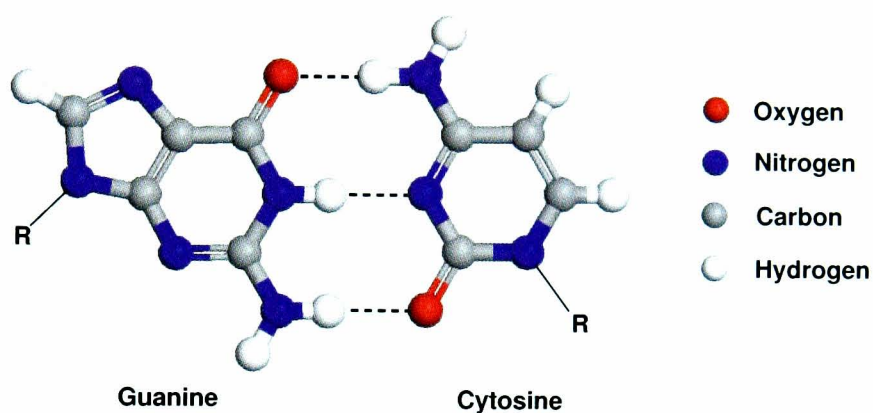


Figure 2.1: A molecular ball and stick diagram showing the triple hydrogen bonding junction between the DNA bases Guanine and Cytosine. The hydrogen bonds are illustrated by the dashed black lines.

Hydrogen bonding is particularly important in nature as it forms the main interaction between the bases in deoxyribonucleic acid (DNA) [6]. For example, consider the bonding interaction between the bases guanine and cytosine shown in Figure 2.1. The DNA base pair form a total of three hydrogen bonds, two N–H···O bonds and one N–H···N. The total strength of the hydrogen bonding interaction will be given by the sum of the strengths of each bond. For DNA it is critical that the molecules are able to separate easily under certain conditions thus making strong intermolecular bonds, such as covalent bonds, unsuitable.

Another common example of hydrogen bonding occurring in nature is between the molecules in water. Each H<sub>2</sub>O molecule can form up to four hydrogen bonds with neighbouring molecules, two as hydrogen bond acceptors through

the two lone pair electrons, two as hydrogen bond donors through the hydrogen atoms. The strength of each hydrogen bond is 0.22 eV per molecule giving rise to a potential overall stabilisation energy of 0.87 eV. This energy is very significant and means water has a much higher boiling and melting temperature compared to similar molecules that do not form hydrogen bonds. In some respects the hydrogen bonding between water molecules is maximised as each molecule can form two hydrogen donor and two acceptor bonds.

### **2.2.2 Van der Waals Interactions**

Van der Waals forces describe the electrostatic interactions between atomic and molecular dipoles. For instance, atoms and molecules with permanent electric dipoles will interact with each other through electrostatic forces. If their orientations are not constrained, the forces will cause them to align themselves with one another maximising the electrostatic attraction. These types of interaction are not limited to atoms and molecules with permanent dipole moments. Non-polar species can have induced dipoles either by the presence of another atom or molecule with a permanent dipole, or instantaneously by another non-polar species. An atom or molecule with a permanent dipole will influence the uniform electron cloud of a non-polar species by repelling it from the negatively charged pole (and attracting it to the positive pole) effectively inducing a dipole. Atoms and molecules with no permanent dipole can induce polarisation in each other as instantaneously all electrons have to be at some position. It is therefore highly unlikely that the net total charge of the species will be uniformly distributed, resulting in an instantaneous dipole. This dipole will electrostatically interact with any neighbours and *visa versa*. The interac-

tions between instantaneous dipoles are often referred to as London dispersion forces.

Individual atomic pairwise van der Waals interactions are very weak, typically of order 10 meV for species with a permanent dipole and less for London dispersion forces. The strength of the interaction will also scale with the size of the atom. However, since any atom can acquire an instantaneous dipole and thus interact with another via London dispersion forces, the total accumulative effect can be very strong, particularly for large molecules.

### 2.2.3 Covalent Bonds

Covalent bonding occurs from the sharing of electrons between atoms in order to fill orbitals in the resulting molecule. For instance, two hydrogen atoms can form a covalent bond, sharing the two electrons and thus filling the first molecular orbital of the molecule  $H_2$ . Covalent bonds form some of the strongest interactions between atoms with typical bonding energies between 2 eV and 8 eV.

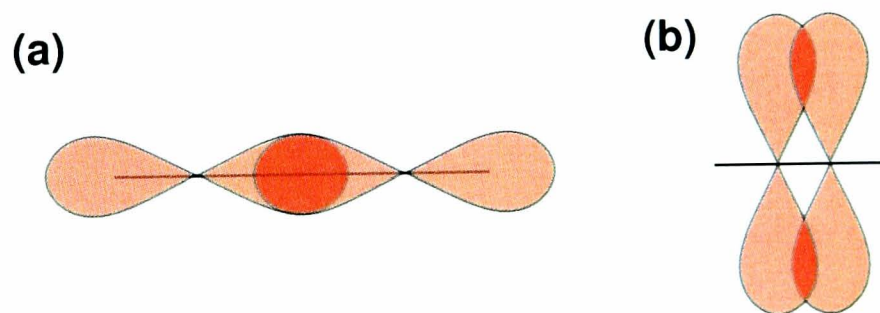


Figure 2.2: Schematic illustrations of 2p orbitals forming (a) sigma and (b) pi bonds.

There are a number of different types of covalent bond, in particular sigma bonds and pi bonds. Sigma bonds are generally the strongest covalent bond

and are defined as bonds where the maximal overlap of the probability density of electronic orbitals lies along the axis between the atomic nuclei or bond axis, as shown in Figure 2.2a. Pi bonds are covalent bonds in which the plane of the overlapping orbitals is away from the bond axis (see Figure 2.2b). These types of bond often occur in atoms connected by double covalent bonds, such as the carbon atoms in ethylene. In this case the carbon atoms form one sigma bond and one pi bond. Pi bonds are generally weaker than sigma bonds owing to the reduced overlap of the electron orbitals.

#### **2.2.4 Pi-Pi Stacking**

In aromatic systems, a large number of p-orbital electrons will be involved in pi covalent interactions. These bonds can form intermolecular interactions when stacked perpendicularly to the plane of the molecule. The strength of the interaction is proportional to the amount of overlap between the pi systems. Like van der Waals interactions, pi-pi stacking is an accumulative interaction thus is much stronger for larger aromatic systems.

### **2.3 Supramolecular architecture formation**

In this section we present an overview of general growth mechanisms at surface interfaces. The mechanisms are not limited to molecular systems or only two dimensional growth. However, given the focus of this thesis, we discuss them in terms of molecular self-assembly. In addition it is important to identify from the outset that the precise microscopic growth mechanics of molecular self-assembly from solution deposition are not well understood. In particular

the role of the solvent molecules is unknown and likely to be very significant. Whilst the mechanics that are subsequently outlined in this chapter are better understood for supramolecular structures formed under ultra-high vacuum (UHV) conditions, it is likely that some or all of them play a role in growth from solution. This is particularly identifiable from the many parallels can be drawn between networks formed by these different deposition techniques. Thus give the relevance of such mechanics for the work presented in Chapters 4 and 5, our current understanding is presented here.

The first phase of the controlled formation of supramolecular architectures is the adsorption of the molecular species in question on the surface. In general this is achieved by one of two methods; sublimation or solution deposition. Sublimation is carried out by heating the powdered form of the molecule (normally in a Knudsen cell) under UHV conditions. The molecules are vapourised and subsequently condense on the sample surface. In the case of solution deposition, the target molecules are dissolved in a solvent and a small quantity is drop-cast directly onto the sample (for more details on solution deposition see Chapter 3). When molecules in solution adsorb on the surface, depending on the molecule-solvent bonding geometry, the molecule may have to break some of the bonds formed with solvent molecules. This will give rise to an energy barrier to adsorption. The arrival rate of molecules to the surface is given by  $R = \frac{P}{(2\pi mk_B T)^{1/2}}$  [7] where  $P$  is the equivalent vapour pressure of molecules on the surface,  $m$  is the mass of the molecule,  $k_B$  the Boltzmann constant and  $T$  the temperature. The pressure is in a broad sense controllable by the duration of heating and temperature of the Knudsen cell for sublimation, and the molecular concentration for solution deposition. Hence, control can be exerted

to some extent over the arrival rate of molecules to the surface.

In general, adsorption of molecular species can be divided into two categories; chemisorption and physisorption. Chemisorption describes adsorption where the chemistry of the system changes, for example if a molecule covalently bonds to the surface. The chemical properties and characteristics of the adsorbed molecule change. Generally chemisorption refers to systems with strong admolecule-substrate interactions. The physisorption of molecules refers to weaker admolecule-substrate interactions where the chemistry of the adsorbed species remains intact. Conventionally, molecules which interact through van der Waals interactions or pi-pi stacking are termed physisorbed.

Once a molecule is adsorbed on the surface it is not permanently bound in one place- it may desorb or diffuse across the surface. The probability of desorption will depend on the strength of the admolecule-substrate interaction. Generally desorption is energetically unfavourable because of the admolecule-substrate interactions. However, there is still a small but finite probability of such events occurring. Specifically, for desorption back into solution this process may be mediated by forming admolecule-solvent interactions on the surface prior to full desorption back into solution reducing the net energy barrier for the process. It is important to note that for solution deposition in particular, molecules may form aggregates in the solvent and adsorb on the surface in large groups. As discussed later, the structure formed under these conditions may play a crucial role in the formation of a supramolecular structure.

As mentioned, an adsorbed molecule may diffuse across the surface. This process requires the breaking of admolecule-substrate bonds. This breaking

of bonds creates an energy barrier to the process proportional to the bond strength, known as the diffusion barrier. The admolecule can be thought of as moving from one potential energy minimum to another. Taking this idea further, the interactions with an adsorbed molecule can be described as a potential energy isosurface defined by the net binding energy of the molecule to the surface as a function of position. Molecules will be predominately adsorbed in potential energy minima and diffusion events will describe translations of the molecule from one minimum to another. The frequency of diffusion events is given by

$$\nu_d = (a^2 D/4)e^{-E_d/k_B T} \quad (2.1)$$

where  $a$  is the jump distance,  $D$  is the diffusion coefficient, and  $E_d$  is the energy required for diffusion.

The initial nucleation of supramolecular structures requires that at least two admolecules encounter one another. These molecules will interact with one another through the formation of admolecule-admolecule bonds such as those discussed in Section 2.2. This will result an additional stabilisation energy for these molecules. Note that the formation of admolecule-admolecule interactions effectively modifies the potential energy isosurface creating lower energy adsorption sites where these interactions can form. These lower potential energy minima increase the stability of the adsorbed species and reduce the probability of desorption. This increased stability leads to the growth of a supramolecular structure. The nucleation rate of these structures will be dependent on the density of molecules on the surface and their surface mobility.

Returning to the specific case of supramolecular network formation from

solution, the relative importance of the diffusion process is not well understood. It is possible that with solution deposition the arrival rate of molecules to the surface is high and network nucleation and growth occurs from the chance adsorption of two molecules next to one another. Solution deposition is also likely to be a more dynamic process as molecules can readily desorb back into solution and re-adsorb again. The frequency of this will be dependent on a number of factors, including the solubility and the net strength of ad-molecule interactions. This dynamic nature provides a mechanism for molecules to order themselves on the surface. Molecules that are adsorbed into a supramolecular structure can also desorb from the surface. However, there will be a significant contribution to the binding energy from ad-molecule-ad-molecule interactions in this case. This will act to reduce the probability of desorption. If the molecule is more strongly bound to the supramolecular architecture, the probability will be even lower. Hence molecules that are adsorbed in positions that correspond to the global energy minimum of the system will be the least likely to desorb from the surface and therefore the most stable.

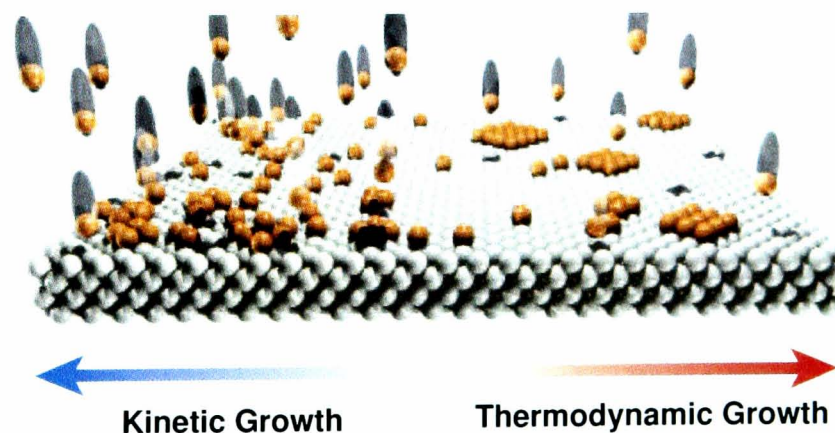


Figure 2.3: An illustration showing the effect different growth process can have on the structure of islands of adsorbed species. Figure adapted from reference [8].

In general, growth mechanics, adsorption and diffusion rates go further

than just influencing the nucleation of structures; they also determine the way in which these structures grow. For instance, if the adsorption rate on the surface is much less than the diffusion rate, adsorbates will on average diffuse across more of the surface before encountering another molecule. This leads to an increase in the rms displacement of adsorbed species given by  $x_{rms} = (D\tau)^{1/2}$ , where  $\tau$  is the mean residence time of the species on the surface. As such, on average adsorbates will sample more of the potential energy isosurface therefore be more likely to be in a global low-energy configuration. This is equivalent to the supramolecular structure growing closer to equilibrium conditions (known as thermodynamic growth) and as such generally gives rise to networks with long-range structural order as shown in Figure 2.3. Conversely, if the rate of adsorption is higher than the diffusion rate then kinetic growth effects dominate resulting in molecules quickly becoming trapped in metastable configurations, again shown in Figure 2.3. This type of kinetic growth leads to supramolecular networks where individual bonding processes have increased significance.

## 2.4 Previously reported examples of supramolecular networks

The assembly of a wide variety of supramolecular architectures has been reported in the literature and significant progress has been made towards controlling the formation of these structures at the molecular level. In this section a number of key papers that precede the work presented in this thesis will be discussed in addition to how these relate to various aspects of the supramolec-

ular assembly process.

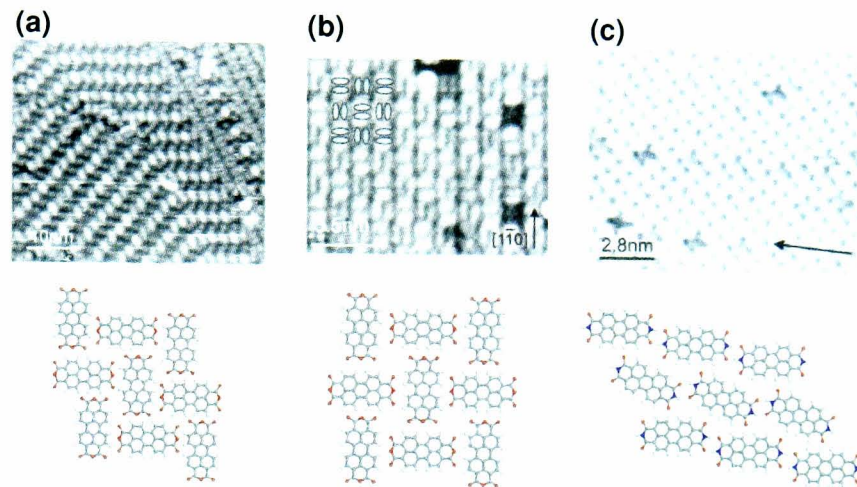


Figure 2.4: Images of the PTCDA **(a)** herringbone and **(b)** square phases, with **(c)** the PTCDI row phase, all taken from [9]. Molecular schematics are presented beneath each image highlighting the molecular packing.

A great deal of interest has surrounded the organic semiconductors 3,4,9,10-perylenetetracarboxylic-dianhydride (PTCDA) and the imide derivative PTCDI because of their opto-electronic properties and therefore potential applications in photovoltaic devices and transistors. Whilst many other organic semiconductors share similar potential applications, these molecules have been shown to form ordered structures when deposited on a number of surfaces[10] including Au (111)[11], Ag-Si (111)- $\sqrt{3} \times \sqrt{3}$ [12, 9], HOPG[13, 14] and Cu (111)[15]. Two distinct bonding geometries of PTCDA have been identified (shown in the scanning tunnelling microscopy (STM) images in Figure 2.4a and b). These networks are stabilised by admolecule-substrate interactions, predominately in this case van der Waals type interactions, and by  $O \cdots H-C$  hydrogen bonds between the anhydride groups and the perylene core of the PTCDA molecule. Both structures are observed to form ordered large domains on the surface. By contrast, PTCDI is reported to only form one

phase shown in Figure 2.4c. These molecules form double  $O \cdots H-N$  hydrogen bonds (as well as admolecule-substrate interactions). The addition of the imide group inhibits the hydrogen bonding between the oxygen atoms and the perylene core and energetically biases the system to bond through the end groups instead. This is an example of how changing a relatively small percentage of the molecular structure can completely change how molecules interact with one another on a surface. It also illustrates that with careful selection of molecular functional groups, different supramolecular structures can be formed on a surface.

Otero et al. have presented the formation of random cytosine networks adsorbed on Au (111)[16]. A variety of different hydrogen bonding junctions are observed to form suggesting that unlike PTCDI networks, a number of different bonding geometries have similar energetic stability - an observation backed up by theoretical studies[17]. The system will need comparatively longer to explore the potential energy isosurface as there are many metastable configurations with energies comparable to the true energetic minimum state. Thus, as the system is quickly thermally quenched to lower temperatures molecules become trapped in these metastable states often give rise to a network with no long-range order as defined by kinetic growth mechanisms. Further to this, Treier et al.[18] have presented the covalent coupling of PTCDA molecules with two amine derivatives. They report extended polymer networks on the heating of the substrate formed by imidisation reactions. The networks they form also do not have long-range order. The covalent bonds formed by the polymerised network are sufficiently strong that once formed the energy barrier to breaking them makes such an event unlikely leading to the domination

of kinetic growth effects.

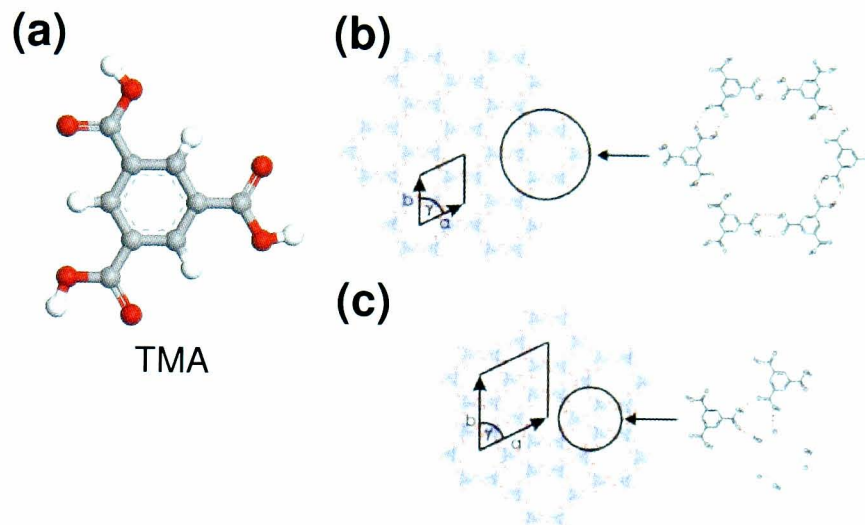


Figure 2.5: **(a)** A molecular schematic of the TMA atomic structure. Diagrams of **(b)** the TMA chickenwire and **(c)** flower structures taken from reference [19]

The systems discussed thus far have all been based around vacuum deposition techniques. In the literature there are numerous examples where techniques such as solution deposition are utilised. Particular attention has been on the supramolecular networks formed by trimesic acid (TMA), shown in Figure 2.5a [19, 20, 21, 22, 23]. These molecules have been shown to form two open porous structures on the highly oriented pyrolytic graphite (HOPG) surface. The networks form extensively across the surface with the long-range order apparent from images with submolecular-resolution. Double  $\text{O-H}\cdots\text{O}$  hydrogen bonds are formed between the carboxylic acid groups in neighbouring TMA molecules stabilising the chickenwire structure, shown in Figure 2.5b. The flower structure (Figure 2.5c) is stabilised by a mixture of double carboxylic acid hydrogen bonds and single  $\text{O-H}\cdots\text{O}$  bonds. Interestingly, both structures are porous, in that within the non-defective structure, areas of the HOPG substrate beneath are exposed. From this we can deduce that the en-

ergy saving from satisfying the hydrogen bonds is greater than the energetic cost of not having molecules adsorbed in these areas. However, this is not the complete picture as it is possible that molecules may weakly bind into these regions and not be stable under STM scanning. This will contribute to the total stabilisation energy of the system. Solvent molecules in particular may adsorb in these regions. The paper by Lackinger et al. [19] explores the influence of the solvent used in the deposition process further by observing changes in the abundance of the two TMA structures when the solvent is changed. They observe the formation of a “flower” phase for solvents with a shorter alkane chain and a “chickenwire” phase for larger chain solvents citing the cause as either the stabilisation of molecular clusters in the solution phase or the preferential stabilisation of one structure on the surface. If small crystals of solute are forming in the solution phase in a particular orientation, say that of the trimer group shown in Figure 2.5c for the short chain solvents, this may bias the structure that forms when the solution is brought into contact with a surface. Alternatively, the adsorption of solvent molecules into the porous regions could stabilise the network differently depending on the solvent in question. As such, the shorter solvent molecule may energetically bias the network to form the flower structure.

Supramolecular networks that are stabilised by weak van der Waals interactions are also reported extensively in the literature. In particular the work by De Feyter et al. on the adsorption of a variety of molecules with long alkane chains demonstrates that weak interactions acting in parallel can stabilise large structures [26, 27]. Whilst the van der Waals interaction between carbon atoms in two alkane chains is itself weak, the total binding energy is determined

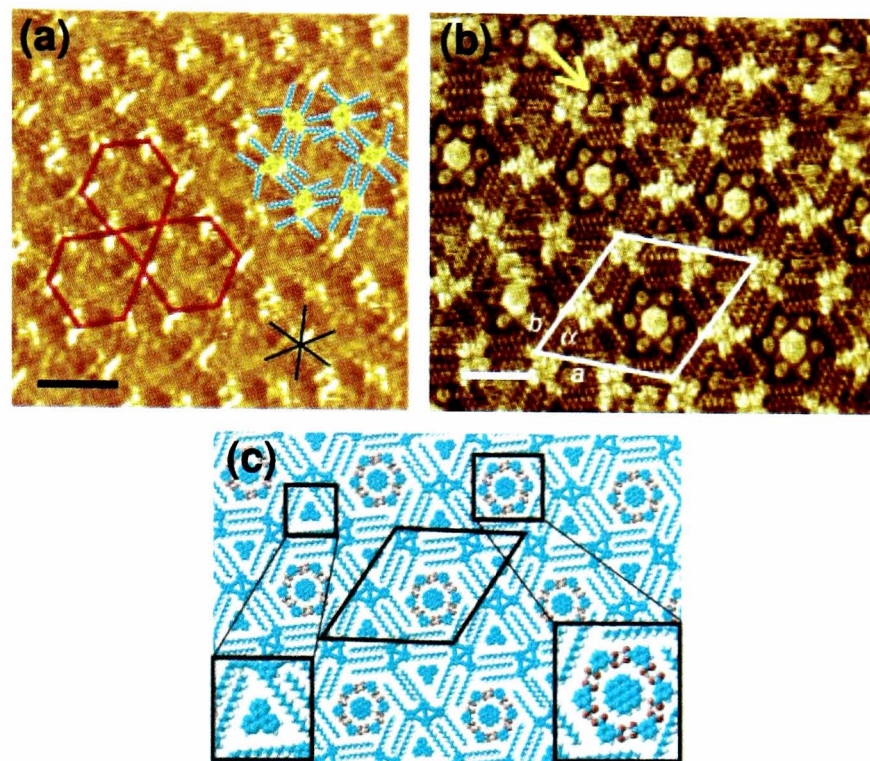


Figure 2.6: **(a)** An STM image illustrating the Kagomé network formed by a DBA derivative. The scale bar is 4 nm. Figure is adapted from reference [24]. **(b)** The porous nature of the network is utilised to direct the adsorption of coronene, isophthalic acid and triphenylene guest molecules. The scale bar is 3nm. **(c)** A schematic model of the supramolecular network shown in (b). Figures (b) and (c) are adapted from reference [25].

from the sum of all these interactions along the full length of the chain. This also applies to admolecule-substrate contributions where, for surfaces such as HOPG, the adsorption energy increases linearly with chain length, due to the close registry between the graphite lattice constant and the separation of carbon atoms in the alkane chain [27]. For the majority of the systems reported [26, 28, 29, 27], lamellar-type structures are formed where alkane chains lie side by side maximising the van der Waals interactions between molecules. However for two dehydrobenzo[12]annulene (DBA) derivatives, porous Kagomé structures are observed [24, 30, 31], shown in Figure 2.6. They identify that the hexagonal pores of such a Kagomé network are of ideal size for the adsorption

of one coronene molecule surrounded by six isophthalic acid molecules. They demonstrate this by nucleating the formation of the kagomé structure by the sequential deposition of these molecules with a DBA derivative which, when deposited alone, forms a non-porous structure[25]. They also show that the resulting kagomé structure additionally hosts the adsorption of triphenylene guest molecules in the vacant triangular pores (Figure 2.6). Another example of the use of a supramolecular architecture to direct the adsorption of a guest molecule is the work by Theobald et al. who demonstrate the formation of a hexagonal porous network formed by PTCDI and melamine molecules[32]. The melamine molecules adsorb at the vertices of the network and each is bonded by a triple hydrogen bond to three PTCDI molecules. They show that this network may be used to direct the adsorption of  $C_{60}$  guest molecules, observing up to seven trapped per hexagonal pore. This work was later reproduced using solution deposition techniques by Madueno et al.[33].

## **2.5 Conclusions**

In this chapter a summary of different bonding interactions is presented. The circumstances in which these bonds arise is discussed as well as the relative interaction strengths. However, how these interactions give rise to the growth of supramolecular architectures from solution is not well understood. Thus we present the current understanding of general growth mechanisms in the context of molecular organisation under UHV conditions. It is likely that many of these mechanisms play a role in the solution case though a precise microscopic understanding of the process is not known. Finally an overview of

supramolecular network studies in the literature is presented, with particular attention to liquid STM studies.

# Chapter 3

## Experimental Techniques

*In this chapter, an overview of all experimental techniques and imaging practices is presented. Specifically scanning tunnelling microscopy is used extensively in sample imaging and a brief overview of basic theory and experimental practices is described. A detailed description of the structure and properties of all the materials used in experiments is presented. The image analysis and drift correction techniques utilised are also reviewed.*

### 3.1 Scanning Tunnelling Microscopy Theory

The scanning tunnelling microscope, or STM, was invented by Gerd Binnig and Heinrich Rohrer at the IBM facility in Zürich in 1982 [34]. The technique involves bringing an atomically sharp probe into close proximity to a sample surface. When a voltage bias is applied across the tip-sample junction electrons can pass across the gap due to quantum mechanical tunnelling (Section 3.1.1) giving rise to a small but measurable current (tunnel current). This

current is exponentially dependent on the tip-sample separation resulting in sub-Ångstrom height resolution. Piezo-electric transducers provide control of lateral probe movement enabling the tip to be scanned over the sample and the tunnel current measured. As the current changes, implying a change in tip-sample separation, the position of the tip is adjusted using a feedback control loop. This loop controls the vertical tip motion so that the current returns to a target value, thus maintaining a constant tip-sample separation. An image of the surface can then be reconstructed from how the tunnel current changes across the surface as discussed in Section 3.2.2.

### 3.1.1 Quantum Mechanic Tunnelling

The main physical principle which underpins STM operation is that of quantum mechanical tunnelling. This phenomenon arises from the decay of the wavefunction into a finite height potential barrier as determined from the general solutions of the 1D time-independent Schrödinger equation (TISE), shown in equation 3.1

$$-\frac{\hbar^2}{2m} \frac{d^2\psi}{dx^2} + V(x)\psi = E\psi \quad (3.1)$$

where  $\psi$  is the time-invariant wavefunction of the electron,  $V$  the potential energy at position  $x$  and  $E$  corresponds to the energy eigenvalues.

Consider the 1D case where an electron is incident on a potential energy barrier of finite height and width, similar to that shown in Figure 3.1. The general solution for the electron inside this barrier is of the form

$$\psi = Ae^{\pm\kappa x} \quad (3.2)$$

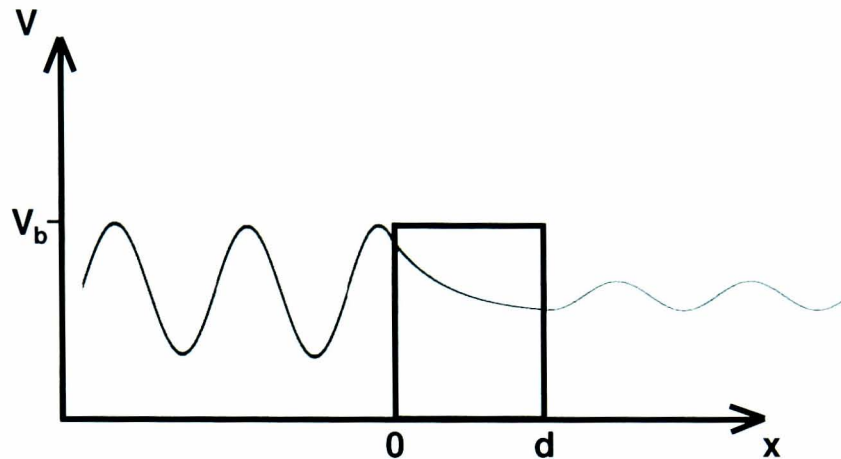


Figure 3.1: A schematic diagram of a one dimensional finite quantum barrier of width  $d$  and height  $V_b$ . Classically, the electron does not have the energy to surmount the barrier.

where  $A$  is a constant,

$$\kappa^2 = \frac{2m(V_b - E)}{\hbar^2} \quad (3.3)$$

and  $V_b$  is the height of the potential energy barrier. Determining the probability amplitude at position  $d$ , where  $d$  is the width of the potential energy barrier, gives rise to the transmission probability

$$T = |\psi|^2 \sim e^{-2\kappa d}. \quad (3.4)$$

This non-zero result shows that with a quantum mechanical approach, electrons have a finite probability of “tunnelling” through a potential energy barrier.

Consider the energy levels in two different materials that are initially separated, as shown in Figure 3.2a. If these two materials are brought into immediate proximity of one another and allowed to relax into electrical equilibrium, the fermi levels align resulting in a contact potential as shown in Figure 3.2b. If a voltage,  $V$ , is then applied across the junction, the fermi levels are shifted

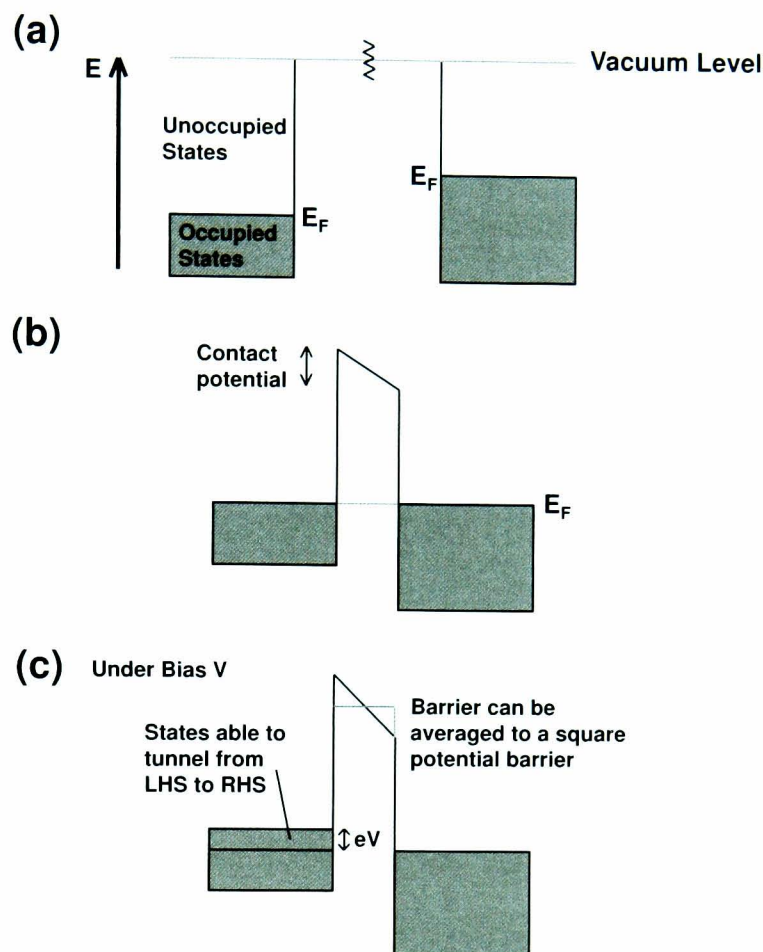


Figure 3.2: Schematic diagrams of the energy levels of two materials brought into electrical contact with one another. **(a)** Initially the two materials are not in electrical contact and have different Fermi levels. **(b)** When the materials are brought into contact the Fermi levels align resulting in a contact potential between the two materials. **(c)** If a voltage bias is applied across the junction the fermi levels shift and electrons with energy within  $eV$  of the Fermi level have a finite probability of tunnelling into the empty valence band states in the other material.

with respect to each other enabling electrons with energy within  $eV$  of the fermi energy to tunnel through the barrier into the empty states in the other material. If we assume that the barrier between the materials can be averaged to a square potential barrier, tunnelling will occur with the transmission probability described in equation 3.4. The tunnelling of electrons between the

materials will give rise to a small current described by the equation

$$I \sim e^{-2\kappa d} n(E_F) eV \quad (3.5)$$

where  $n(E_F)$  is the local density of states (LDOS) at the Fermi level. Equation 3.5 also highlights the exponential distance dependence of the tunnel current on the barrier width.

### 3.1.2 Tersoff-Hamann Theory

In order to further the theoretical investigation into the interaction between STM tip and sample, Tersoff and Hamann[35, 36] proposed that when the tip and sample are in close proximity, the electronic states could be considered independently but overlap. This requires the assumption that the states in the tip and sample are weakly coupled. Thus the wave function decays rapidly into the barrier. Making this assumption, the matrix element describing the electron transfer as a result of the overlap can be determined from time-dependent perturbation theory. Adopting this approach, they show that the tunnelling current,  $I$ , is given by

$$I = \frac{2\pi e}{\hbar} \sum_{\mu, \nu} \{f(E_\mu)[1 - f(E_\nu)] - f(E_\nu)[1 - f(E_\mu)]\} |M_{\mu\nu}|^2 \delta(E_\nu - E_\mu + eV) \quad (3.6)$$

where  $f(E)$  is the Fermi function of that state and  $M_{\mu\nu}$  is the tunnelling matrix describing the transfer between states. This equation can be simplified by taking the zero temperature limit where the Fermi functions become unit step

functions. Bardeen[37] showed that the tunnelling matrix may be written as

$$M_{\mu\nu} = -\frac{\hbar^2}{2m} \int (\psi_\mu^* \nabla \psi_\nu - \psi_\nu \nabla \psi_\mu^*) \cdot d\mathbf{S} \quad (3.7)$$

where the integral is over any surface that lies entirely within the barrier region.

To explicitly determine the matrix element, it is necessary to accurately describe the wave functions of the system. However this relies on the exact atomic structure of the tip, which is unknown. Thus it is necessary to produce a model of the tip. Tersoff and Hamann[35] present a simple model where the ideal STM tip is used. The apex is described by a sphere centred at  $r = r_0$  with a radius of curvature  $R$  and separated from the surface by a distance of closest approach  $d$ . The wavefunctions of this tip are modelled as

$$\psi_\mu = \Omega_t^{-1/2} c_t \kappa R e^{\kappa R} e^{-\kappa|r-r_0|} (\kappa|r-r_0|)^{-1} \quad (3.8)$$

where  $\Omega_t$  is the volume of the probe,  $c_t$  is a normalisation term and  $\kappa$  is as defined in Section 3.1.1. This equation is valid for the simplified case where the work function of the two materials is equal and  $R \gg \kappa^{-1}$ . Using this model, the matrix element becomes

$$M_{\mu\nu} = \frac{4\pi\hbar^2}{2m\kappa} \Omega_t^{-1/2} \kappa R e^{\kappa R} \psi_\nu(r_0) \quad (3.9)$$

assuming that the tip wave function is in the s-wave state ( $l = 0$ ). This result for the matrix element may then be used to determine the tunnel current

$$I \propto \sum_\nu |\psi_\nu(r_0)|^2 \delta(E_\nu - E_F) \equiv n(r_0, E_F). \quad (3.10)$$

where  $n(r_0, E_F)$  is the local density of states at the apex of the tip at the Fermi level. Thus the STM tunnel current provides a measure of the charge density at the Fermi level at the position of the tip. It therefore follows that if the tip is scanned across the sample surface so that the measured current is held constant, the path of the tip follows a contour of constant local density of states as discussed in Section 3.2.2.

### **Limitations of Tersoff-Hamann Theory**

Tersoff and Hamann's work illustrated the relationship between the quantum mechanical tunnel current and the local density of states of the surface. Crucially, it is assumed that the states in the tip and surface are weakly coupled as first order perturbation theory is used in the determination of the tunnel current. The closer the STM tip is to the surface, the stronger the states will interact and chemical forces begin influencing the tip, resulting in a breakdown of the formulae. If the tip gets closer still it will eventually snap into contact with the surface. Tersoff-Hamann also assumes that the voltage applied across the tunnelling junction is very low. For metals this is normally the case, however for semiconducting samples, the band gap requires higher voltages to even draw a tunnel current. Also larger voltages are conventionally used in tunnelling spectroscopy experiments.

Fortunately, the expression in equation 3.10 can be generalised to finite non-zero voltages by considering the sum of the contributions to the LDOS

$$I \propto \int_{E_F}^{E_F+eV} n(E, r_0) T(E, eV) dE. \quad (3.11)$$

where  $T$  again is the transmission probability. This breaks down for large voltages[38] but for the purposes of the systems studied in this thesis it is an acceptable approximation.

### **3.1.3 Adsorbates on Surfaces**

The exponential dependence of the tunnel current on distance from the surface implies that electrons from the top layer of the sample crystal make by far the most significant contribution to tunnelling. The electronic properties of atoms and molecules adsorbed on the surface of the sample will therefore have a significant effect on the LDOS. Chapter 2 discussed the different types of bonding motifs that can arise between atoms and molecules. It is these types of bonding events that give rise to the adsorption of atoms and molecules on surfaces. The impact of such adsorption on STM has been studied in the literature[39, 38, 40, 41]. Particular attention should be drawn to the work by Wintterlin et al.[41] on oxygen adsorbed on Al (111) which provided evidence that the oxygen made a negative contribution to the LDOS of the system, thus actually appearing in STM as indented areas of surface. Clearly this demonstrates that care must be taken when STM images are analysed for topographical information. But it also highlights that the LDOS in the presence of an adsorbate becomes a superposition of the substrate and adsorbed species states.

Equation 3.11 describes the behaviour of the tunnel current at non-zero, low voltages. This equation is still valid for tunnelling through adsorbates. As this thesis is focused on the adsorption of different molecular species, the effect on the LDOS will only be discussed from the point of view of molecular ad-

sorbates. Theoretical estimates of quantum tunnelling through the adsorbed species requires understanding of the molecular wavefunction. Qualitatively this can be described by the linear combination of atomic orbitals (LCAO) approximation[42]. In this approximation, the molecular orbital is determined from the linear expansion of the constituent atomic orbitals that make up the molecule. Using the relationship in equation 3.10 we can relate the resulting tunnel current to these molecular orbitals. In the limit of finite voltage (equation 3.11) the states that contributed to the tunnel current are those with energy between  $E_F$  and  $E_F + eV$ . For conventional STM voltages this limits tunnelling to only a few molecular orbitals. For positive tip biases (or negative sample biases), electrons will tunnel out of states in the sample into the tip. The STM will therefore be probing the highest occupied molecular orbital (HOMO) of the sample. There may also be contributions from the HOMO-1 and HOMO-2 energy levels, referring to the two energy levels directly below the HOMO. For negative tip biases (or positive sample biases), electrons will tunnel from the tip into the sample, hence probing the lowest unoccupied molecular orbital (LUMO) of the sample. There may also be contributions from the LUMO+1 and LUMO+2.

### **3.1.4 Summary of Advantages and Limitations of STM**

The invention of the STM opened up a completely new technique for the imaging of surfaces. Unlike any previous surface characterisation methods, the technique is based on bringing a local probe into the immediate vicinity of the surface giving it some key advantages. Previously unresolvable non-periodic features, such as step edges and topological defects, can be imaged as

the technique does not rely on surface diffraction. STM also has the ability to locally probe properties such as the LDOS through techniques such as scanning tunnelling spectroscopy (STS)[43, 44]. Famously in 1989 the potential of STM as a manipulation technique was eloquently demonstrated by the positioning of xenon atoms on a nickel (110) surface to form the letters “IBM”[4] and later by the creation of quantum corrals using iron atoms on the copper (111) surface[45]. This ability for STM to interact with matter on the atomic scale in addition to the extremely high resolution underlines the importance of this technique.

Despite the advantages of STM as an imaging technique, there are a couple of important drawbacks. Firstly, the sample that is to be imaged must be an electrical conductor in order for a tunnel current to flow. This has a particular impact on biological samples, which are commonly non-conductive. Secondly, a great deal of care needs to be taken when analysing STM data. It is easy to forget that the images produced are not strictly topographic images of the surface, but rather are isosurfaces of constant local density of states. As such areas of the surface with relatively higher conductance give rise to a higher tunnel current. Such features could easily be misinterpreted as raised features (c.f. Figure 3.5).

## **3.2 From Theory to Images**

This section will discuss the details of STM operation such as how the theory described in Section 3.1 is used to produce images of a surface with atomic resolution. In particular, the operation of piezoelectric tubes which are re-

sponsible for scanning the STM tip across the surface is discussed. A basic overview of the isolation used to separate the STM from external sources of vibration is also presented. Finally, the method for creating the tips used for STM scanning is described.

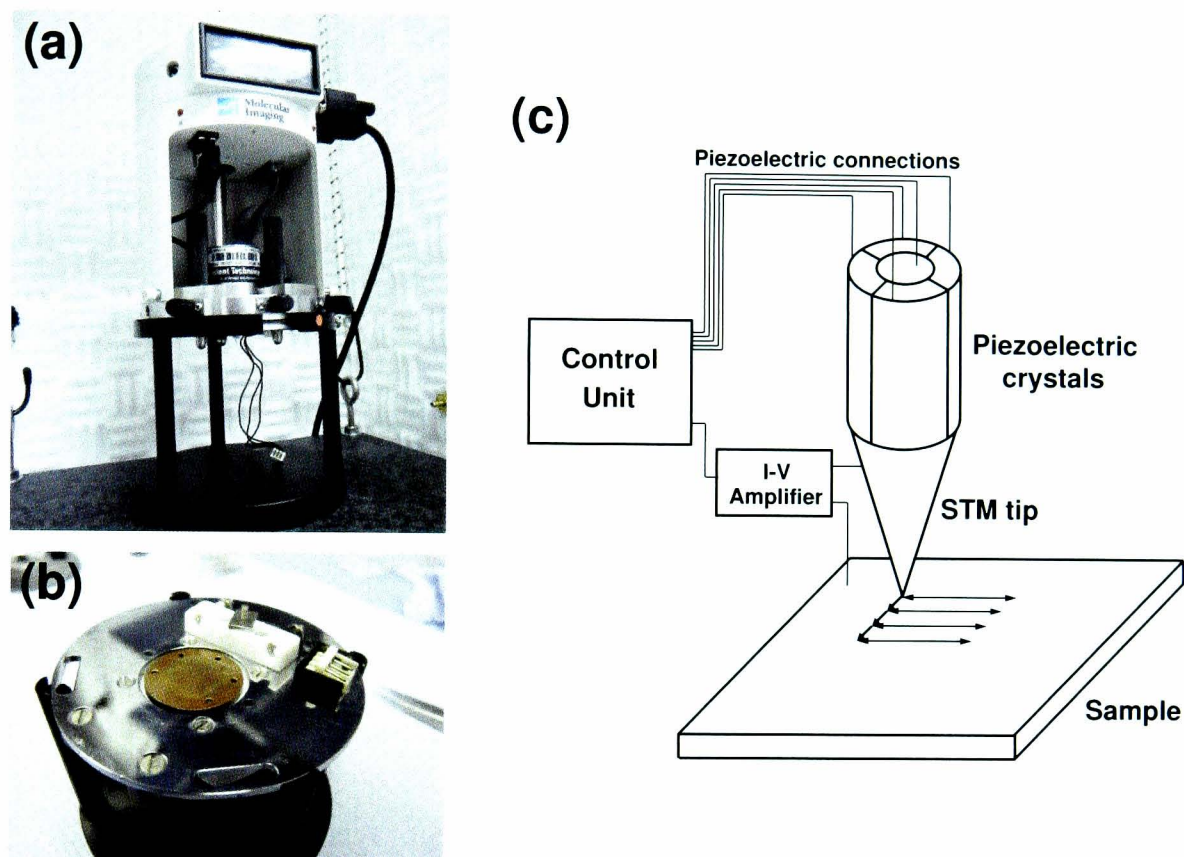


Figure 3.3: (a) A photograph of the Agilent 4500 series SPM and (b) the sample plate. (c) A schematic diagram of an STM.

Two STMs were used to take the results presented in this thesis, both of them Agilent 4500 series SPMs. Photographs of one of the systems are shown in Figure 3.3a. The STM is mounted on a platform suspended with elastic rope and operated in an acoustic chamber to isolated the system from vibrations. The sample plate is shown in Figure 3.3b. The plate is clamped magnetically under the STM probe. A schematic diagram of an STM is shown in Figure 3.3c. The piezoelectric crystals control the positioning of the STM tip as

discussed in Section 3.2.1. In order to achieve the highest possible resolution, the tip is required to be atomically sharp. Tip preparation is discussed in Section 3.2.3. A voltage bias is applied across the tip-sample junction and the resulting tunnel current amplified before being transferred to the control unit.

### **3.2.1 Piezoelectric Scan tubes**

By utilising the quantum mechanical tunnelling of electrons, extremely high vertical resolution of the surface is obtainable, as discussed in Sections 3.1.1 and 3.1.2. In order to obtain atomic resolution of surfaces however, it is vitally important that good horizontal resolution is also possible. This is achieved by performing the X-Y scanning motion using piezoelectric crystals. Applying a voltage across these materials induces a mechanical strain perpendicular to the voltage. This strain gives rise to a small change in length of the material given by the equation

$$\Delta l = d \frac{V}{t} l, \quad (3.12)$$

where  $\Delta l$  is the displacement,  $d$  is a material-specific constant,  $V$  is the applied voltage,  $t$  the thickness of the material and  $l$  the total length. For example, the ceramic PZT ( $\text{Pb}(\text{Zr},\text{Ti})\text{O}_3$ ) is commonly used in STM scan tubes[46] and has a typical value for  $d$  of  $(-1 \text{ to } -2) \times 10^{-10} \text{m/V}$ .

There are a number of different arrangements of piezoelectric material that can be used in an STM scanning mechanism. However, the most commonly used in modern STMs is the tube scanner, shown in Figure 3.4. Four different piezo crystals are used, a pair for the moving the tip in the x direction and another pair for the y direction. The electric field is applied across the material

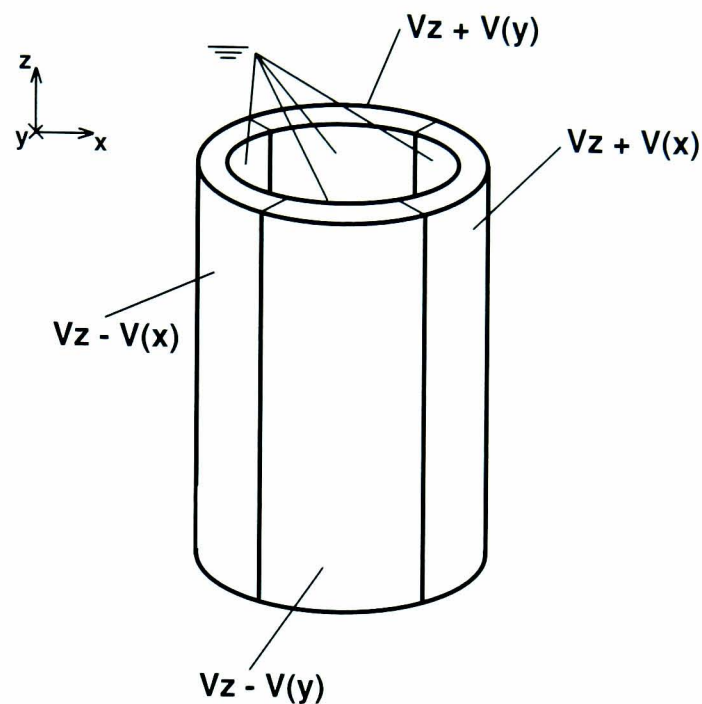


Figure 3.4: A schematic diagram of a piezoelectric STM scan tube. The tube is separated into four electrically isolated sections. The inside of the tube is grounded. The sections operate in two pairs as described in the text.

radially giving rise to strain in the  $z$  direction. This is translated to lateral  $xy$  scanning as opposite polarity voltages are applied to pairs of crystals. For example, to move the tip in the positive  $y$  direction, a positive voltage would be applied to the  $z+y$  electrode (in Figure 3.4) and a negative voltage to the  $z-y$  electrode. By equation 3.12, this results in a contraction of the  $z+y$  electrode and an expansion of the  $z-y$  electrode, twisting the scan tube in the  $y$  direction. Note that in Figure 3.4, vertical scan motion ( $z$  direction) is achieved by applying an equal voltage (denoted by  $V_z$ ) to all electrodes thus either extending or contracting them all at the same time.

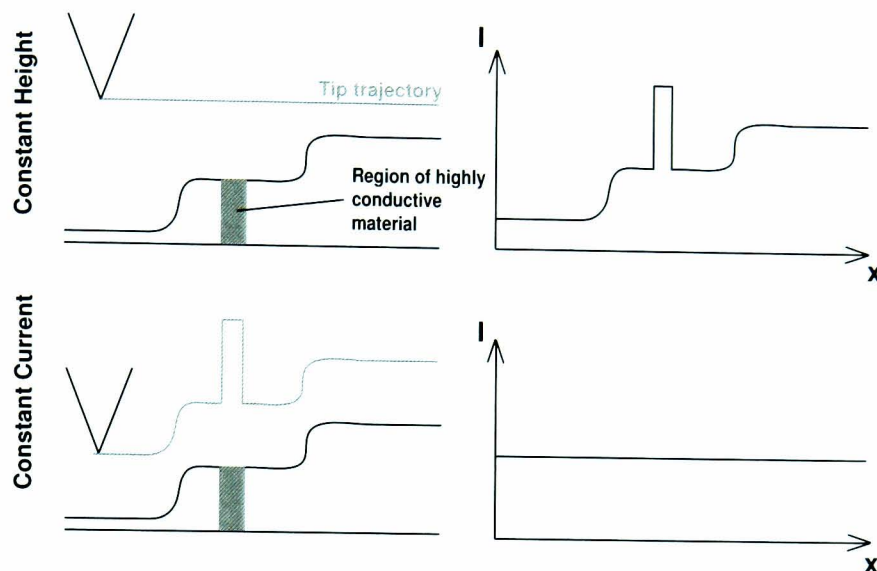


Figure 3.5: Diagrams showing the tip trajectory and ideal measured tunnel current. Under constant height mode no feedback mechanism is utilised and the  $V_z$  value remains constant. Topographic information is obtained from the current data. In constant current mode a feedback loop is used to keep the tip on a trajectory of constant LDOS. The grey region of the surface indicates a region of increased conductivity. In the constant height scan this region gives rise to an increased measured tunnel current. In the constant current mode the increased tunnelling from this region causes the feedback loop to retract the tip. Therefore despite that area of surface being topologically flat, the STM images this area as a protrusion.

### 3.2.2 STM Feedback Mechanism

As the STM tip is scanned across the surface, the changing topography will result in the tip-sample separation changing. An image of the surface can therefore be reconstructed directly from the tunnel current data. This approach is known as constant height mode in reference to the constant absolute height of the tip. The major draw back of this method is that large surface features such as step edges can cause the tip to make contact with the sample, potentially damaging it beyond repair. To avoid this, a feedback mechanism is often employed to regulate the tip-sample separation. Put simply, a target value for the tunnel current is specified and the mechanism adjusts the  $V_z$  value to maintain the tunnel current at this value. For example, if the tip

encounters a step edge resulting in a reduction in the tip-sample separation and hence a rise in the tunnel current, the feedback mechanism responds by reducing the  $V_z$  value thus retracting the tip. This increases the tip-sample separation so that the tunnel current returns to the target value. The topograph of the surface can then be deduced from the  $V_z$  voltage. The STM is said to be operating in constant current mode. Schematic diagrams illustrating the two different modes of operation are shown in Figure 3.5. As the feedback mechanism attempts to hold the tip at a level of constant current the tip will follow a trajectory of constant LDOS.

More specifically, the majority of STMs (including the ones used to obtain the results presented in this thesis) operate using a PI controller. These controllers regulate an output variable proportionally to a specified input and the history of that input. For general applications a third component is often considered; the derivative of the input history, however this is very sensitive to impulse noise and therefore not used here. For STM, the output variable is the voltage  $V_z$ , this controls the vertical position of the tip. The input signal used is a voltage proportional to the difference between the target tunnel current and the measured tunnel current values. The equation determining the output voltage is of the form

$$V_z = k_P V_{in} + k_I \int_0^{t'} V_{in}(t) dt \quad (3.13)$$

where  $k_P$  and  $k_I$  are constants relating to the proportional and integral components of the output respectively.

### **3.2.3 STM Tip Preparation**

Producing an atomically sharp tip is of vital importance for an STM experiment to be successful. If electrons can tunnel into more than one atom in the tip, the system is unable to distinguish the atomic origin of the electron, thus reducing the resolution of the resulting image. Fortunately, due to the exponential dependence of the tunnel current on distance, only the few atoms which are closest to the surface will contribute significantly to tunnelling. Therefore in tip preparation it is only a small number of atoms at the extremity of the wire that we are concerned with.

The experiments performed in this thesis have all been performed without a UHV environment. This places certain constraints on what materials can be used for the tip. For instance tungsten, which is commonly used for UHV STM experiments, oxidises in air. Tungsten oxide is non-conductive and the layer formed is sufficiently thick to make tunnelling impossible. Therefore STM experiments in atmospheric conditions commonly use a platinum-iridium (Pt/Ir) alloy. This alloy is obtainable in a number of different ratios. We use an alloy with ratio 80Pt/20Ir purchased commercially from Goodfellow.

STM tips are mechanically cut from the Pt/Ir wire as follows. A small length of wire is held firmly using long-nose pliers. Sharp tungsten carbide wire cutters are then brought into contact with the wire forming as acute an angle as possible. Rather than simply cutting the wire, the most effective mechanical tip preparation is achieved by pulling the wire through the cutters attempting to rip the end of the wire off. This on average produces a sharper tip with a higher aspect ratio than ones simply cut with wire cutters.

### **3.3 Density Functional Theory**

Density Functional Theory (DFT) is a theoretical modelling technique used to quantum-mechanically determine the ground state electronic structure of many-body systems (or critically many-electron systems). The core of the technique is based on two theorems developed by Hohenberg and Kohn ???. The first theory shows that the ground state properties of the system may be determined by the exact calculation of the electron density. This is computationally critical as it reduces the N-body problem from having  $3N$  spatial coordinates to just 3. The second theory describes an energy functional of the system that when minimised gives the correct ground state electron density. These theories are then combined with those of Kohn and Sham which converts the problem of interacting electrons in an external potential to non-interacting electrons in an effective potential. The description of the electron Coulomb interactions is then included in this effective potential.

Whilst this simplifies the problem, further approximations are still required to model the electron exchange and correlation interactions. In this thesis we use the generalised gradient approximation (GGA) proposed by Perdew et al. ?? which means the energy functional depends only on the value of the electron density at that point and its gradient. The electronic orbitals are determined from a basis set. A double numerical plus polarisation (DNP) set is used for the calculations in this thesis. DNP basis sets have polarised functions for both s and p orbitals.

In this thesis, DFT is used for determining the stability of potential molecular bonding arrangements, calculating the binding energy of such systems and

the determination of molecular orbitals. Calculations are performed without the inclusion of a substrate or the presence of any solvent molecules. The constituent atoms within the molecules are constrained to be planar with the exception of any hydrogen atoms which have no additional constraints on their movement. These omissions are to reduce the computational strain of calculations and aid conversion to a realistic answer. As such the output of our DFT simulations and the conclusions drawn need to be considered in light of this. In particular, DFT does not effectively include van der Waals-type forces in the determination of energy values which would provide a significant increase in the binding energy of many networks especially if adsorbate-substrate contributions were included.

### **3.4 TOFSIMS**

Time-of-Flight Secondary Ion Mass Spectrometry (TOF-SIMS) is an analysis technique used to determine the surface constituents of a sample. The sample is placed in an ultra-high vacuum and exposed to a rastered primary ion beam. This causes the local desorption of atoms and molecules from the sample. These secondary ions are collected into a flight path towards a detector. Mass spectrometry is performed on these ions based on their time-of-flight enabling the mass of the secondary ions to be determined with a high degree of accuracy. This reveals an accurate picture of the chemical make up at the surface of the sample. In our experiments, a primary bismuth ion source was used. A raster area of  $500 \times 500 \mu\text{m}^2$  was analysed at a resolution of  $256 \times 256$  pixels.

## 3.5 Substrate Materials

As discussed in Section 3.1, the choice of surfaces which can be studied with STM is limited to electrical conductors which are predominantly atomically flat. All of the work presented in this thesis was carried out under atmospheric conditions. This adds further limitation as some surfaces begin to form an oxide layer on exposure to air, in particular silicon which is commonly used for STM under ultra-high vacuum conditions. The oxide layer is non-conductive so a tunnel current cannot be established. In this thesis we have studied the adsorption of molecules on two surfaces, highly ordered pyrolytic graphite (HOPG) and the (111) plane of crystalline gold.

### 3.5.1 Highly Ordered Pyrolytic Graphite

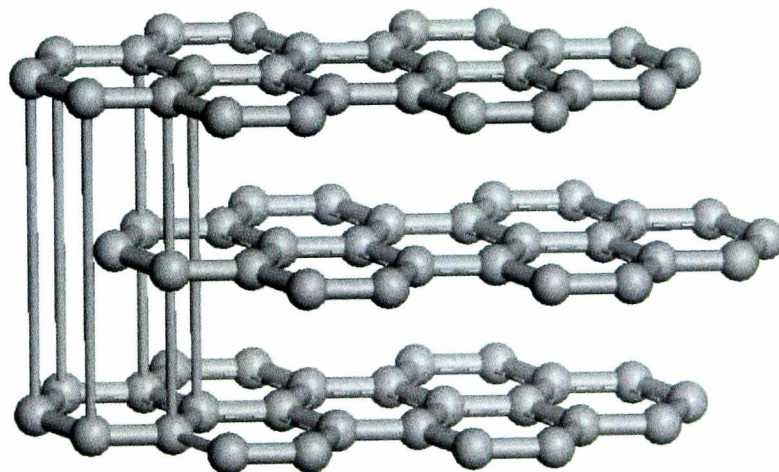


Figure 3.6: The Atomic structure of highly ordered pyrolytic graphite.

HOPG is formed by annealing pyrolytic graphite at approximately 3300K under compressive stress. This produces a high purity and highly planar carbon surface. The atomic structure of the surface is shown in Figure 3.6. Each

carbon atom in a plane bonds to three neighbours forming a hexagonal structure. The carbon-carbon bond distance is 1.42 Å. Alternating planes are separated by 3.35 Å and are laterally displaced with respect to one another by 1.42 Å such that each hexagonal ring in one plane is centred on a carbon atom in the next. Planes are loosely bound to one another by the overlapping of  $\pi$ -orbitals, known as  $\pi$ - $\pi$  stacking (c.f. Section 2.2.4). The large number of delocalised electrons within each plane make the surface highly conductive.

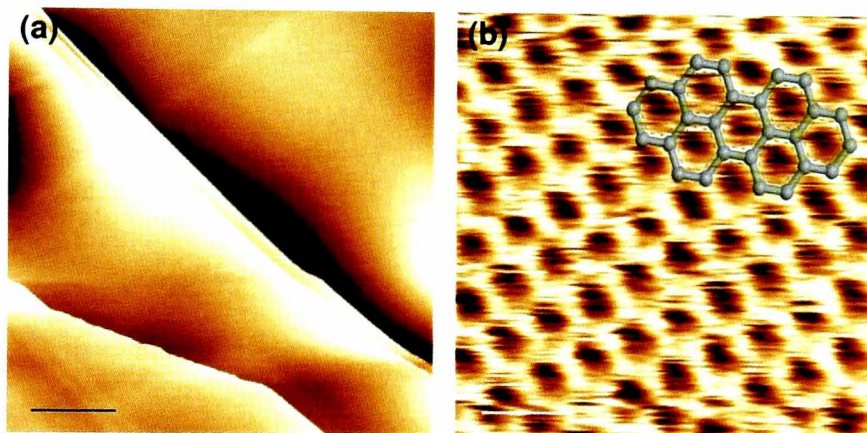


Figure 3.7: **(a)** A large STM scan of the HOPG surface showing the large, flat terraces. The scale bar is 100 nm. **(b)** A small STM scan showing the atomic structure of HOPG. A schematic is overlaid to aid identification of the atomic structure. The scale bar is 0.5 nm. Both images were taken at  $I = 1$  nA,  $V_{tip} = 0.1$  V.

A large STM scan of the HOPG surface is shown in Figure 3.7a. The majority of the surface appears flat at this magnification. Discrete lines in the STM image can be seen which correspond to the STM moving over an edge of a graphite plane (known as a graphite step edge). Typically step edges have an average separation of 150 - 200 nm. The image shown in Figure 3.7b shows a smaller scan of the graphite surface. At this magnification, the individual carbon atoms in the graphite plane can be resolved. They appear as hexagonally orientated bright protrusions corresponding to the structure of one graphite layer.

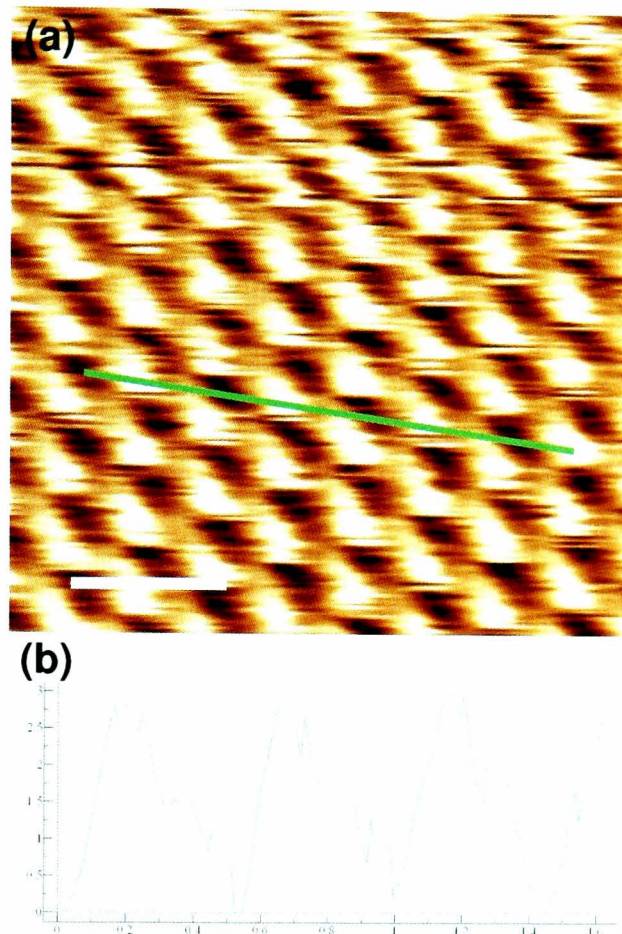


Figure 3.8: **(a)** The atomic structure of highly ordered pyrolytic graphite resolved so that three of the six carbon atoms appear bright. The green line shows the position of the line profile shown in **(b)**. The brighter carbon atoms appear with a higher apparent height than the others. Image parameters;  $I = 1 \text{ nA}$ ,  $V_{tip} = 0.1 \text{ V}$ .

Whilst obtaining atomic resolution of carbon atoms in a graphite plane is relatively trivial, it is not uncommon for the appearance of the atoms under STM to change from scan to scan. By way of example, consider the image shown in Figure 3.8. In this imaging contrast, three of the six carbon atoms in a hexagonal unit appear brighter than the other three giving rise to a triangular contrast. This effect is caused by the density of states of the top graphite layer being influenced by the layer below. The atoms that appear brighter correspond to atoms in the graphite structure with another carbon atom directly beneath them in the layer below. It is not known why the same structure

appears in different ways, the most plausible theory being related to a change in the interaction of the tip with the surface.

The highly planar nature of the HOPG surface makes it very simple to clean. As the planes are only weakly bonded to one another the top layer can be cleaved from the sample exposing a clean surface. This is done by firmly pressing adhesive tape onto the sample, ensuring that good contact is made evenly across the surface, then carefully peeling back the sample. The top few layers of graphite remain adhered to the tape, creating a new clean surface.

### **3.5.2 Gold (111)**

The second surface on which molecular adsorption has been studied is the (111) plane of gold. Crystalline gold has a face-centred cubic structure. The (111) plane of the crystal therefore has a three-fold triangular symmetry. The lattice constant of gold is 4 Å. When cleaved, the Au (111) surface is commonly reported to reconstruct into the  $23 \times \sqrt{3}$  herringbone reconstruction where 23 gold atoms on the surface layer sit on top of 22 atoms in the bulk crystal. The stacking of the atoms in this top layer changes from face-centred cubic (fcc) to hexagonally close-packed (hcp) back to fcc across the 23 atom unit cell. The mismatch between the two layers creates strain across the surface which is partially relieved by the slight buckling in the top atomic layer resulting in tramline-like features. The herringbone pattern meanders across the surface with the kinks in the structure nucleated at defects or gold adatoms[47, 48].

Gold (111) on mica surfaces were purchased from Georg Albert[49]. Samples were stored in a pressurised nitrogen atmosphere. Immediately prior to use, samples were removed from the nitrogen atmosphere and cleaned in an

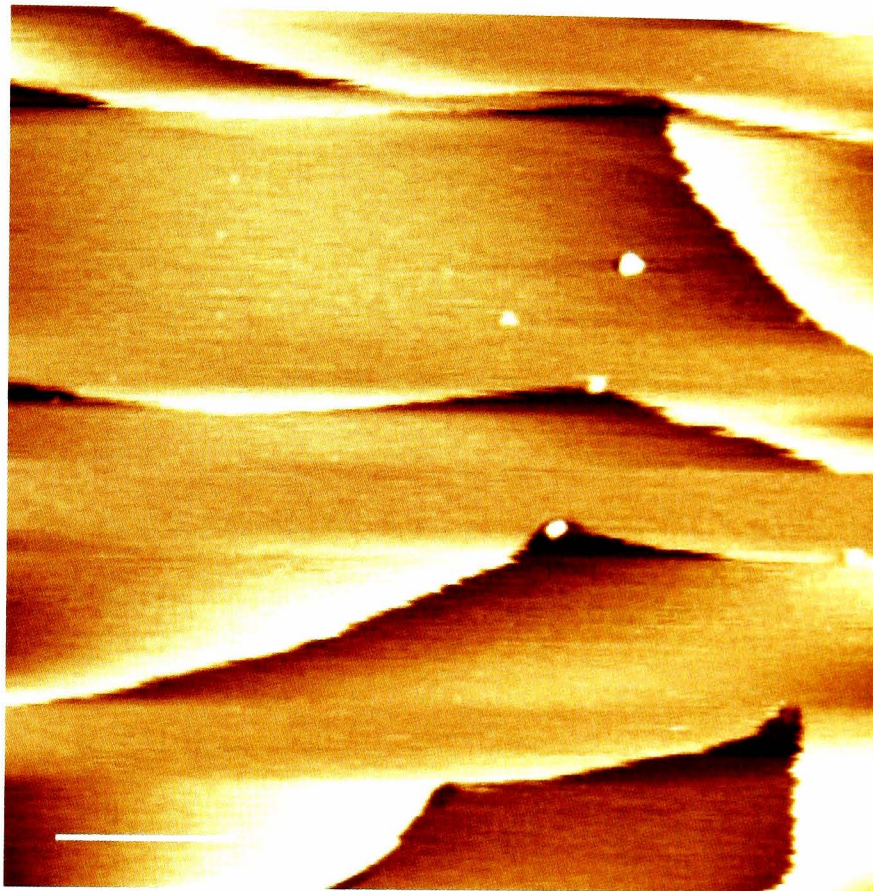


Figure 3.9: An large-scale image of the Au (111) Surface. The scale bar is 40 nm. The image was taken at  $I = 0.5$  nA,  $V_{tip} = -0.25$  V.

oxygen plasma whilst being heated to  $100^{\circ}\text{C}$  for 15 seconds. This ensured the surface was clean of adsorbates. Deposition was carried out after cleaning without any further annealing. An example STM image of a clean Au (111) surface is shown in Figure 3.9. The surface exhibits large flat terraces similar to graphite. The step edges of graphite, however, are much straighter, less frequent and more sharply defined. We do not readily observe the herringbone reconstruction in STM owing to the reduced resolution associated with atmospheric imaging and as the samples are not annealed immediately prior to imaging. It has not been possible to obtain atomic resolution of the Au (111) surface under atmospheric conditions.

## **3.6 Solution Deposition**

In this thesis, all of the results presented have been obtained by STM under liquid conditions. Without a UHV (or HV) environment, conventional molecular deposition techniques such as sublimation cannot be used. Therefore in order to deposit molecules of interest onto surfaces, we first dissolve them into a suitable solvent. The solution is then brought into contact with the surface and the molecules adsorb onto it, reducing the energy of the system. The specifics of the deposition technique is dependent on the solvent used, as detailed in subsequent sections.

The choice of solvent used depends on a number of criteria. The solvent must be able to dissolve the target molecule. It is worth noting that only a relatively small amount of the molecule needs to actually dissolve as the number required to form an extended monolayer is low. In order for the target molecule to form an extended molecular structure it must be more energetically favourable for it to adsorb onto the surface than for the solvent molecules. If this is not the case the target molecules will remain dissolved in solution and solvent adsorption will occur.

### **3.6.1 Specific solution deposition methods**

Depositing molecules from solution first requires that the powdered form of the molecule is dissolved in a suitable solvent. Typically, 1 mg of molecule is combined with 6 ml of solvent although specific values vary from experiment to experiment. The solution is then placed in an ultrasonic bath to help break up the large crystals and to ensure that both the maximum amount of solute

is dissolved in the solvent and that there is an even concentration throughout the solution. Solutions are also ultrasonicated immediately prior to deposition for these reasons. Often this produces a saturated solution as many of the molecules we have studied have limited solubility. A 10  $\mu\text{l}$  droplet of the solution is removed using a pipette and deposited onto the sample surface.

If the timescale for the evaporation of a droplet of a solvent is sufficiently long (at room temperature) that the droplet does not evaporate over the course of some hours the STM tip can be immersed directly into it and STM performed at the liquid-solid interface. This places certain additional constraints on the properties of the solvent. It must be a very poor conductor of electricity otherwise the system will short as electrons will be able to freely pass from the STM tip to the grounded sample without the need to quantum mechanically tunnel. STM tips can be insulated to get around this issue, though these require a more extended preparation procedure than using regular Pt/Ir wire. The solvent vapour must be non-toxic as the STM itself is housed necessarily in an environmentally isolated chamber. To introduce a gas extraction system would generate both noise and a considerable amount of drift into imaging.

For solvents where evaporation is rapid, the droplet will evaporate faster than it is reasonable to perform an STM experiment on the sample. Samples are therefore left until solvent evaporation has been completed before being scanned with STM at the air-solid interface.

### **3.6.2 Solvents**

In this section the atomic structures and specific experimental details relating to each of the solvents used in this work will be discussed. Experiments were

carried out using a total of four different solvents; nonanoic acid, ethanol, butanol and phenyloctane.

### Nonanoic Acid

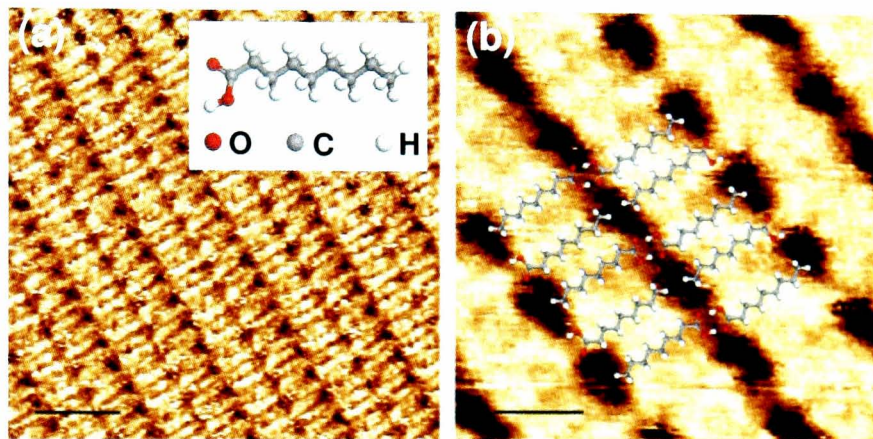


Figure 3.10: **(a)** An STM scan of nonanoic acid molecules adsorbed on the HOPG surface. The scale bar is 3 nm. The image was taken at  $I = 0.03$  nA,  $V_{tip} = 1.2$  V. Inset: Molecular ball and stick diagram of nonanoic acid. **(b)** A smaller scan of the network illustrating the alternating orientation of the molecules along the lamella structure. The scale bar is 2 nm. The image was taken at  $I = 0.03$  nA,  $V_{tip} = 1.2$  V.

Nonanoic acid (inset Figure 3.10a) is formed from a carboxylic acid group bonded to an alkane chain (nine carbon atoms). The carboxylic acid group makes the solvent an ideal candidate for dissolving molecules that also have carboxylic acid functionality as these groups can form double hydrogen bonds with themselves. The high boiling point of the solvent means that droplets take days to evaporate at room temperature. This makes the solvent an ideal candidate for in-situ STM experiments when combined with its low electrical conductivity.

An STM image of nonanoic acid adsorbed on the HOPG surface is shown in Figure 3.10. The molecules form an ordered lamellar structure. Adjacent molecules (in neighbouring rows) bond to one another through the carboxylic

groups as highlighted by the overlaid molecular diagram in Figure 3.10b. The periodicity of the lamellar rows is measured to be  $1.3 \pm 0.1$  nm consistent with the length of one nonanoic acid molecule ( $1.2 \pm 0.1$  nm). The system will be additionally stabilised by van der Waals interactions between neighbouring molecules and the surface[26]. The commensurability between neighbouring alkane chains and the underlying HOPG substrate will increase the total strength of these interactions. From close examination of Figure 3.10b, the nonanoic acid molecules do not appear to be all aligned in the same orientation. There are brighter patches within the lines of dark contrast with a periodicity of  $1 \pm 0.1$  nm. We propose that these bright features within the lines of dark contrast correspond to carboxylic acid dimer junctions. We also note that these features appear to be offset to one another from one lamellar row to the next. We attribute this to an alternation of molecular orientation as commonly described in the literature[26, 27] and illustrated by the molecular overlay in Figure 3.10b.

### Ethanol and Butanol

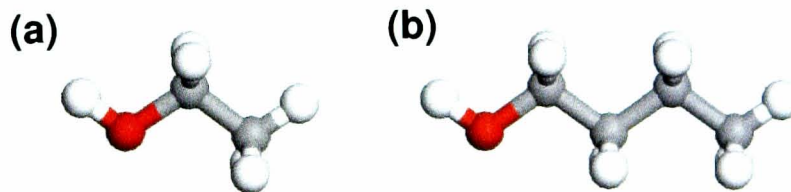


Figure 3.11: The molecular structure of **(a)** ethanol and **(b)** butanol.

Molecular diagrams of ethanol and butanol are shown in Figure 3.11. The molecules are comprised of a hydroxyl group attached to an alkane chain of either two (ethanol) or four (butanol) carbon atoms. Both molecules are highly

solubilising owing to the hydroxyl group and the shortness of the alkane chain making them suitable solvents for the liquid deposition of molecules. Experiments are performed by allowing the solution to evaporate prior to scanning with STM as droplets will not persist more than a few minutes.

### Phenyloctane

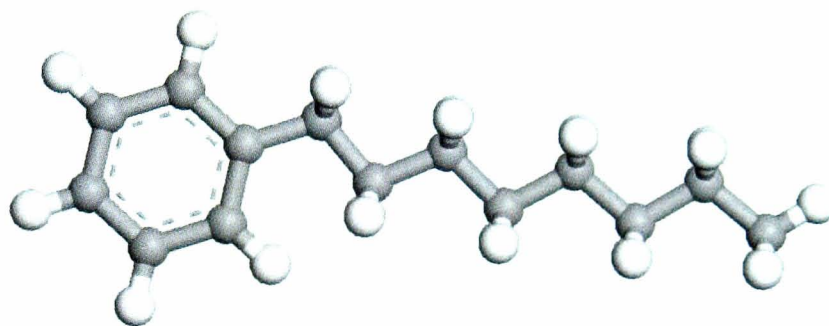


Figure 3.12: The molecular structure of 1-phenyloctane.

The structure of 1-phenyloctane is shown in Figure 3.12. The molecule is comprised of a phenyl group linked to an alkane chain eight carbon atoms long. Phenyloctane has been used extensively in the literature for the dissolution and subsequent deposition of molecules with large alkane chains[27] as the cumulative effect of the van der Waals interactions between alkane chains on the solute and solvent gives rise to a strong binding. Like nonanoic acid, phenyloctane has poor electrical conductance and a droplet will persist for much longer than the timescale of an STM experiment, STM scanning is thus performed at the phenyloctane-substrate interface.

## **3.7 Image processing**

This section will discuss the different methods and techniques used in this thesis for the processing of STM data. In particular, methods for reducing the effect of STM drift will be discussed in detail as well as compensating for a non-zero angle between the substrate and scanning X-Y planes. Finally, a number of image enhancement techniques will be presented. All image processing carried out on STM images in this thesis is performed with the WSxM software [50].

### **3.7.1 Distortion in STM images**

Image distortion in STM covers a wide range of effects each resulting from different aspects of STM operation. Effects include thermal drift, scan tube creep and hysteresis and the calibration of the piezoelectric crystals. Thermal drift is caused by the thermal expansion of components within the STM as a result of a temperature gradient. This changing temperature can be caused by external air currents or by heat generated internally in the STM. A change in temperature will crucially lead to the thermal expansion of the piezoelectric crystals resulting in the STM tip drifting in three dimensions with respect to the scan origin. For STM images, thermal drift has the appearance of stretching the image in the direction parallel to the drift. Over time the system will return to thermal equilibrium reducing the strength of the effect.

There are two main techniques used in this thesis to reduce the influence of thermal drift on distance measurements; image averaging and split molecule-substrate imaging. Image averaging requires that a number of STM images

are taken where the scan area is rotated with respect to the direction of drift. The specific distance value can then be measured and averaged from each of the images. A better method is to image both the atomic structure of the substrate and the adsorbed molecular layer in the same STM image. This is achieved by scanning the adsorbed layer with the conventional tunneling parameters for imaging the network then, half way through the scan, changing the parameters to those that reliably image the substrate. The atomic structure of the substrate is well categorised with a well defined lattice constant. The comparison of this value with one obtained from an STM image will provide a measure of the drift in the image, assuming that the drift is constant across the whole scan. A subsequent distance measurement for the adsorbed molecular layer can then be adjusted for drift.

As discussed in Section 3.2.1, piezoelectric crystals are used to perform the very small movements required for STM scanning. The expansion of these crystals can be controlled by the voltage applied across them. However, this expansion is not perfectly uniform. When the voltage across the piezotube is changed, the crystal initially expands/contracts quickly before slowing, extrapolating to the target size giving rise to the name piezoelectric creep. This effect has two implications for STM scanning. Firstly, when the scan area is moved to a new area using the piezotubes the system will need time to relax as the piezotubes expand/contract to the new position. If STM data is taken in this time, images will have the appearance of non-uniform drift as the piezotube creep exponentially reduces over time. Secondly, as the STM uses piezoelectric crystals to scan the surface. The piezoelectric creep will occur as the tip approaches the edges of the scan, known as scan tube hysteresis. This

leads to distortion of STM images at the edges of the fast scan direction. To compensate for this, an overscan is often used whereby the STM scans a larger area than is desired and the data is only taken from the middle of the scan region where piezoelectric creep is minimized.

### **3.7.2 STM image flattening**

In STM it is highly unlikely that the tip will be perfectly perpendicular to the surface giving rise to a non-zero angle between it and the z direction. In resulting STM images, the sample surface will appear to be at a steep gradient which normally masks any observable detail. To compensate for this a plane is fitted based on the line scans which is then subtracted from it. This removes the gradient and reveals the residuals of the global plane, i.e. the detail of the surface features.

### **3.7.3 STM image enhancement**

Whilst the above experiment and processing techniques are often essential in producing an STM image from which meaningful conclusions can be drawn, there are a range of additional image processing techniques which can be used to enhance specific features in an image or improve the overall quality. Those techniques that have been used for STM image enhancement in this thesis will now be discussed.

A histogram equalisation has been applied to every STM image we present. The technique is a basic contrast enhancement whereby the greyscale brightness values are remapped between 0 and 255 such that a cumulative histogram

of the image becomes a straight line. It has the effect of broadening or flattening a histogram of number of pixels against pixel value such that the distribution of pixel height values becomes more even, giving rise to an increased contrast. This technique is a simple reassignment of the pixel height values, thus it does not fundamentally manipulate the data. Histogram equalisation can also be used to enhance a specific range of pixel values. This is achieved by only considering this range when performing the equalisation and thresholding values outside of this to 0 or 255.

In any image, reducing noise is important and highly desirable. Often this can be achieved through good experimental setup and procedure alone. However in some cases, additional post-experiment noise reduction techniques are required. For a number of images in this thesis additional noise reduction was utilised, specifically Gaussian smoothing. The noisy STM image is convoluted with a 2D Gaussian function, blurring the image. It is particularly effective at removing high frequency “speckle” noise, in a similar way to a basic pixel-averaging technique. The noise reduction does come at the price of reduced spatial resolution, hence this technique has been used sparingly in this work and only where stated.

## **3.8 Conclusion**

In conclusion, this chapter has presented an overview of the fundamental theory used in STM. The implications and limitations of the theory were then discussed. Section 3.2 reviews how in practise STM theory is translated into images of the surface. A summary of the substrate materials used for exper-

*CHAPTER 3. Experimental Techniques.*

---

iments in this thesis is presented as well as the solvents and deposition techniques used. Finally a explanation of the image processing and enhancement techniques that have been performed on images is included.

## Chapter 4

# The different adsorption morphologies of two carboxylic acid derivatives

*We have investigated the supramolecular networks formed by two carboxylic acid tectons when deposited from nonanoic acid on the HOPG surface. The first, quaterphenyl-tetracarboxylic acid (QPTC), forms a parallel network where each molecule bonds to its four neighbours via carboxylic acid dimer bonds. The second tecton studied was terphenyl-tetracarboxylic acid (TPTC). Unlike QPTC, TPTC forms a hexagonally ordered network with no translational symmetry. The molecules were found to order themselves in one of three different directions forming a total of five different conformations around the hexagonally ordered pores. We show that the TPTC network maybe represented as a tiling of rhombi and by following previously identified mathematical techniques, we determine that the disordered nature of the network is stabilised*

*by the entropic contribution to the free energy. The role of topological defects is discussed and we show that the propagation of so called triangular defects provides a mechanism for morphological re-ordering, equivalent to transferring between the near-degenerate ground states of the system.*

*Such defect diffusion events are rare and very localised. In order to investigate larger changes in network morphology the evolution of TPTC domain boundaries has been studied. We show that large changes in morphology can occur at these boundaries as a result of the dynamic nature of the network growth. Finally we demonstrate the direct manipulation of the network morphology by the tip-directed formation of close-packed TPTC domains and their subsequent relaxation forming a network with a perturbed statistical distribution of pore types.*

## **4.1 Introduction**

Supramolecular chemistry is sufficiently well understood that molecules can be synthesised with a specific functionality so that when deposited on a surface they will form a pre-targeted molecular structure[51, 52]. Strong hydrogen bonds are particularly suited to directing network formation as they are intermediate between being robust enough to produce stable molecular structures and yet weak enough to allow the diffusion of molecules into the lowest energy configuration[32, 53]. Carboxylic acid moieties are particularly suitable as a primary hydrogen bonding group as they preferentially form dimers[54, 55, 56]. The highly directional nature of these dimers limits the bonding angle between molecules resulting in increased control over the possible molecular structures.

The carboxylic acid dimer interaction is the principal hydrogen bonding junction for all of the molecules discussed in this chapter.

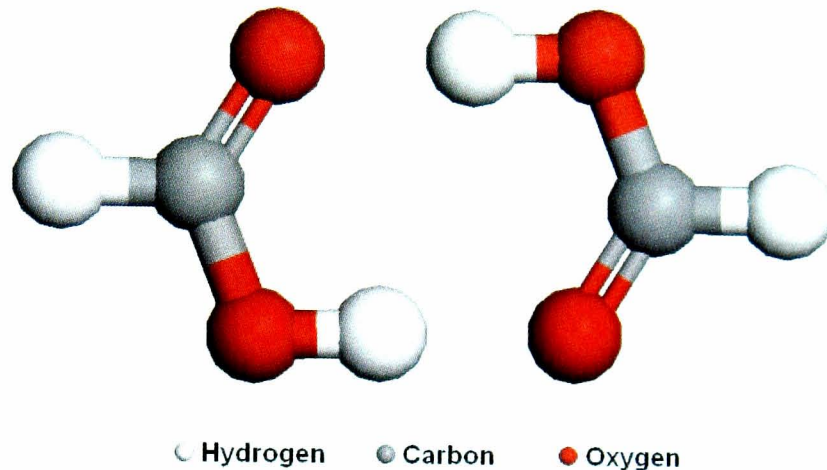


Figure 4.1: A DFT simulation of a carboxylic acid dimer.

In order to gain further insight into the carboxylic dimer interaction, density functional theory (DFT) simulations have been performed on the junction. The stabilising energy was found to be 0.76 eV per junction. The energy was found by calculating the total energy of the dimer system, shown in Figure 4.1, and subtracting this from twice the total energy of a single carboxylic acid moiety. The equilibrium separation of the carbon atoms was found to be 3.77 Å.

Molecules with carboxylic acid functionality have been used previously in the formation of supramolecular structures, most noticeably in the formation of trimesic acid (TMA) layers on a number of surfaces[23, 57, 58, 59]. The three carboxylic acid groups create a strong energetic preference for the formation of a hexagonal network where each TMA molecule participates in three carboxylic acid-carboxylic acid bonds. Other, more complex structures have been observed and it would appear that the choice of solvent molecule is partic-

ularly influential in determining which is the most energetically stable[19]. In our research we have studied the network formation of the two carboxylic acid tectons[60] terphenyl-3,5,3',5'-tetracarboxylic acid (TPTC) and quaterphenyl-3,5,3',5'-tetracarboxylic acid (QPTC) shown in Figure 4.2a and b respectively.

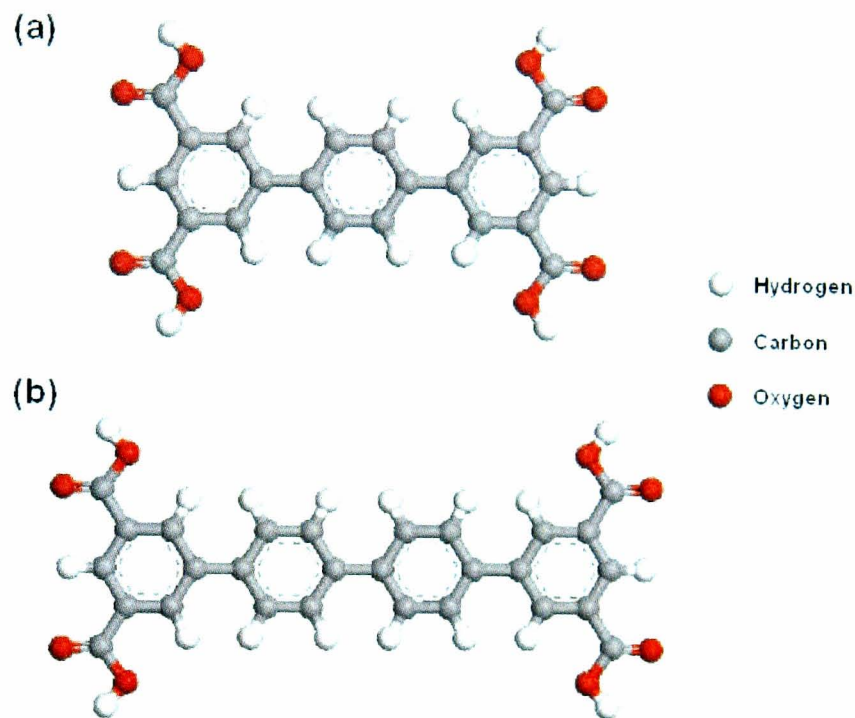


Figure 4.2: Schematic diagrams of the (a) TPTC and (b) QPTC molecules.

## 4.2 Experimental

The synthesis of the TPTC and QPTC molecules has been published in our previous work[61, 62]. Saturated solutions of the TPTC and QPTC molecules in nonanoic acid were prepared and ultrasonicated immediately prior to deposition. This was to ensure that the solution was truly saturated as the solubility of both molecules is relatively poor. For both experiments, a 10  $\mu$ l droplet of solution was deposited on a freshly cleaved, high oriented pyrolytic graphite (HOPG) surface. Samples were imaged with a STM operating at the nonanoic

acid-HOPG interface under atmospheric conditions. STM tips mechanically cut from 80/20 Pt/Ir wire were prepared in advance and their quality tested by imaging the HOPG in air. The STM chamber was allowed to settle for up to two hours prior to advancing the STM tip into tunnelling to minimise image drift due to atmospheric disturbance. Once approached, voltage pulsing was used to improve tip resolution. Typical values ranged from 3-5 V with a 200 $\mu$ s duration. If the resolution was particularly poor, larger 10 V pulses were used and failing that, a new STM tip was cut. All images presented in this section were taken with the voltage bias applied to the STM tip.

### 4.3 QPTC Results

A typical STM scan of the QPTC network is shown in Figure 4.3. The aromatic backbone of the molecule appears bright in the STM scan, with detail of the individual phenyl groups visible. The central two groups appear brighter than the two isophthalic groups. We observe a greater than 90% coverage of the HOPG surface. The backbones of the molecules lie parallel to one another forming a parallel network. The inset in Figure 4.3 highlights the packing of the molecules. Each molecule participates in four carboxylic acid dimer bonds which stabilises the network. By taking measurements from multiple images acquired with different scan directions, the effect of thermal drift can be eliminated and a value for the molecular separation determined. We found the values of **a** and **b** to be  $2.0\pm 0.1$  nm and  $2.1\pm 0.1$  nm respectively, in excellent agreement with previous work[63]. Closer inspection of the images reveals the presence of a periodic modulation of the network contrast. The periodicity of

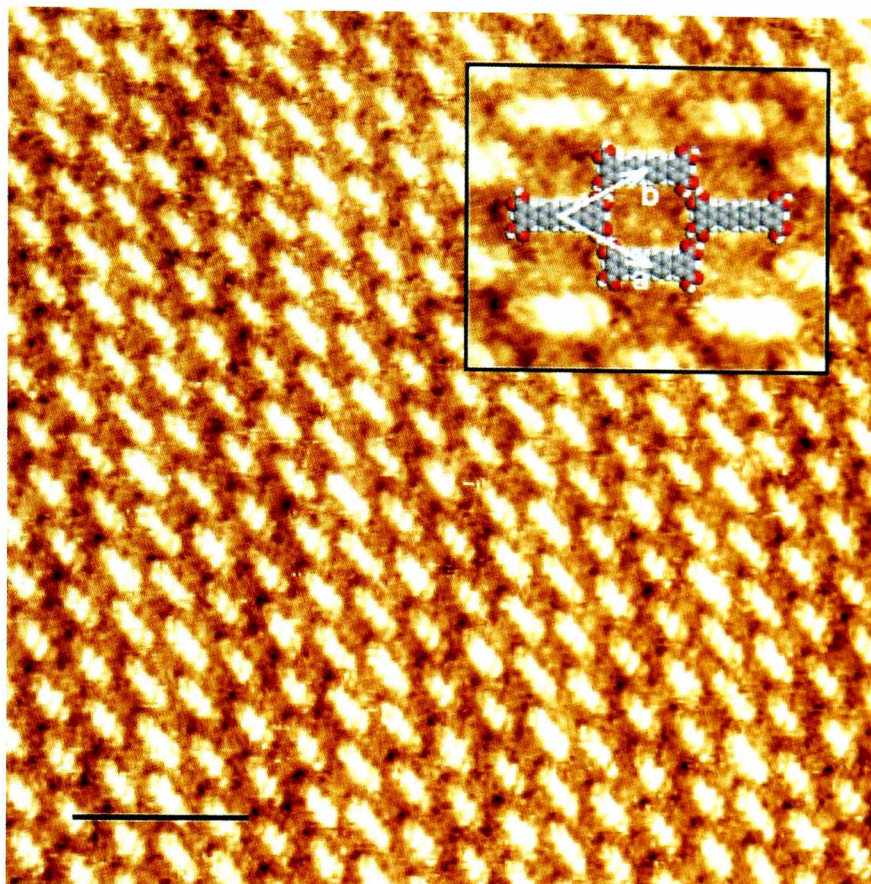


Figure 4.3: An STM scan of the QPTC network formed at the nonanoic acid/HOPG interface. The white arrows indicate the unit cell vectors. The image was taken at  $I = 40$  pA,  $V_{tip} = 1.1$  V. The scale bar is 6 nm.

this feature can be enhanced by computing the Fast Fourier Transform (FFT) of this image. This produces a k-space image showing the spatial frequencies of the image (Figure 4.4a (inset)). Figure 4.4b shows the image with the contrast modulation enhanced. The periodicity of this feature is measured to be  $7.2 \pm 0.6$  nm.

In order to investigate the origins of the periodic banding we have produced a model of the QPTC structure adsorbed on the HOPG surface. A schematic diagram is shown in Figure 4.5. The pair of black lines indicates rows of molecules which have equivalent substrate adsorption sites. The molecules are related by a translation of  $4\mathbf{b}$ . The perpendicular separation of the black lines

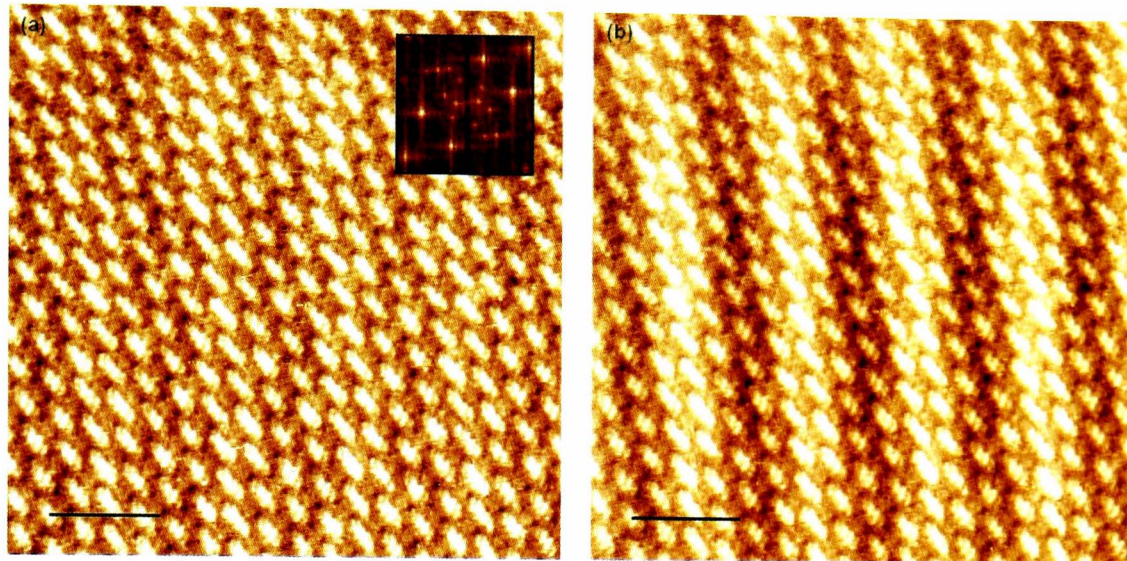


Figure 4.4: (a) The STM scan of the QPTC network shown in Figure 4.3 with the corresponding FFT shown in the inset. The two peaks closest to the origin correspond to the modulating contrast across the network. (b) The image shown in (a) with the contrast modulation enhanced for clarity. Both scale bars are 6 nm.

is therefore calculated to be  $7.5 \pm 0.4$  nm. As the periodicity of the contrast modulation is in agreement with this value, it suggests that the banding we observe is a Moiré pattern formed from the mismatch between the substrate and adsorbed molecular layer.

Another STM image is shown in Figure 4.6. The QPTC molecules used in this experiment came from a later synthetic run. There appear to be two distinct molecular species present in the sample. The separation of the two molecular species is determined to be  $2.8 \pm 0.3$  nm and  $1.9 \pm 0.1$  nm. This suggests that a larger molecular species forms interstitial rows commensurably in the QPTC bulk network. From consideration of the molecular size and the synthetic technique it is likely that this impurity is hexaphenyl-3,5,3',5'-tetracarboxylic acid (HPTC). We suspect that this impurity arises during the chemical synthesis. *Ceteris paribus*, it stands to reason that the larger HPTC molecule has a stronger interaction with the HOPG surface, by virtue of being

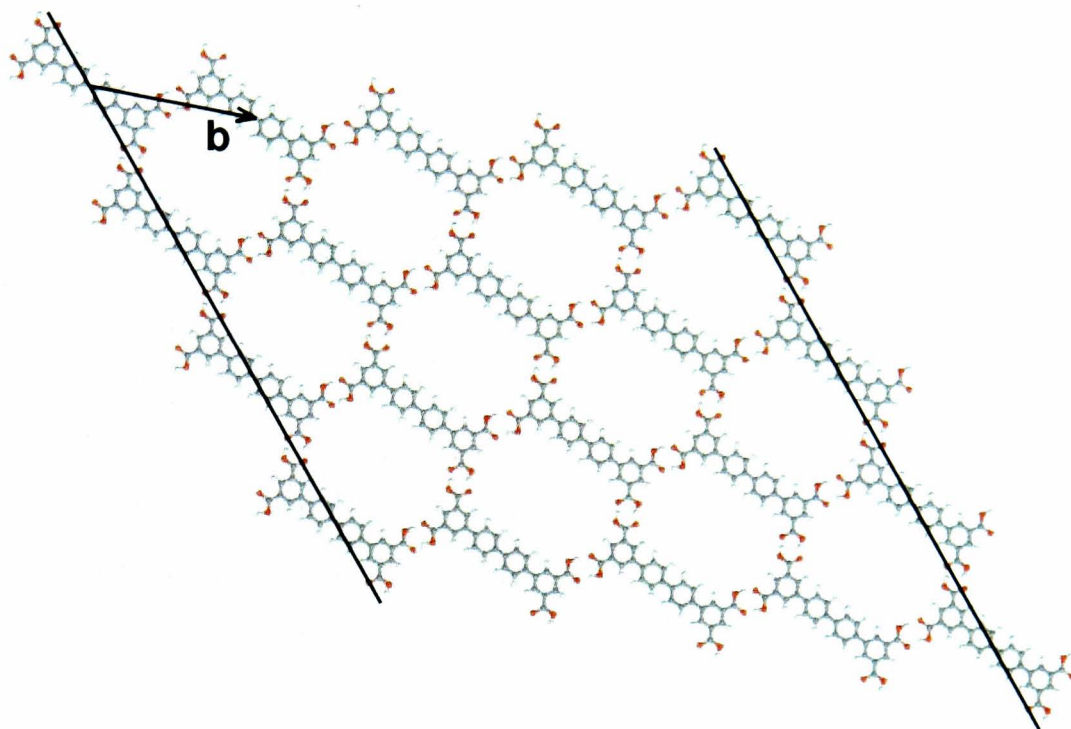


Figure 4.5: A schematic diagram showing the adsorption of QPTC molecules on a HOPG surface. The black lines indicate rows of molecules with equivalent adsorption sites.

larger, thus increasing the probability of adsorption relative to QPTC. Hence even for very small concentrations, it can become a prominent feature of the molecular network. It is also worth drawing special attention to the fact that the HPTC molecules form interstitial rows in the QPTC bulk network instead of forming domains of pure HPTC. Such rows can link to QPTC rows without forming defects as the chemical structure of the isophthalic groups is identical. However the change in molecular backbone length means only similar molecules can adsorb along the row without the formation of defects.

The model shown in the inset of Figure 4.3 and which is also discussed in previous work [63] implies that the QPTC parallel network is not only porous, but that those pores are vacant. Close examination of the STM images of the network suggest that this is not the case. But it has not been possible to

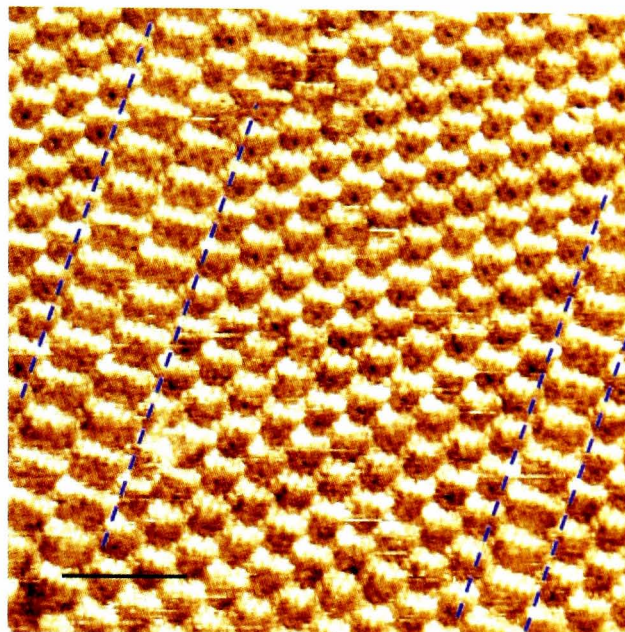


Figure 4.6: An STM scan of the QPTC network formed at the nonanoic acid/HOPG interface. Rows of HPTC impurity highlighted between the blue dashed lines can be seen interspersed amongst the QPTC network. The image was taken at  $I = 50$  pA,  $V_{tip} = 1$  V. The scale bar is 6 nm.

obtain resolution of any constituent. The most persuasive argument is that solvent molecules co-adsorb into the pores of the network, lowering the total energy. The adsorption of nonanoic acid onto the HOPG surface has already been described in Section 3.6.2, thus co-adsorption is certainly a feasible explanation. From simple geometric constraints it is unlikely that more than one or two solvent molecules would be able to adsorb into any one QPTC pore resulting in the solvent molecules being loosely bound to the structure and hence difficult to image using STM. It could also be argued that adsorption of another QPTC molecule occurs, but a simple geometric argument would imply that the molecule would have to adsorb in a relatively unconventional way, suggesting that this would be energetically unfavourable.

## 4.4 TPTC Results

An example STM image of the TPTC network is shown in Figure 4.7a. The TPTC molecules appear as bright rod like features on the HOPG surface, with the middle benzene group appearing the brightest of the three. Unlike the quarterphenyl version of the molecule however, the TPTC molecules do not all lie parallel to one another. The formed structure is much more complex. All the molecules lie on a hexagonally symmetric lattice and each molecule is oriented in one of three different directions, at  $120^\circ$  to each other. This hexagonal symmetry is highlighted in Figure 4.7a by the green circles located over the centres of the network pores. We can therefore determine that a level of order is present in the network. However, unlike the vast majority of observed hydrogen-bonded structures formed by molecules on HOPG, there is no extended translational symmetry of the molecules.

The larger scan shown in Figure 4.7b shows that this unusual network morphology occurs over extended areas of the surface. We estimate the total surface coverage of network to be at greater than 90%. The periodicity of the hexagonally ordered pores was determined from a split image of half the TPTC network and half the HOPG substrate. This is achieved by first imaging the TPTC network and half-way through the image changing the tunnel current and/or bias voltage to those which will image the substrate, shown in Figure 4.7c. A measurement of the separation of carbon atoms in the substrate and subsequent comparison to the accepted values gives a measure of the drift. The molecular separation can therefore be scaled accordingly. The pore to pore separation was determined to be  $16.6 \pm 0.8$  Å. It is worth mentioning at this

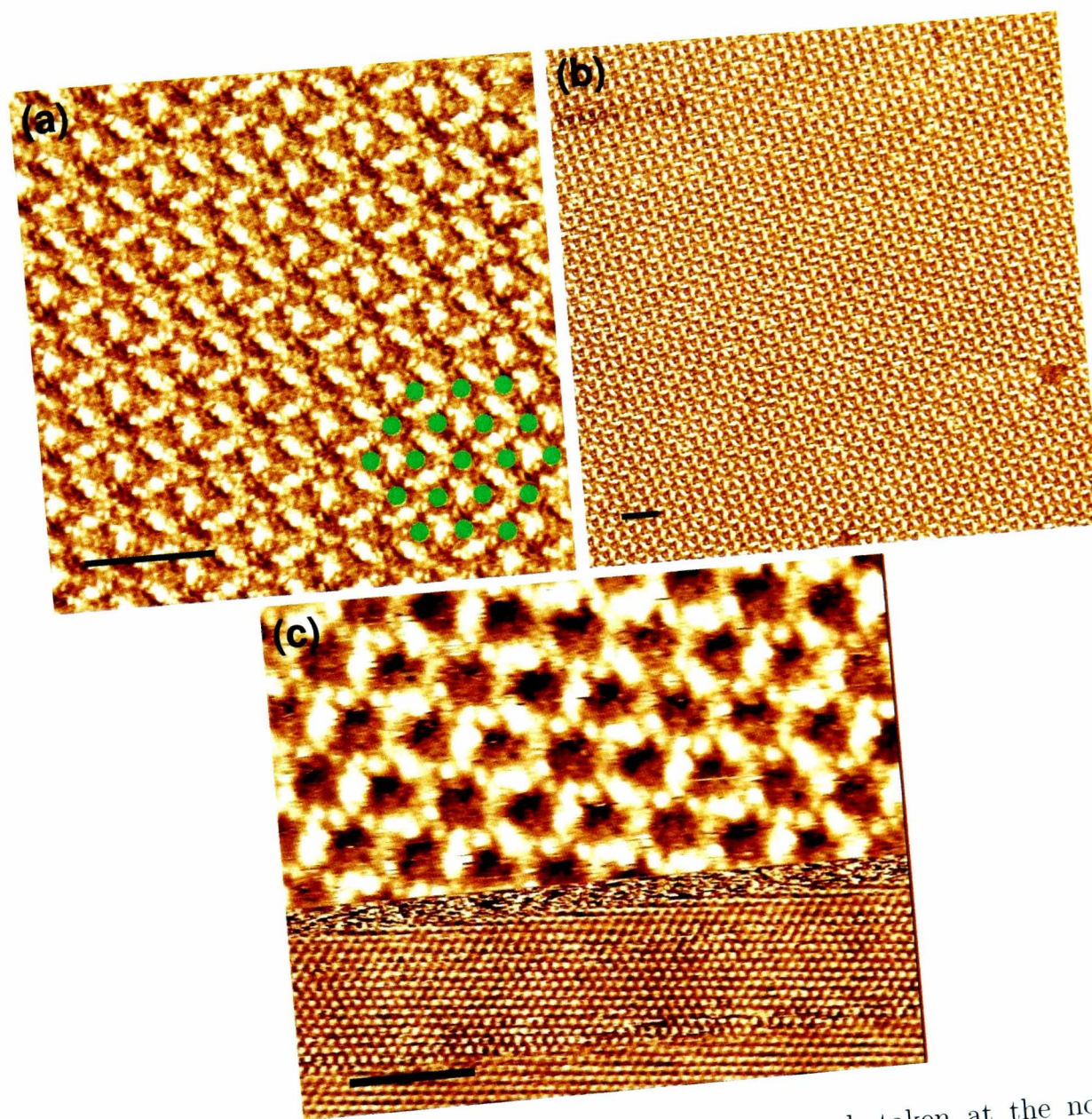


Figure 4.7: (a) An STM image of the TPTC network taken at the nonanoic acid/HOPG interface. The image was taken at  $I = 150$  pA,  $V_{tip} = 1$  V. The scale bar is 5 nm. (b) A larger scan of the TPTC network showing that the morphology is extensive across the surface. The image was taken at  $I = 135$  pA,  $V_{tip} = 1$  V. The scale bar is 5 nm. (c) A composite image showing the TPTC network (top) and the underlying HOPG substrate (bottom). The tunnelling parameters are changed half way through the image from those which image the adsorbed TPTC molecules ( $I = 5$  pA,  $V_{tip} = 1.2$  V) to those that image the substrate ( $I = 1$  nA,  $V_{tip} = 0.1$  V). The scale bar is 3 nm.

stage that commonly the reverse image contrast is measured where the pores of the TPTC network appear bright and the actually molecules darker. Thus images of the system show a hexagonally ordered arrangement of dots (the pores). In this contrast, no detail of the molecules themselves is visible thus the determination of molecular morphology is not possible. We believe that the specific state the tip is in plays a critical role in determining the imaging contrast as imaging can switch between the two without external input.

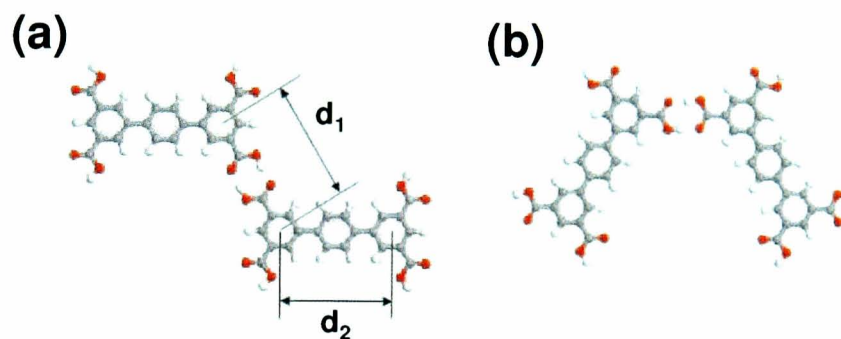


Figure 4.8: A schematic diagram showing the two distinct bonding arrangements of two TPTC molecules.

After careful examination of a number of STM images we determine that there are only two distinct TPTC bonding orientations. These two admolecule-admolecule bonding geometries are shown in Figure 4.8. The first, shown in Figure 4.8a has the aromatic backbones of the two molecules lying parallel to one another. The second arrangement, known as the anti-parallel orientation (Figure 4.8b) has the molecular backbones rotated  $60^\circ$  to one another. In both geometries, the TPTC molecules form a single carboxylic-carboxylic acid hydrogen bond. In order to determine if there is any energetic difference in these two geometries, we have performed DFT calculations[61]. The values for  $d_1$  and  $d_2$  were determined to be  $9.6 \text{ \AA}$  and  $8.7 \text{ \AA}$  respectively. The binding energy of both systems was determined to be  $0.80 \text{ eV}$ .

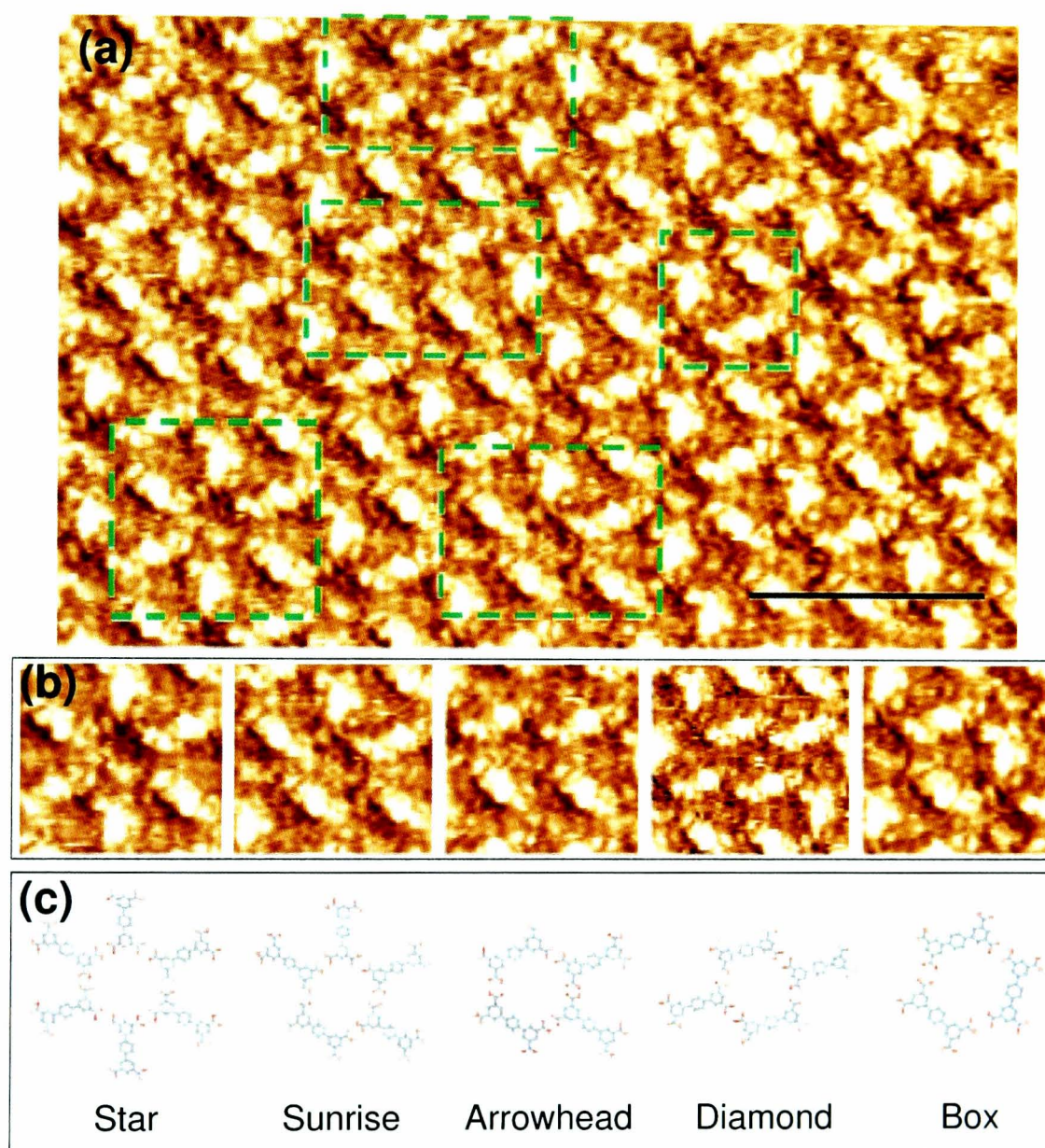


Figure 4.9: (a) A section of the image shown in Figure 4.7a with examples of the five distinct pore types sectioned in the green dashed boxes. (b) Images of the five pore types and beneath them in (c) are the corresponding molecular schematic diagrams.

Despite the TPTC molecules only bonding in two ways, five different unique arrangements of TPTC molecules around any network pore are observed. We refer to these as “pore types”. The arrangements are highlighted in the network shown in Figure 4.9a. The first pore type (from left to right in Figure 4.9b) is a hexaisophthalate pore similar to that found in the trimesic acid (TMA) chickenwire structure[23]. This pore is formed from six TPTC molecules all forming non-parallel hydrogen bonds with each other. The second pore type is a five-membered pore formed from three non-parallel hydrogen bonds and two parallel bonds. Thirdly, a four-membered pore which has two non-parallel and two parallel bonds. Fourthly, another four-membered pore which is similar to the parallel structure formed by the QPTC tecton which exhibits four parallel hydrogen bonds. Finally, a three-membered pore type which has three non-parallel bonds. For clarity these pores will be referred to as *star*, *sunrise*, *arrowhead*, *diamond* and *box* respectively. In order to statistically determine the relative abundance of each of the five pore types, multiple images of sizes ranging from 50x50 to 100x100 nm<sup>2</sup> were analysed. We determined the distribution of pore types to be 13.3%, 18.4%, 19.8%, 1.3% and 47.3% for each type respectively.

#### 4.4.1 Analysis

The molecular networks which are commonly reported in the literature normally exhibit translational symmetry. There are only a few examples of disordered molecular systems[16, 64]. In order to analyse the glassy morphology of the network we perform a one-to-one mapping of TPTC molecules to lozenge rhombi as follows. In Figure 4.7a we highlighted the hexagonal ordering of the

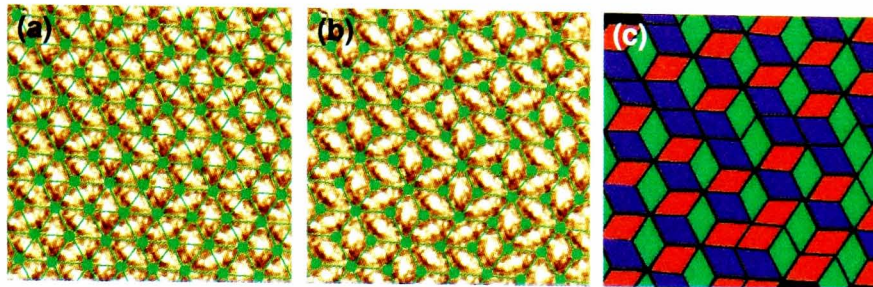


Figure 4.10: **(a)** A section of the image shown in Figure 4.9a with the hexagonal order utilised to form a triangular grid. **(b)** The grid lines that intersect molecules have been removed to produce a tiling of rhombi. On subsequent tilings, the rhombi are coloured according to orientation.

pores. Drawing lines intersecting all the pores illustrates that the network lies on a triangular lattice, shown in Figure 4.10a. Each adsorbed TPTC molecule takes up exactly two triangles of the lattice. Removing the lines that bisect TPTC molecules (Figure 4.10b) produces a tiling of rhombi with internal angles of  $60^\circ$  and  $120^\circ$ . We note that the rhombi orient themselves in one of three directions and now the carboxylic acid dimer bonds are located at the midpoint of the rhombus edges. Alternatively, the formation of a rhombus tiling can be thought of as replacing every TPTC molecule in a STM image with a lozenge rhombus completely tiling the image. Subsequently we colour tiles by the orientation to aid visualisation as shown in Figure 4.10c.

### Height Function Analysis

Rhombus tilings have been studied theoretically before and related to experimental systems in fields such as ferromagnetism[65, 66]. In order to determine whether the rhombus tilings produced from the TPTC network are truly random, we utilise the mathematical techniques available in the literature[67, 68, 69, 70]. We introduce an effective tiling height by defining an arbitrary origin at a tiling vertex then, using the scheme in Figure

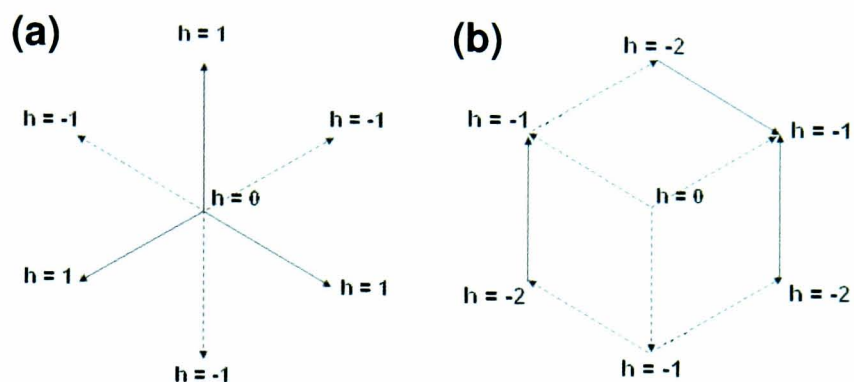


Figure 4.11: (a) The scheme for determining the height function of a point relative to an origin. (b) An example showing a box pore and the height values of the points surrounding it.

4.11a, we can determine the height of all other vertices relative to this point. It is the equivalent of considering the rhombus tiling as the projection of a three-dimensional surface where points of equal “height” correspond to points in the same (111) crystallographic plane. Areas of higher or lower height will correspond to the (111) planes above or below that plane in a similar way to contours on a map. The rhombi are then coloured by calculating the average height value from the height of the four adjacent vertices.

However, this height scheme only holds true for defect free tilings. Whilst vacancies in the network have no effect on the height function, triangular topological defects result in the height function becoming multivalued. Their effect is analogous to screw dislocations in a crystal structure resulting in a nonzero change in the height function for a closed path around them. The net change in the height function around a closed path enclosing a triangular defect is  $\pm 3$ [70, 71].

The rhombus tiling produced from a  $100 \times 100 \text{ nm}^2$  STM image is shown in Figure 4.12a and the corresponding height function is shown in Figure 4.12b. The colour scale in the height function is hot/cold with the hotter colours

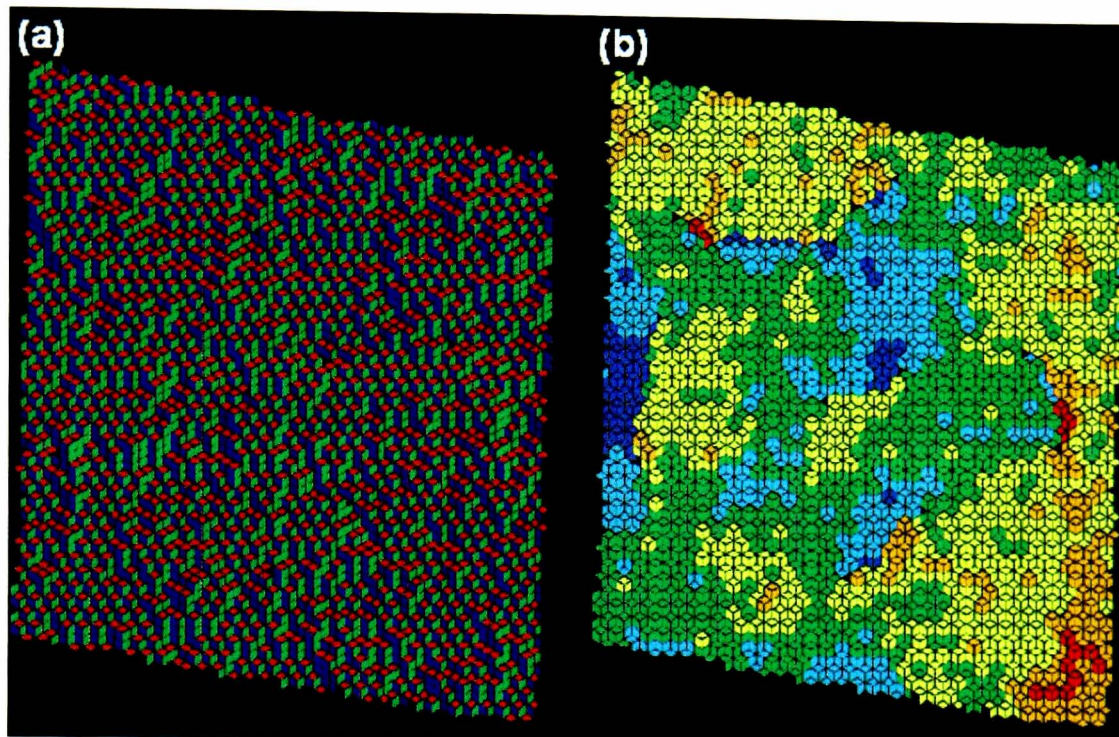


Figure 4.12: **(a)** The rhombus tiling of an 100x100 nm<sup>2</sup> STM image. **(b)** The height function of the tiling shown in **(a)**.

corresponding to higher height values. The lines that connect defects with opposite charge have not been illustrated but are clearly visible from jumps in the height function colour. We also note the effect on the height function of each of the different pore types. The rhombi that form star and box pores (defined in Section 4.4) all have the same average height value, implying there is no change in the height function across them. The sunrise, arrowhead and diamond pores however, all contain a non-equal number of each of the three orientations of tile, implying that they result in a change in the height function. Ordered networks can be formed using either just the diamond pore type, for example the structure formed by the QPTC system (Section 4.3), or a combination of the star and box pores (such as that formed by the QPTC-coronene network in Section 5.2.1). The former would have a height function which was a constant gradient from one side of the image to the other (essentially a

sloped height function). The latter would have a perfectly flat height function of where all the tiles are the same colour. A height function that tends towards one of these implies that the network is closer to an ordered state.

To further our tiling analysis, we introduce an effective elastic free energy of the system. We assume that all possible tilings are degenerate and that the numbers of each of the three orientations of tile are equal. The first assumption implies that the effective internal energy of a tiling will be much less than the entropic contribution. Therefore,

$$F = -S \quad (4.1)$$

in units of  $k_B T$ , where  $k_B$  is Boltzmann's constant. The second assumption implies that the entropy density will be at a maximum in this case (Henley elegantly relates this to a mixture of gases having maximum entropy when each component has equal density[72]). We refer to the literature where for any maximally random tiling, the entropy density is given by

$$\sigma(\nabla h) - \sigma(0) = -(K_0/2)|\nabla h|^2 + O(|\nabla h|^n) \quad (4.2)$$

where  $O(|\nabla h|^n)$  refers to higher order terms in  $\nabla h$ . As the entropy density is at a maximum, we can simplify equation 4.2 by only considering the term in  $|\nabla h|^2$ . Thus the free energy for the whole tiling may be expressed as

$$F = (K_0/2) \int |\nabla h|^2 d\mathbf{r}. \quad (4.3)$$

This may be expressed in terms of the Fourier transform of  $h$ ,  $H$  as

$$F = (K_0/2) \int |H|^2 |k|^2 d\mathbf{k}. \quad (4.4)$$

Henley then shows that fluctuations in this energy can be expected with a power spectrum  $\langle h_k^2 \rangle \propto K_0^{-1} |k|^{-2}$  leading to real-space logarithmic spatial correlations of

$$C(r) = \langle [h(0) - h(r)]^2 \rangle = (\pi K_0)^{-1} \ln(r) + c \quad (4.5)$$

where  $c$  is a constant. For maximally random rhombus tilings  $K_0 = \pi/9$  [72, 70].

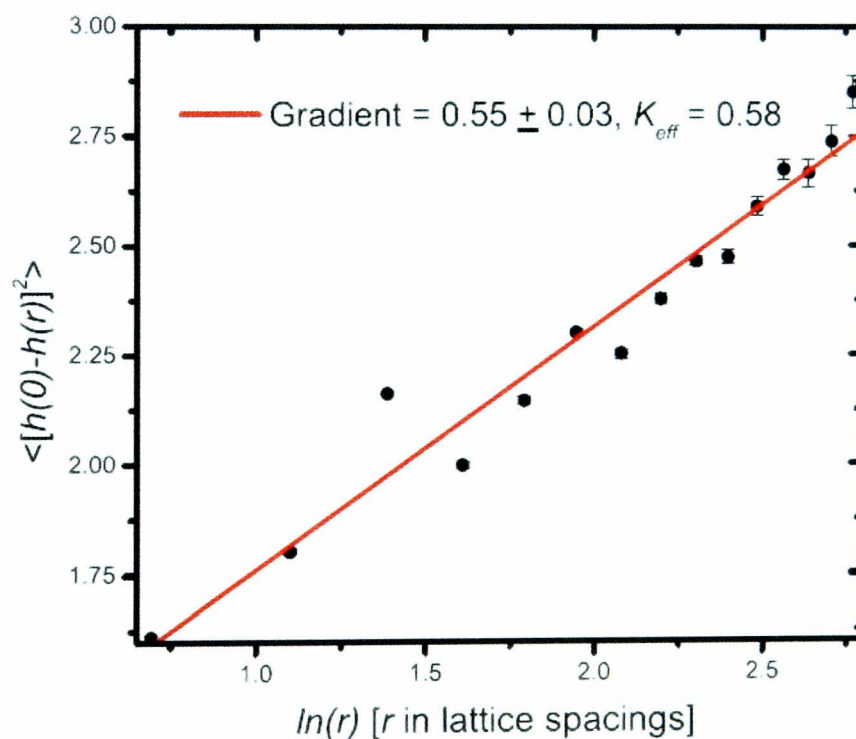


Figure 4.13: Graph showing the logarithmic dependence of the correlation function on distance.

A graph of the correlation function  $C(r)$  against distance is shown in Figure 4.13. There is a clear logarithmic dependence on distance  $r$  identifying the

TPTC network as a random rhombus tiling. The value for  $K$  is determined to be  $K_{eff} = 0.58 = 1.7K_0$

### Discussion of $K_{eff}$ for the TPTC network

The logarithmic dependence illustrates that random morphological behaviour is present in the tiling, though the value for  $K_{eff}$  was determined to be much greater than expected for a maximally random tiling. The correlation function is based on the assumption of a defect free tiling. However, we have already discussed the effect of introducing defects into the tiling in Section 4.4.1. In any case the defects only introduce errors to the correlation function at  $r > r_d$ . Thus this cannot account for the difference between  $K_{eff}$  and  $K_0$ . Close examination of the theory identifies two possible explanations for the discrepancy; an equal number of each of the three tile orientations and energetically degenerate states. The 100x100 nm<sup>2</sup> image used to produce the correlation function contains 4138 tiles with 1376, 1383 and 1379 in each of the three different orientations. This is within statistical error of an even distribution. Which leaves us with the question of whether the tilings are truly degenerate. In Figure 4.9 we identified that the values of  $|\mathbf{d}_1|$  and  $|\mathbf{d}_2|$  were 9.6 Å and 8.7 Å respectively and the binding energy of both systems was determined to be 0.80eV. Whilst there is no energetic difference in terms of the binding energy (within error), the differences in the values of  $|\mathbf{d}_1|$  and  $|\mathbf{d}_2|$  breaks the symmetry of the system and hence also the energetic degeneracy. In our experiments we observe this as a slight preference for the non-parallel bonding geometry. To highlight this preference we note that the ratio of parallel to non-parallel bonds show a clear preference for the non-parallel bonding geometry with 79% ( $\pm 1\%$ ) of the

bonds in the network being non-parallel. By way of comparison, simulations of a maximally random tiling predict 61% ( $\pm 1\%$ ) of bonds to be non-parallel.

#### **4.4.2 Network Defects**

From larger STM scans, we can identify two types of structural defect found in the TPTC network. These defects are fundamentally different from features such as domain boundaries, though they may nucleate at them. The first of which is a simple molecular vacancy, equivalent to a whole rhombus tile that is absent from the network. A vacancy is likely to come about from the readsorption of a TPTC molecule back into solution once the network has been formed. Such an event will result in the breaking of the four carboxylic acid dimer bonds as well as any admolecule-substrate contributions. There will be a large energy barrier (relative to the thermal energy at room temperature) to this process. However, there is still a small but finite probability that such an energetically unfavourable event occurring. The second type of defect is much more intrinsically interesting. It is the equivalent of a half tile vacancy in the network. Such defects arise due to the disordered morphology of the TPTC network, thus are not commonly identifiable in more ordered structures. These defects appear in two different effective “charges” which correspond to triangles in a tiling pointing either up or down. The formation of these triangular defects has not been observed experimentally though we have formulated two likely mechanisms. The first is that they are formed during the initial growth stage of the network and that the TPTC network simply forms around them as illustrated in Figure 4.14a. Secondly that they are formed from a combination of events (Figure 4.14b); the desorption of a molecule from the network creating

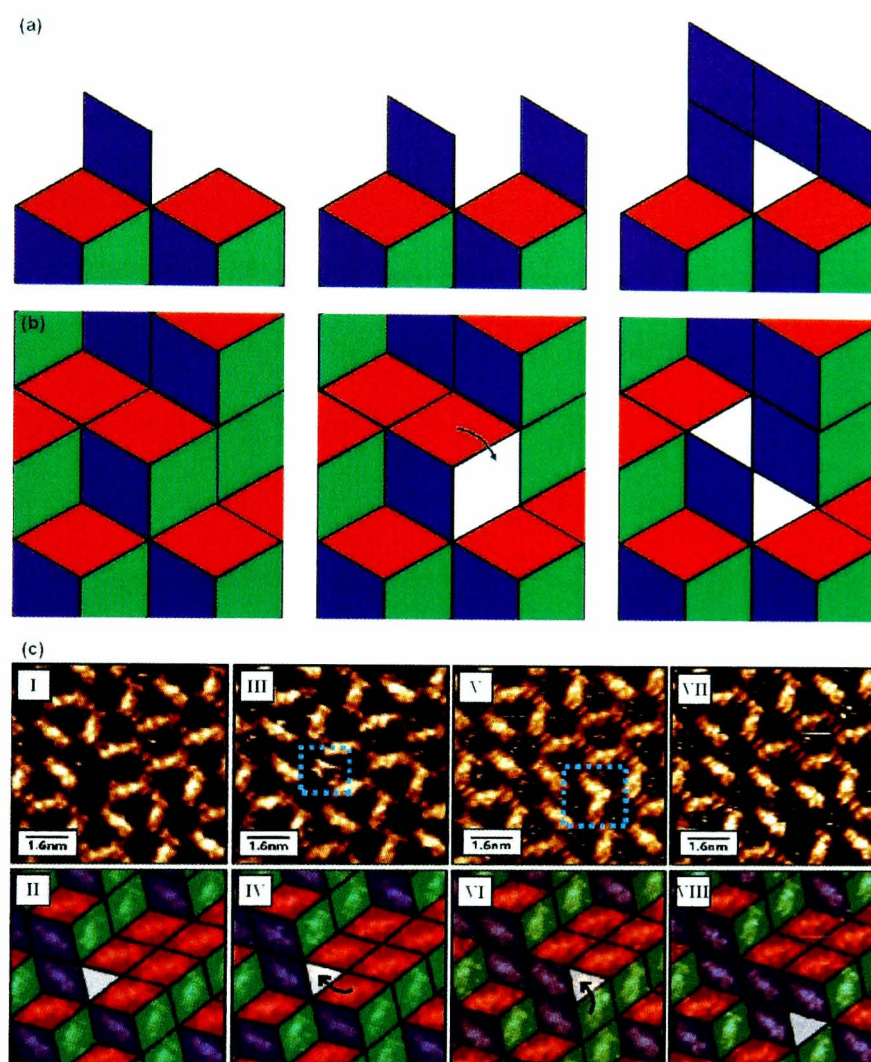


Figure 4.14: **(a)** An example showing the creation of a topological defect during growth. The network grows around the site leaving some carboxylic acid bonds unsatisfied. **(b)** An illustration of defect creation mechanism 2. A TPTC molecule desorbs from the middle of the network and a diffusion event occurs for a TPTC molecule neighbouring the site. The vacancy is then split up into two triangular defects with opposite effective charge. **(c)** An experimentally observed defect diffusion event discussed in the text. The blue box highlights the possible presence of an additional molecular species.

a vacancy, followed by the diffusion of another TPTC molecule adsorbed in the network essentially splitting the vacancy into two independent triangular defects of opposite charge. It is worth noting that the first suggested defect creation mechanism does not require equal numbers of the two defect charges to be created (though statistically it would be expected), whereas the second method does require it.

Whilst the creation of triangular defects has not been observed experimentally, their diffusion through the TPTC network has, as shown in Figure 4.14c[61]. Subfigures I, III, V and VII show the STM scans of the defects diffusion whilst subfigures II, IV, VI and VIII show the corresponding rhombus tilings for the images above them. Subfigure III shows the first diffusion event occurring. Interestingly the STM scan suggests the presence of an interstitial molecule temporally absorbed in the defect. This is even more apparent for the second diffusion event shown in subfigure V. The presence of an additional adsorbed molecule during the diffusion process suggests that, rather than molecules diffusing from one possible site to another, that the adsorption of another molecule into the defect reduces the energy barrier for the desorption of its neighbours. Once the existing molecule has then desorbed, the new TPTC molecule can adopt its most energetically favourable bonding orientation resulting in a net diffusion of the defect site. It is also possible that the appearance of a second molecule is simply an image artifact. It is worth noting that the charge of the defect is conserved through these diffusion events as expected. The net effect of defect diffusion on the network morphology is the reordering of the tiling resulting in a transfer between the degenerate ground states of the system.

The diffusion of defects through the TPTC network raises interesting questions about the post-initial growth evolution of the system. If defects can diffuse, then it is possible that two defects of opposite charge could meet and annihilate by the adsorption of a TPTC molecule. Simulations of the TPTC system[71] suggest that after the initial growth stage of the network, a much longer period of defect annihilation takes place until an equilibrium is obtained where the number of defects annihilating equals the number being created.

### 4.4.3 Evolution of the TPTC network

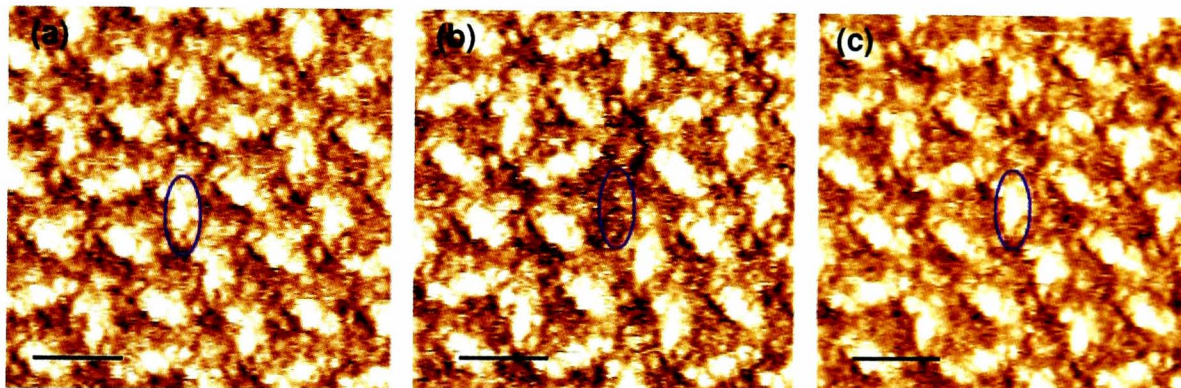


Figure 4.15: A sequence of images showing the creation of a molecular vacancy in the TPTC network. The sequential scans show the desorption of the molecule highlighted with the blue circle. Another TPTC adsorbs into the vacancy in (c). The images were taken at  $I = 150$  pA,  $V_{tip} = 1$  V. Images are were taken approximately 4 minutes apart. The scale bar is 2 nm.

It is clear from our experimental data that once network formation has occurred, the network morphology is essentially trapped in a local energy minimum. We observe little re-ordering of the internal network structure on the timescales of our experiments. In order for the network morphology to change, at least one TPTC molecule will have to first desorb from the surface requiring the breaking of four carboxylic acid dimer bonds in addition to any admolecule-

substrate interactions. In Section 4.1 we calculated the carboxylic acid dimer bond strength as 0.76 eV giving a minimum total bond strength of 3.04 eV, much larger than thermal energy at room temperature making desorption unlikely. However, despite the low probability of this event, we have managed to observe such an event occurring, shown in Figure 4.15. The vacancy is filled by another TPTC molecule before any re-ordering of the network can occur. More frequent network re-structuring will occur from the diffusion of defects (shown in Figure 4.14c). The energy barriers for either desorption or diffusion will be lower for molecules neighbouring such a defect as they will have an unsatisfied carboxylic acid bond.

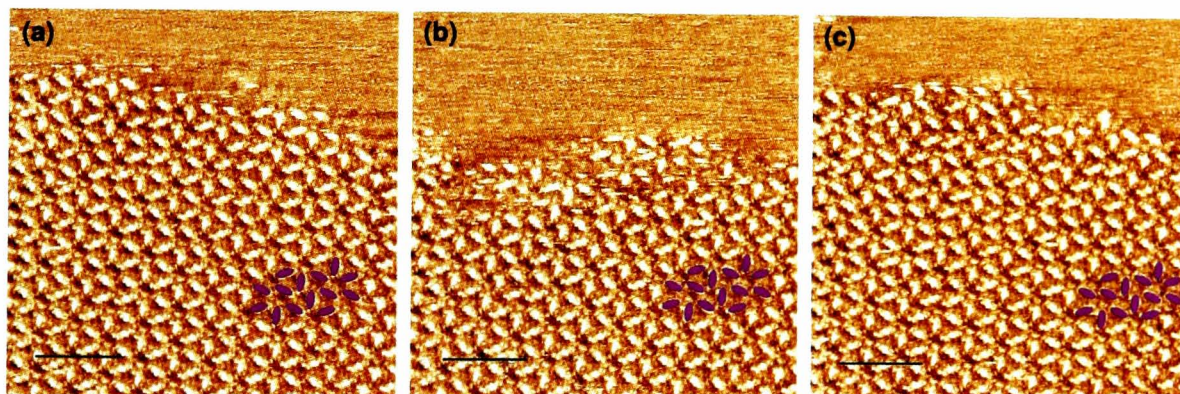


Figure 4.16: A sequence of images showing the evolution of of an edge of the TPTC network. The molecules highlighted in violet provide a reference point. The scans are sequential. Between scans (a) and (b) the edge of the network has withdrawn and between scans (b) and (c) it has grown back. The images were taken at  $I = 150$  pA,  $V_{tip} = 1$  V. Images are were taken approximately 4 minutes apart. The scale bar is 6 nm.

Unlike in the bulk, at network domain boundaries the molecules will have a number of unsatisfied carboxylic acid bonds and as a result be relatively weakly bound to the network making re-ordering events much more likely. Figure 4.16 shows a set of sequential scans of a domain boundary. The sample was imaged with STM immediately after the deposition of the TPTC molecules so that

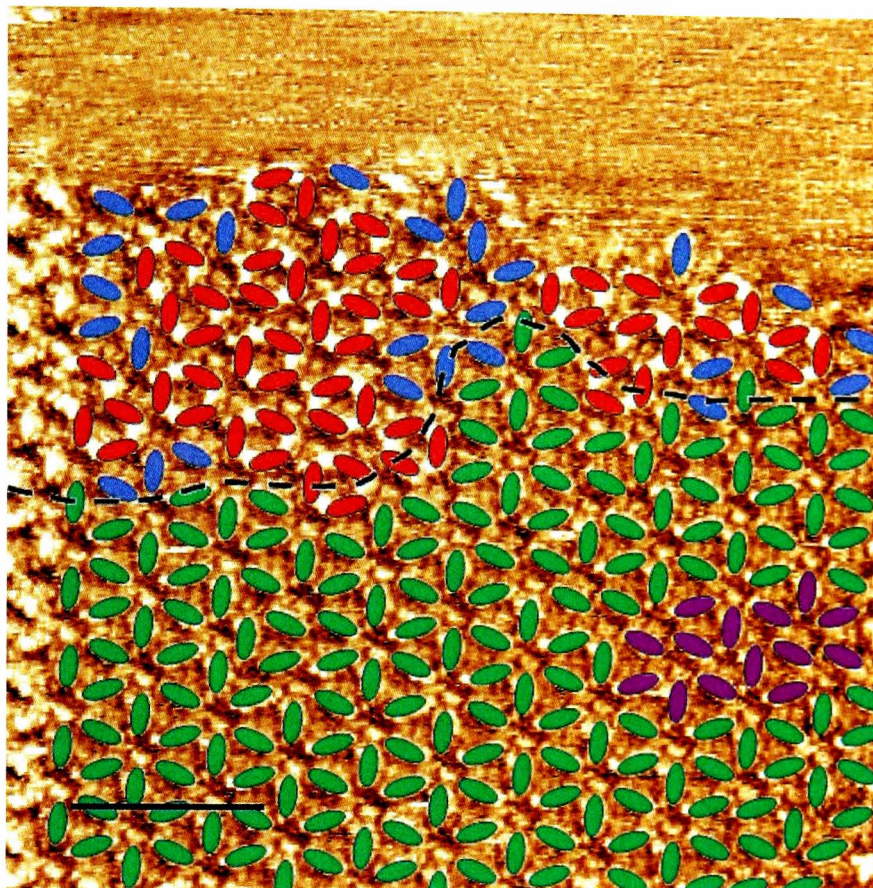


Figure 4.17: A composite image made from the STM image from Figure 4.16c and the positions of all the molecules from Figure 4.16a. The dashed black line represents the approximate edge of the domain from (b). The green ovals represent molecules that are present in both (a) and (c). The red ovals represent the locations of molecules not present in (c) that were present in (a). The blue ovals represent molecules that are present in both (a) and (c) but not in (b). The violet molecules are again for reference. The scale bar is 6 nm.

the growth of the network domains could be studied. Figure 4.16a shows the initial morphology of the network. Between scans 4.16a and b a number of the TPTC molecules have desorbed from the network illustrating the dynamic nature of network formation from solution deposition. The domain has regrown on the surface in scan 4.16c. The molecules highlighted in violet provide a reference point throughout the images. A number of the molecules near the edge of the network appear with line streaks across them or only parts of a molecule are visible. These visual effects are generally attributed to loosely

bound molecules, as expected for molecules at the edge of a network.

Figure 4.17 illustrates the net change in network morphology that has occurred between Figure 4.16a and c. As illustrated by the presence of the red molecules (ovals), the network does not grow back in the same morphology as before. Despite this, some molecules that have been removed from the network grow back in the same position as in 4.16a. This is expected due to the triangular lattice which the molecules form and the random nature of their orientation. We note that despite the statistically low number of molecules in Figure 4.16c, 26 of the 83 (31%) that readsorbed were in occupied positions in (a). Given the triangular symmetry of the underlying lattice we would expect 33% to be in equivalent positions.

## 4.5 Manipulation of the TPTC network

The manipulation of molecules on the nanoscale has been studied by a variety of different approaches. Molecules such as  $C_{60}$  have been manipulated in supramolecular networks under both vacuum[32, 73, 74, 53] and liquid[75] conditions. Other single molecule manipulations have been performed using coronene[76]. Such experiments use the STM tip to perform the manipulation directly. Other approaches utilise chemical changes to the system such as changing the solvent (discussed in Section 2.4) or the introduction of guest species (Chapter 5). In this section we report the manipulation of the TPTC network over extended areas by scanning the surface with a particular range of voltage biases.

The TPTC network is formed via the experimental method outlined in

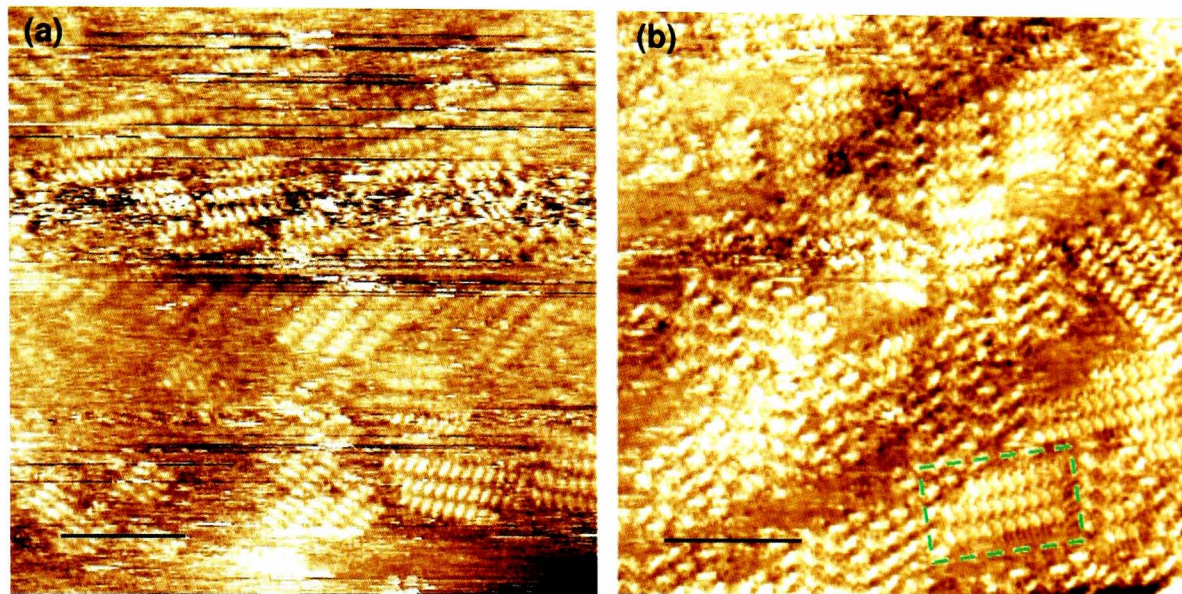


Figure 4.18: **(a)** The manipulation scan performed with  $I = 121$  pA,  $V_{tip} = -1.5$  V. The normal ordering of TPTC is disrupted to form domains of molecules close-packing together. **(b)** The subsequent scan performed with  $I = 121$  pA,  $V_{tip} = 1.1$  V showing that some of the domains relax back into the normal hexagonally ordered network and other remain in a close-packed formation (an example of which is shown in the green dashed box). The scale bar is 6 nm.

Section 4.2. Once the network has formed over extensive areas of the surface, a scan is taken using the normal parameters (typically  $I = 10$ - $100$  pA,  $V_{tip} = 0.8$ - $1.2$  V) to ensure the tip is located over an area of network. Once the scan is complete, the polarity of the voltage bias is reversed (to  $V_{tip} = -1.5$  V) and another scan taken (Figure 4.18a). The image shows the TPTC molecules forming close-packed domains similar to that reported for another carboxylic acid derivative (Naphthylene 2,6-bis(3,5-benzenedicarboxylic acid[63]). There is no evidence that any of the hexagonally ordered TPTC structure remains. The resolution in the image is low and there is a large amount of line streaking suggesting loosely bound material on the surface, consistent with a large scale reordering of the network structure. Figure 4.18b shows the subsequent scan of the network once the imaging parameters had been returned to normal. A

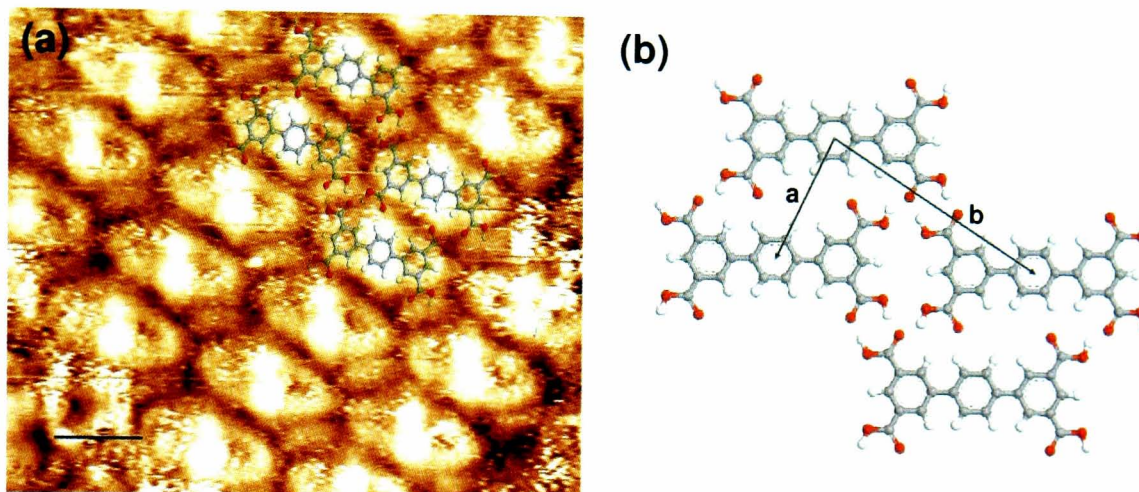


Figure 4.19: **(a)** An image of the close-packed TPTC structure. Sub-molecular resolution of the central benzene group and the carboxylic acid dimer bond is obtained. The image was taken at  $I = 121$  pA,  $V_{tip} = 1.1$  V. The scale bar is 1 nm. **(b)** A model of the TPTC close-packed structure. The model is overlaid on to the image in **(a)**.

clear restructuring of the network has occurred and the presence of domains of close-packed TPTC molecules is notable. An example of the close-packed structure is highlighted in the green dashed box.

A high-resolution image of the TPTC close-packed structure is shown in Figure 4.19a. As in the standard TPTC structure, the central benzene ring appears the brightest of the three and therefore can be used to identify an individual molecule. The molecules form a close-packed structure with each forming two carboxylic dimer bonds, two single O-H $\cdots$ O bonds and two C-H $\cdots$ O bonds. A model of the close-packed structure is shown in Figure 4.19b. Accurate values for **a** and **b** were calculated experimentally from split images, half of the close-packed structure and half of imaging the HOPG substrate. They were determined to be  $0.9\pm 0.1$  nm and  $1.6\pm 0.1$  nm respectively. The value of **a** as determined by DFT[63] is  $0.90\pm 0.01$  nm, in excellent agreement with our value. Setting the carboxylic acid dimer bonds to their most en-

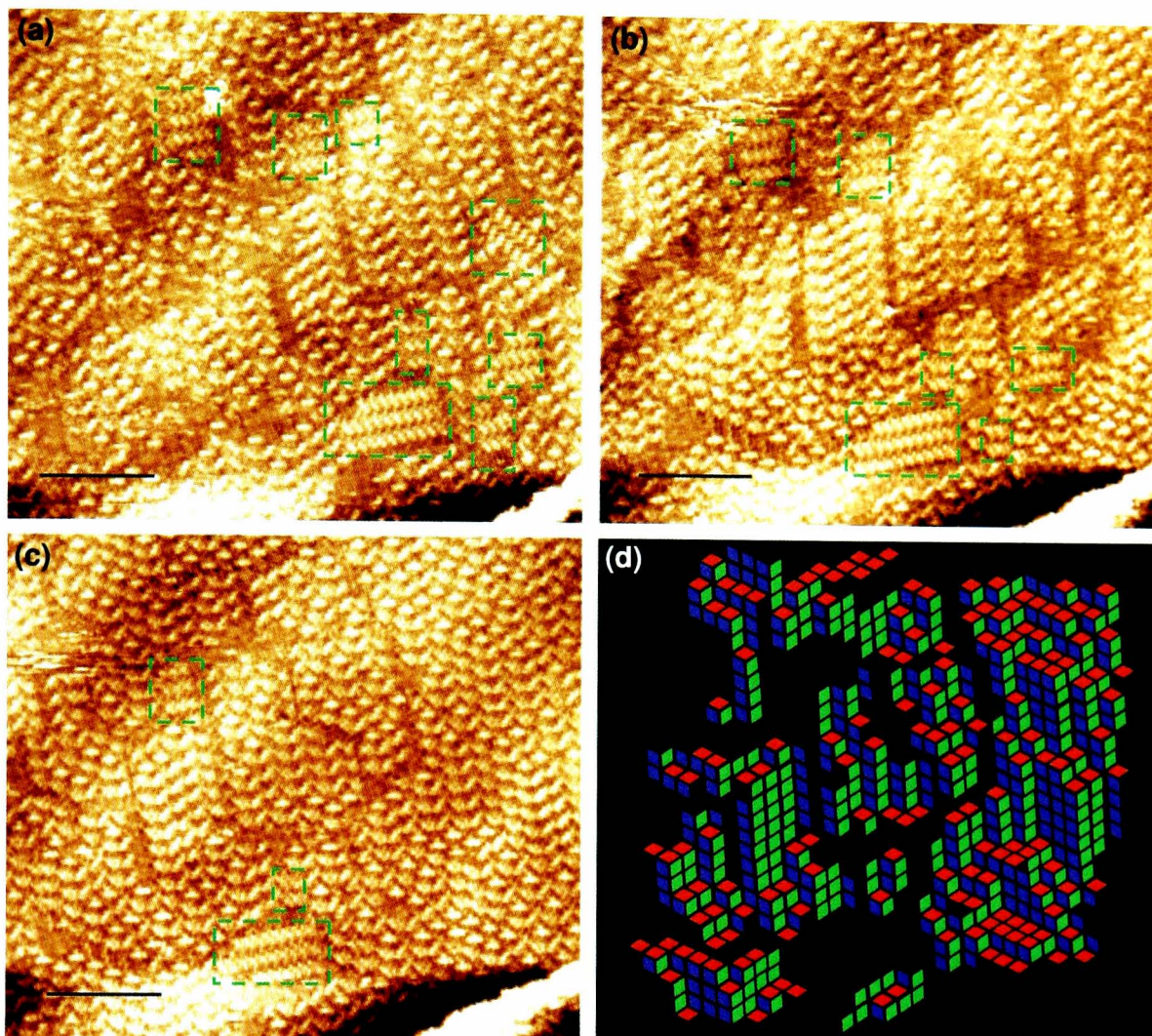


Figure 4.20: **(a)-(c)** The series of sequential scans taken after Figure 4.18b showing the subsequent relaxation of the close-packed TPTC structure. Areas of close-packed structure are highlighted with green dashed boxes. All images were taken at  $I = 121$  pA,  $V_{tip} = 1.1$  V. The scale bar is 10 nm. **(d)** A rhombus tiling of the image shown in (c).

energetically favourable separation gives a value for **b** of  $1.70 \pm 0.1$  nm, also in agreement with our results.

The scans acquired after those shown in Figure 4.18 are shown in Figure 4.20. The scans show a gradual reduction in the areas of close-packed structure (highlighted with the green boxes) over the course of the scans. Each scan took approximately 4 minutes. The relaxation of the network can be characterised by considering the number of molecules in a close-packed arrangement as a

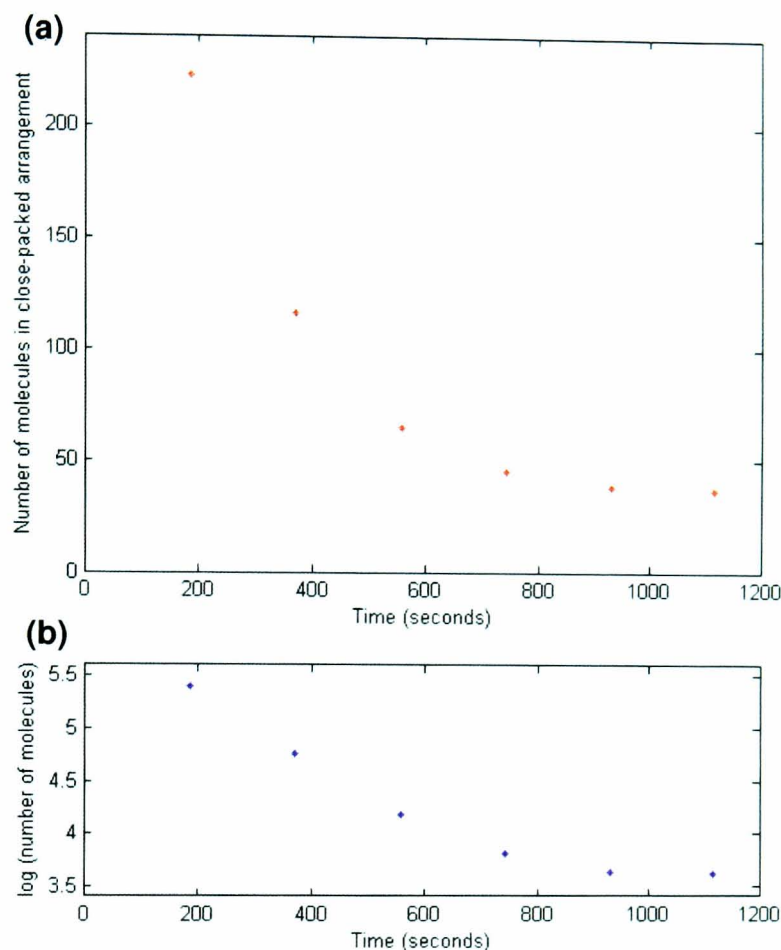


Figure 4.21: **(a)** Graph of the number of molecules in the close-packed arrangement against time since the disruption of the network. The number initially decays exponentially (as illustrated by the logarithmic dependence shown in **(b)**) before slowing.

function of time since the disruptive STM scan was performed (Figure 4.21a). Whilst the decay is at least initially exponential in form (highlighted by the log-plot in Figure 4.21b), after a number of scans the rate of network relaxation slows. We determine the decay constant for the initial relaxation as  $3 \pm 1 \times 10^{-3} \text{s}^{-1}$ . The final area of close-packed structure disappeared approximately 45 minutes after initial disruption.

The morphology of the TPTC network post-relaxation is unlike that seen for the unperturbed system, with large areas containing only diamond pores

Pore Type (%)	Star	Sunrise	Arrowhead	Diamond	Box
TPTC network ( $\pm 1.1\%$ )	13.3	18.4	19.8	1.3	47.3
Disrupted TPTC ( $\pm 4\%$ )	3	19	35	11	32

Table 4.1: Pore statistics for the unperturbed TPTC and post-relaxation disrupted TPTC networks.

Network Type	Ratio of parallel to antiparallel bonds (%)
TPTC network ( $\pm 1\%$ )	21:79
Disrupted TPTC ( $\pm 3\%$ )	38:62

Table 4.2: Pore statistics for the unperturbed TPTC and post-relaxation disrupted TPTC networks.

present. The change in morphology is highlighted visually by producing a rhombus tiling of the final image, shown in Figure 4.20. Whilst the small domain size hinders the identification of patterns in the image, the large numbers of diamond and arrowhead pores are clearly distinguishable. Performing a statistical analysis on the network, we determined the distribution of pore types (shown in Table 4.1). There is a clear preference for the arrowhead and diamond pores at the expense of the star and box types. It is worth noting that the arrowhead and diamond pores have the highest fraction of parallel hydrogen bonds and the star and box pores the lowest. The ratio of parallel to antiparallel bonds is shown in Table 4.2. There is a clear increase in the proportion of parallel bonds observed in the disrupted network. We believe the perturbed statistical distribution we observe results from the relaxation of the close-packed structures, implying that the resulting network is formed from molecular diffusion.

In Section 4.4.3, we demonstrated that the re-ordering of molecules occurs preferentially at edges of domains. We propose that the high initial relaxation rate occurs as the majority of the local area is not covered by bulk network

leading to the exponential decay in Figure 4.21. The rate then falls off as more of the area becomes saturated with the hexagonally ordered TPTC network and the system becomes dynamically arrested in this state. Over time, it is possible that the system may re-order to the same morphology as outlined in Section 4.4 however the timescale for this is likely to be much longer than experimentally feasible to observe.

We have performed subsequent experiments to ascertain the reproducibility. While we have been able to repeatably observe the effect, the range of biases which are required varies from STM tip to STM tip. Network disruption has only been observed for voltages below -1 V, typically in a few tenths of a volt range. Outside of this tip-dependent range either the effect does not occur (for lower absolute voltages) or irreversable changes to the tip occur resulting in the loss of molecular resolution. The effect has only been observed for negative tip voltages, never positive tip voltages and a few STM tips failed to reproduce the effect. Disruption also seems to be relatively localised on the surface affecting areas within approximately 10 to 20 nm of the tip. Whilst we expect the effect to be anisotropic, molecules in the vicinity of domain boundaries appear to be influenced more by the negative bias scanning. Such molecules are of course more weakly bound to the molecular network and hence a lower energy barrier to diffusion.

The manipulation of adsorbates has been studied under vacuum conditions before by many authors[4, 77, 78, 79], however there is little prior literature on such manipulation under solution conditions[75]. The work by Whitman et al.[79] on the manipulation of caesium atoms on two semiconductor surfaces describes how the application of voltage pulses induces diffusion of the

atoms into the region beneath the tip. They argue that the electric field gradient produced by the STM tip induces a potential energy well into which the atoms are able to diffuse. We propose that a similar probe-based manipulation effect is causing the stabilisation of the close-packed TPTC structure in our experiments. There are a number of similarities between our work and that of Whitman et al. which supports this hypothesis. For instance, they report that they do not observe manipulation events under their normal tunnelling conditions arguing that in this case the potential energy gradient must be very small or absent. The strength of the effect also decreases with increasing distance from the STM tip. Although our experimental system is more complex by virtue of being in solution under ambient conditions, we believe a similar mechanism is disrupting the established TPTC network and favouring the formation of the close-packed domains. Despite this we do not have a precise understanding of the mechanism on a molecular level. It could be argued that rather than directly favouring the adsorption of TPTC, the electric field gradient repels solvent molecules from the STM tip leading the energetic preference of the more densely-packed TPTC phase.

## **4.6 Conclusions**

In this chapter we have investigated the adsorption of two similar carboxylic acid derivatives from nonanoic acid on the HOPG surface. QPTC was observed to form an ordered parallel network over extended regions of the surface. A discussion of the periodically modulating contrast of the network is presented and potential sources identified. The second derivative, TPTC, is observed

to form a very different network. Whilst still forming a porous structure, there is no translational symmetry of molecules in the network. We analyse the morphology of this network by utilising height and correlation functions from theoretical discussions of lozenge rhombus tilings. The evolution of this network is then reviewed with particular attention paid to the diffusion of topological defects and domain boundaries. Finally the tip-based manipulation of the TPTC network is presented. The manipulation stabilises the formation of a new close-packed TPTC structure which not otherwise observed.

## Chapter 5

# The formation of multi-component supramolecular structures

*In this chapter we examine the effect of introducing molecular guest species into the supramolecular assemblies described in Chapter 4. We study the introduction of two different guest species, coronene and perylene, into the QPTC parallel network discussed in Section 4.3. Both molecules result in a complete conversion of the parallel network into a hexagonal bimolecular network with the guest species adsorbing into the vertices formed by six QPTC molecules. By drying the sample quickly before the system has been completely converted into this new phase, we are able to observe the growth of this new phase nucleating at the edges of pre-existing parallel domains. In addition, this demonstrates that the adsorbed supramolecular structures are stable on the surface in air.*

*We have also investigated the effect of introducing the coronene guest*

*species into the TPTC network discussed in Section 4.4. By introducing the guest with increasing concentration we are able to gradually fill different TPTC pore types. We observe a slight perturbation to the statistics of the network morphology. In order to examine this effect we perform experiments where both molecular species are deposited simultaneously. Not only do we observe a much increased perturbation of the network statistics but also the formation of localised patches of non-uniform coronene adsorption at low concentrations. We propose that this is caused either by the formation of crystallites in solution or by different growth rates for the two different areas.*

## **5.1 Introduction**

Templating on the nano-scale has been viewed as a route to functionalising surfaces for technological applications[8]. Molecular templates have been used to guide the adsorption of other molecular species in a predefined and controllable way[73, 80, 81, 32]. Understanding the important processes which guide the adsorption of these guest species is a key objective in realising the potential in this field. Recently a number of studies have investigated combining multiple molecular species to form multicomponent molecular systems[25, 82, 83, 63].

In this chapter, we discuss the changes introduced to the two molecular systems presented in Chapter 4 when additional molecular species are codeposited. First, we consider the codeposition of quaterphenyl-3,5,3',5'-tetracarboxylic acid (QPTC) with, separately, coronene (Figure 5.1b) and perylene (Figure 5.1c) molecules. In both cases a hexagonal bicomponent supramolecular structure forms. Second, we investigate the introduction

of coronene into the entropically-stabilised terphenyl-3,5,3',5'-tetracarboxylic acid (TPTC) network.

## 5.2 QPTC bicomponent molecular systems

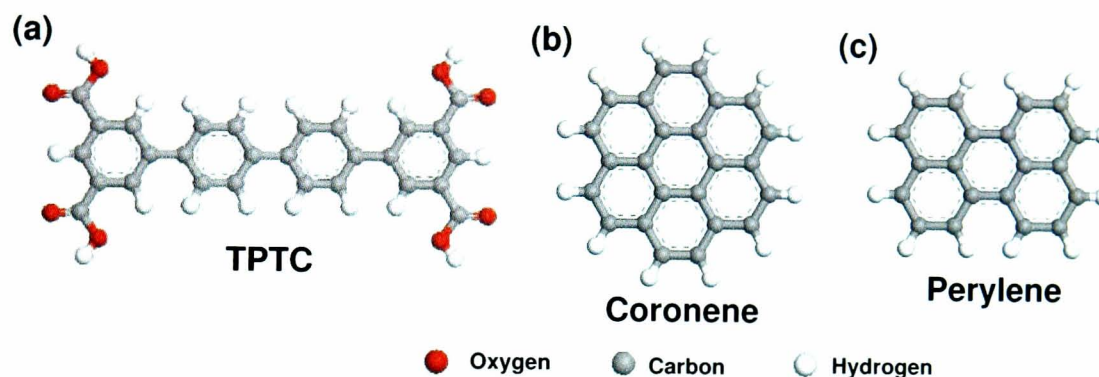


Figure 5.1: Molecular diagrams of the (a) TPTC, (b) coronene and (c) perylene guest species.

In Section 4.4 we discussed the formation of the QPTC supramolecular structure in which molecules align themselves with their organic backbones parallel to each other and bond through four carboxylic acid dimer bonds. We have subsequently investigated combining this network with two guest species; coronene and perylene (shown in Figure 5.1). Both are essentially small flakes of graphene with the edges terminated with hydrogen. The geometries of the two molecules however are subtly different; perylene is rectangular in shape and consists of five fused benzene rings, coronene is approximately circular and comprised of seven. Both molecules were purchased from Sigma-Aldrich. Coronene was purchased at  $\geq 98\%$  purity. Perylene was purchased at sublimed grade ( $\geq 99.5\%$ ) after problems with impurities in preliminary experiments.

### 5.2.1 Simultaneous deposition of QPTC and coronene

QPTC molecules were dissolved in nonanoic acid until a saturated solution was formed. Coronene solutions were prepared by dissolving a known quantity of the powdered solid into a measured volume of nonanoic acid. A 10  $\mu\text{l}$  drop of QPTC in nonanoic acid was deposited on a freshly cleaved HOPG substrate followed immediately by a 10  $\mu\text{l}$  drop of the coronene solution. The STM tip was then immersed directly in the solvent and scanning took place at the nonanoic acid/HOPG interface. Full experimental details can be found in Section 3.6.

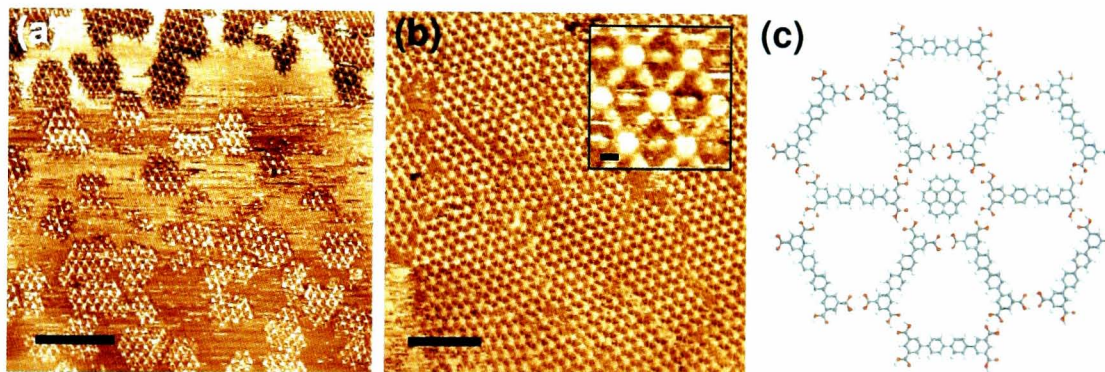


Figure 5.2: (a) An STM image showing the initial growth of the QPTC-coronene bimolecular network. (b) An image showing the network after extensive coverage has formed and the system has entered a state of dynamic equilibrium. A high resolution zoom of the network is shown in the inset. STM imaging parameters are:  $I = 50 \text{ pA}$ ,  $V_{tip} = 1.0 \text{ V}$ . The scale bars are 30 nm and 1 nm for the inset figure. (c) A model showing the QPTC-coronene hexagonal structure.

An example STM image taken  $\sim 20$  minutes after the initial deposition is shown in Figure 5.2a. A relatively large number of small domains consisting of a combined QPTC-coronene network can be seen forming on the HOPG surface. Over time we observe these domains to increase in size until a high surface coverage of  $\geq 90\%$  is obtained. At this stage the supramolecular network enters a steady state where the surface coverage remains approximately

constant. Figure 5.2b shows the network after extended coverage has formed (after one hour). A large number of domain boundaries can be observed in the image owing to the high nucleation rate of domains. The inset shows a zoomed image of the QPTC network. We determine that the coronene molecules sit at the vertices of six QPTC molecules with angles of  $60^\circ$  between them forming a hexagonally order bicomponent supramolecular network. A model of the QPTC-coronene network is shown in Figure 5.2c. We measure the periodicity of the coronene molecules to be  $3.1 \pm 0.2$  nm, in agreement with previous work and DFT simulations[63].

It is interesting to note that we do not observe the formation of any QPTC parallel network, even during the initial growth stage shown in Figure 5.2a. We might expect statistically to observe at least some to form, particularly during the early stages, as the parallel network requires only the presence of QPTC molecules whereas the bimolecular system is formed from two molecular species. This preference for the bimolecular system is further demonstrated by the time each network takes to form on the HOPG substrate. The pure QPTC parallel network takes between one and three hours before the surface coverage enters a steady state. Despite the increased complexity, the bimolecular QPTC-coronene network takes under an hour for the average surface coverage to become constant and can be observed forming within 15 minutes of deposition.

### **5.2.2 QPTC-coronene drying experiments**

We have identified that for the pure QPTC system a parallel structure is observed. However when QPTC is codeposited with coronene molecules a

hexagonally ordered bimolecular structure is preferentially formed. Thus the introduction of coronene appears to change the preferred structure from parallel to hexagonal. In order to explore this further we have performed experiments where the molecules were deposited sequentially; QPTC molecules were deposited first and the QPTC parallel structure allowed to form extensively across the surface, then coronene molecules were subsequently deposited. This would enable us to study the effect on the system of introducing a new, more favourable supramolecular configuration after another structure has preformed.

The first stage of the experiment was to form the QPTC parallel network. A  $10\mu\text{l}$  droplet of QPTC molecules dissolved in nonanoic acid were deposited on a freshly cleaved HOPG substrate. The formation of the QPTC parallel network is then observed with STM until the average surface coverage becomes constant. Then a  $10\mu\text{l}$  droplet of coronene dissolved in nonanoic acid is added to the sample before reimaging with STM. Preliminary experiments showed that the complete conversion from the parallel to the hexagonally ordered bimolecular network typically took under three hours. This places a time constraint on imaging the transition period between the two arrangements. In order to increase this time period samples were dried one and a half hours after coronene deposition. Removing the solvent traps the network morphology in that configuration enabling the sample to be imaged for much longer.

To dry the sample, excess nonanoic acid is first removed using a pipette before the sample is cleaned in a volatile solvent. In order to leave the network intact, we choose a solvent in which nonanoic acid is miscible but the admolecules are insoluble. For this molecular system, hexane was identified as

a suitable solvent. The sample is then dipped in pure hexane for a few seconds before being allowed to dry naturally in a vertical position. The sample is then reimaged with STM, scanning at the air/HOPG interface.

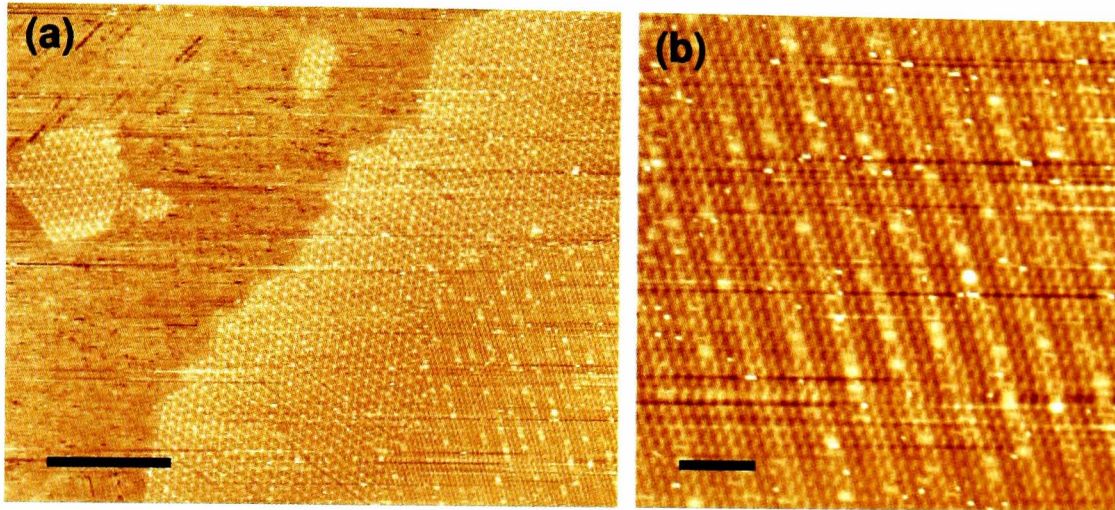


Figure 5.3: (a) An STM image showing a dried QPTC-coronene network formed by sequential deposition. The scale bar is 40 nm. (b) A zoom in of the bottom right corner of (a) showing QPTC parallel network. The periodic contrast modulation has been enhanced. The scale bar is 10 nm. The imaging parameters for both images were:  $I = 20$  pA,  $V_{tip} = 1.1$  V

An example image is shown in Figure 5.3. There are a number of interesting points which arise from the images. First, we have successfully removed the nonanoic acid solvent from the sample whilst retaining a significant proportion of the adsorbed supramolecular network. However, some of the network has been clearly disrupted, though we observe large fluctuations in surface coverage across the sample. Added to this, the network is clearly stable in air. Second, we observed the co-existence of the pure QPTC parallel and QPTC-coronene hexagonal networks. This is expected as the pure QPTC parallel network was pre-formed on the surface prior to coronene deposition. It is interesting to note however, that the bimolecular network appears as a distinct phase at the edge of the parallel network. As discussed in Section 4.4.3, the molecules at the edge

of any network will be the weakest bound and therefore will have the lowest energy barriers to diffusion. These molecules will be the most likely to reorder into a new minimum energy phase. As the molecules reorder to form the QPTC-coronene structure, the domain boundary of the pure QPTC network recedes and molecules that were previously in the bulk of the network become less strongly bound. By removing the solvent we have essentially trapped the system mid-conversion between the two states.

Finally, a number of coronene molecules appear to be adsorbed within the bulk of the QPTC parallel network. Rather than being adsorbed in hexaisophthlate pores, which is observed exclusively when the molecules are codeposited, adsorption has occurred in some of the diamond pores of the QPTC parallel network. However the adsorption does not appear to occur randomly in the QPTC parallel pores but predominately in those situated along the bright regions of the periodic contrast modulation, discussed in Section 4.3. This is illustrated in Figure 5.3b. This implies that the stability of coronene adsorption is enhanced in pores located in the bright regions. One explanation for this is the commensurability of the QPTC network with the underlying HOPG substrate. This could give rise to the pores located within the bright areas having preferential coronene adsorption sites with respect to the substrate (Figure 4.5). The other potential explanation is that all the pores are not exactly the same in the QPTC network. The carboxylic acid dimer bonds, whilst having an optimal separation and orientation, will have some flexibility at an energetic cost. Once the orientation of the molecules with respect to the substrate is considered, it may prove energetically favourable for a slight relaxation of the carboxylic acid dimer bond to occur if an improved

admolecule-substrate interaction is obtainable. This may give rise to slightly different sizes of pore which in turn might mean some of those pores are more energetically favourable for coronene adsorption.

### 5.2.3 Simultaneous deposition of QPTC and perylene

To further our study of introducing additional molecular species into the QPTC network, we have performed experiments using perylene (Figure 5.1b) as a guest species. Two 10  $\mu\text{l}$  drops of QPTC in nonanoic acid were deposited on to the freshly cleaved HOPG substrate followed immediately by a 10  $\mu\text{l}$  drop of the perylene solution. STM images were taken at the nonanoic acid/HOPG interface.

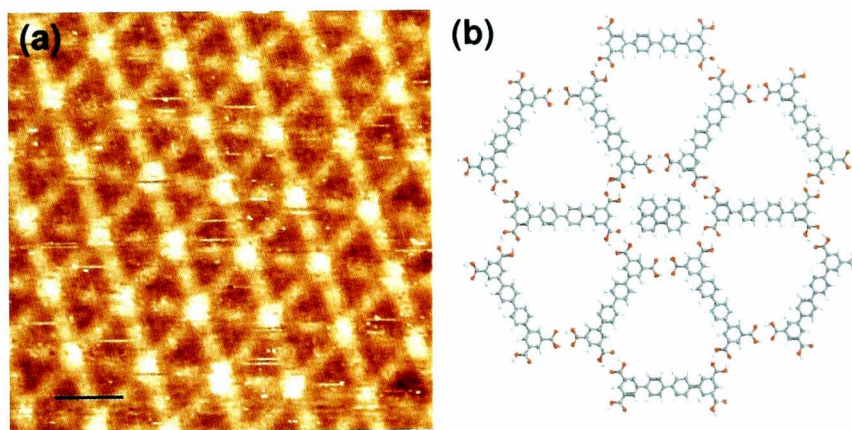


Figure 5.4: **(a)** An STM image of the QPTC-perylene hexagonal network. The scale bar is 3 nm. **(b)** A model of the network. The imaging parameters for the image were:  $I = 100 \text{ pA}$ ,  $V_{tip} = 1.1 \text{ V}$

An example STM image of the QPTC-perylene network is shown in Figure 5.4a. The molecules form the same hexagonal network formed using coronene as a guest species. Taking measurements from multiple images, we determine the separation of the star pores to be  $3.1 \pm 0.2 \text{ nm}$ , in agreement with the value determined for the QPTC-coronene network. The network was

observed to form on a similar timescale to the QPTC-coronene network and also forms with coverage of greater than 90%. A model of the QPTC-perylene network is shown in Figure 5.4b and is equivalent to the QPTC-coronene model except for the different guest species.

### 5.2.4 Guest molecule bonding geometries

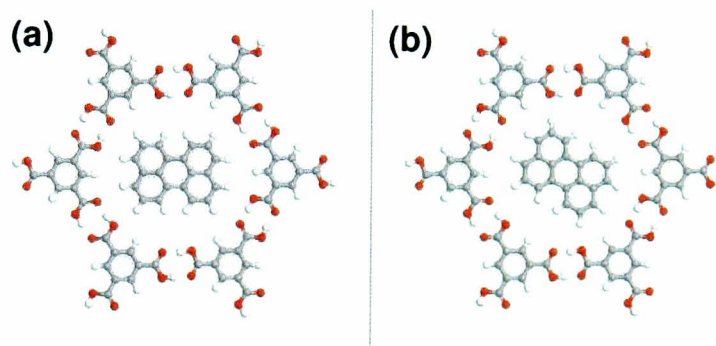


Figure 5.5: DFT simulations of the two discrete bonding geometries of perylene inside the QPTC star pore. TMA molecules are used instead of QPTC as the chemistry of the pore is unchanged but the simulation will be computationally more efficient. The perylene binding energy of both simulations was determined to be  $-0.19$  eV.

Two preferential bonding geometries for coronene molecules in hexaisophthalate pores have been identified [63]. We have performed DFT calculations on the two equivalent bonding geometries for perylene molecules (illustrated in Figure 5.5a and b) to determine which is the most energetically stable arrangement. To simulate this we have determined the energy of a hexagonal arrangement of trimesic acid (TMA) molecules. Such a pore is chemically identical to the star pore formed in the QPTC-perylene network. Two DFT calculations were then performed with perylene adsorbed into the pore in the two different orientations (Figure 5.5). The adsorption energy was then determined from the difference between these calculations and a simulation with

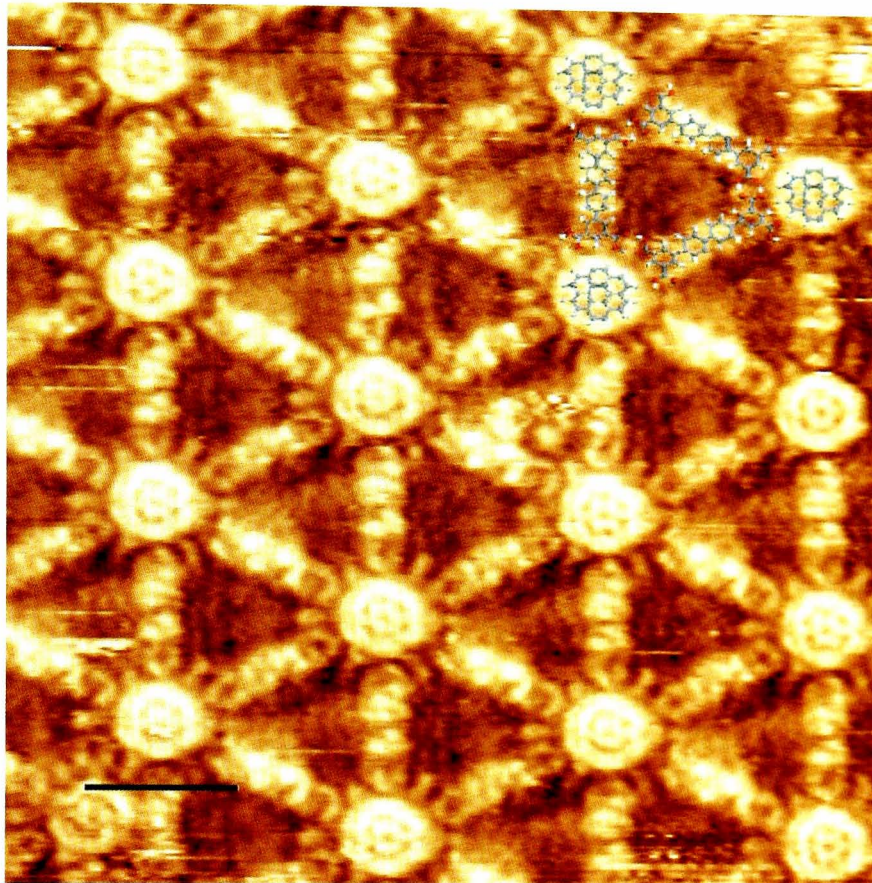


Figure 5.6: A high resolution scan of the QPTC-coronene network showing the orientation of the coronene molecules within the hexaisophthalate pore. A schematic diagram has been overlaid highlighting the orientation of the coronene molecules. The scale bar is 2 nm. The imaging parameters were  $I = 30$  pA,  $V_{tip} = 1.0$  V.

the perylene molecule at infinity. The binding energy was determined to be 0.19 eV for both orientations. By way of comparison, the binding energy for the adsorption of coronene in the equivalent bonding orientations has been shown to be 0.17 eV and 0.20 eV[63] respectively. The source of this binding energy from the simulations will be a number of C-H $\cdots$ O bonds between the guest species and surrounding carboxylic acid dimer junctions. There will also be a significant contribution from interactions with the guest species and the substrate.

It is interesting to note that we have observed the energetic preference shown for coronene experimentally from a sub-molecular resolution image (Fig-

ure 5.6). However no such resolution was obtainable for the QPTC-perylene network. This could be due to the perylene molecules switching between bonding orientations within the pores on a shorter timescale than the experiment, though this would require the energy barrier for switching events to be comparable with thermal energy at room temperature.

## **5.3 TPTC with coronene**

In Section 4.4 we discussed the network formed by the TPTC molecules on the HOPG surface. The network is hexagonally ordered but has no translational symmetry. In Section 4.5, the tip-induced manipulation of the TPTC network and the subsequent relaxation of the structure was demonstrated. The statistics of the relaxed network were heavily perturbed from the original distribution. We have already identified coronene (Figure 5.1b) as a suitable guest molecule for the QPTC network and thus were interested to investigate the introduction of this molecular species into the more complex TPTC network.

### **5.3.1 Sequential Coronene Deposition**

In the first set of experiments, the TPTC network was formed first by the deposition of a 10  $\mu\text{l}$  droplet of TPTC-nonanoic acid solution. The network formation was then observed with STM until a high surface coverage had formed. An additional 10  $\mu\text{l}$  droplet of coronene in nonanoic acid was then added and the sample rescanned with STM. Coronene solutions at different concentrations were prepared by the dilution of a highly concentrated solution to maximise accuracy.

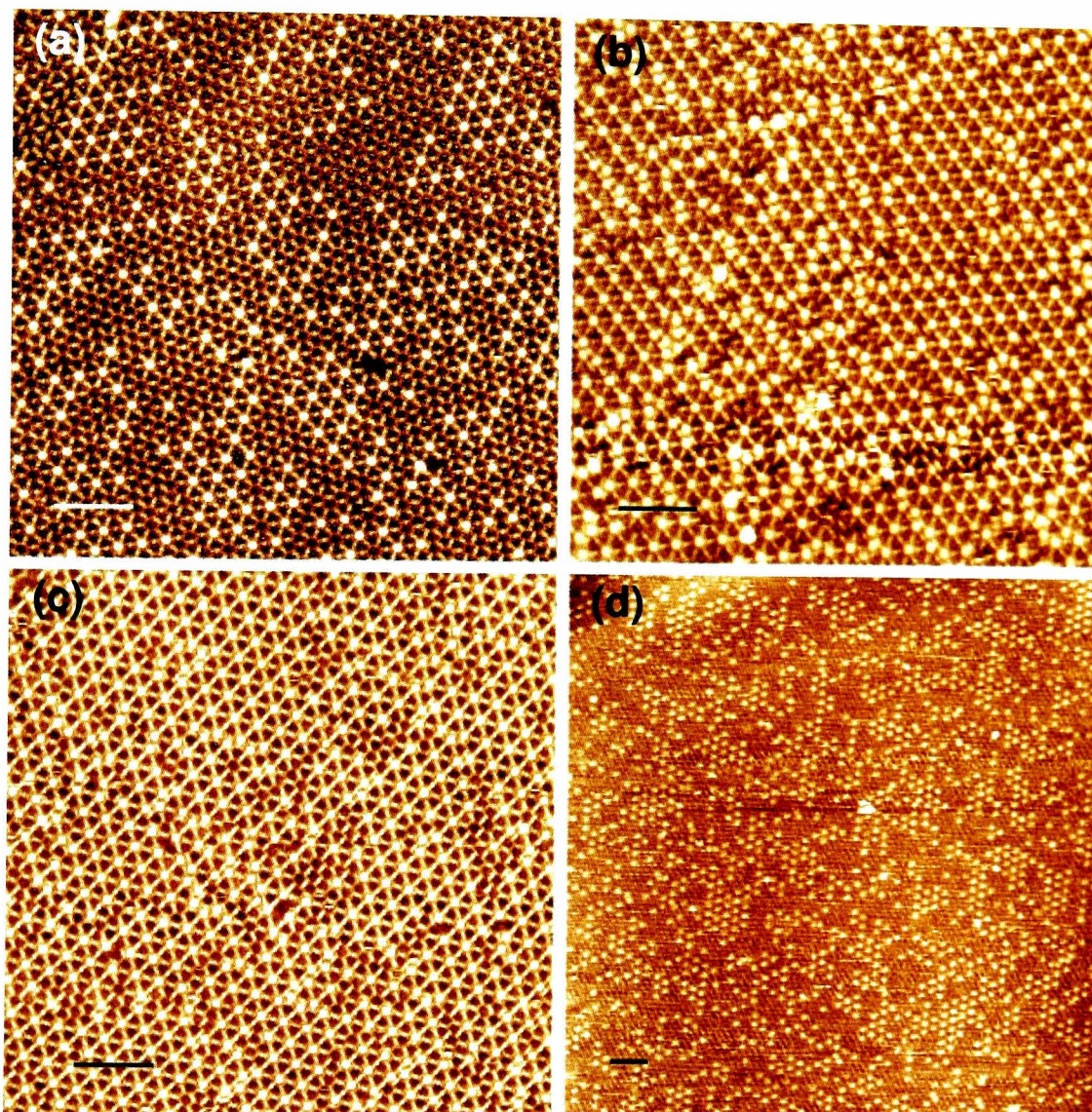


Figure 5.7: A series of scans showing the TPTC-coronene network formed from using coronene solutions with concentrations **(a)**  $1 \times 10^{-4}$  mg/ml (Imaging parameters:  $I = 10$  pA,  $V_{tip} = 1.1$  V), **(b)**  $1.5 \times 10^{-4}$  mg/ml (Imaging parameters:  $I = 15$  pA,  $V_{tip} = 1.5$  V) and **(c)**  $2.0 \times 10^{-4}$  mg/ml. **(d)** A large STM scan illustrating that (a), (b) and (c) are representative images (Imaging parameters:  $I = 10$  pA,  $V_{tip} = 1.0$  V). All scale bars are 10 nm.

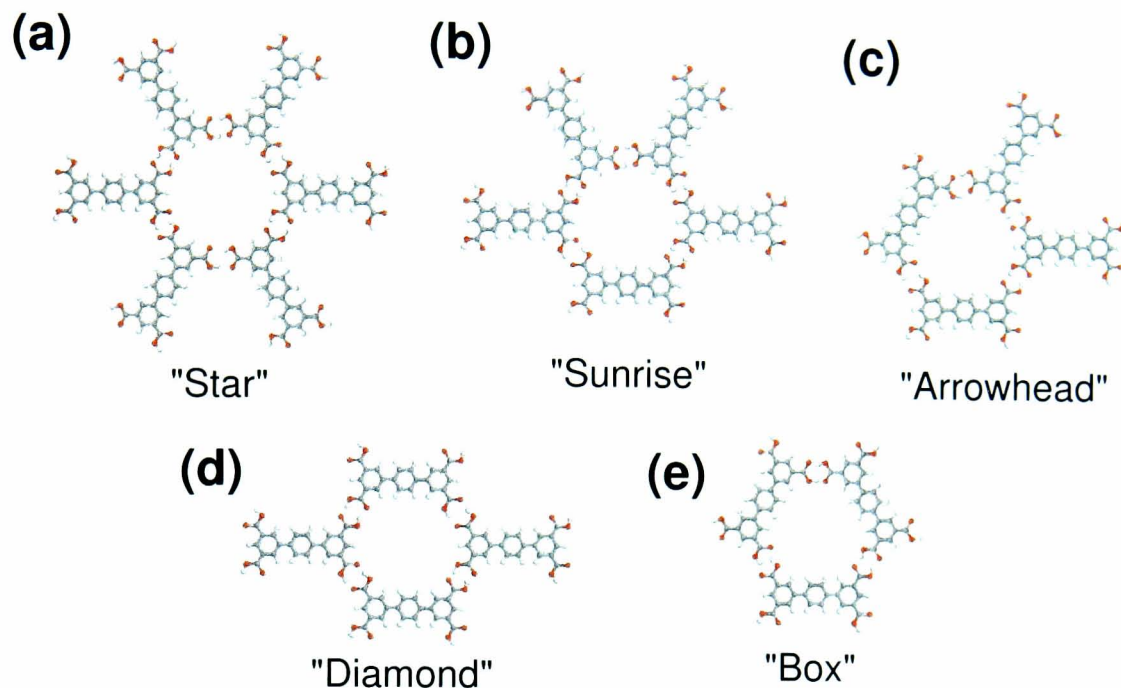


Figure 5.8: Schematic diagrams illustrating the five different arrangements of TPTC molecules around the network pores.

Some example STM images are shown in Figure 5.7. The TPTC molecules appear as rectangular features with the central of the three benzene rings appearing the brightest. The coronene molecules appear as bright circles and appear to adsorb at the vertices of the TPTC network. Figure 5.7a shows the bi-molecular network formed using a coronene solution with concentration  $1 \times 10^{-4}$  mg/ml. Coronene molecules show a clear preference for adsorption into the star pore-type (see Figure 5.8 for pore-type definitions) and to a lesser extent the sunrise pore with  $78 \pm 4\%$  and  $22 \pm 4\%$  of adsorbed coronene molecules occupying those pore types respectively. This suggests that adsorption into the star pore is the most energetically favourable followed by adsorption into the sunrise pore type. In our previous work[84] we have performed molecular dynamics (MD) simulations to determine an estimate for the change in total energy of the different network pores as a result of coronene adsorption.

We determined that the greatest reduction in energy occurred for adsorption into the star pore (-2.45 eV), followed by the sunrise pore (-2.35 eV). Thus if coronene adsorption is guided by energetics alone, we would expect coronene to adsorb into the star pores first. In addition to this we found a reduction of -2.16 eV for the arrowhead pore, -2.08 eV for the diamond pore and -1.86 eV for the box pore type.

Analysis of the pore distribution of the unperturbed TPTC network is given in Section 4.4. Performing the same analysis for pore types in the network at this coronene concentration found little change in the distribution. We also determine that 73% and 16% of the star and sunrise pores respectively contain coronene molecules, suggesting that the surface is not saturated with coronene. The coronene molecules are simply adsorbing into their preferred pore types. We also determine the adsorption rate of coronene into the network by comparing the observed number of coronene molecules per unit area with the number of coronene molecules in solution. In a 10  $\mu\text{l}$  droplet we would expect  $2 \times 10^{12}$  coronene molecules at this concentration. If all these molecules were to adsorb onto the surface the adsorbed coronene density would be  $0.1 \pm 0.02$  molecules per  $\text{nm}^2$ . Analysis of Figure 5.7a shows an adsorbed coronene density of  $0.06 \pm 0.01$  molecules per  $\text{nm}^2$  suggesting that 60% of the coronene molecules deposited adsorb into the network.

Figure 5.7b shows a network formed using a coronene solution of concentration  $1.5 \times 10^{-4}$  mg/ml. Unsurprisingly, increasing the concentration of coronene results in a higher quantity of coronene adsorbing onto the surface. 97% of the star pores in the network are occupied with coronene molecules. Given the dynamic nature of molecular networks formed in solution it is likely

that this pore type is saturated at this concentration. The percentage of sunrise pores containing coronene molecules has also increased to 87%. At this concentration a few of the arrowhead pores now contain coronene molecules (6%) suggesting that this is the third most energetically favourable pore type for coronene adsorption, in agreement with our DFT calculations. Localised line streaking can be seen in the vicinity of some of the arrowhead pores in Figure 5.7b. Such line streaking can be caused by features that are unstable under the scanning of the STM or simply are not stable generally. In either case the appearance of the line streaking suggests the coronene molecules are not as strongly bonded in the arrowhead pores. Performing analysis on the distribution of pore types determined that the network statistics are still within experimental error of those for the pure TPTC network. The observed density of adsorbed coronene is determined to be  $0.137 \pm 0.005$  molecules per  $\text{nm}^2$ . At this concentration, if all the coronene molecules were to adsorb on the surface the density would be  $0.15 \pm 0.03$  molecules per  $\text{nm}^2$ .

Increasing the concentration of coronene further to  $2 \times 10^{-4}$  mg/ml (Figure 5.7c), results in the sunrise pores also becoming saturated (97% of the pores occupied). There is also an increase in the occupation of the arrowhead pores to 18%. We note that at this concentration there was a slight change in the pore statistics of the network. The distribution of pore types was found to show an increase in the star pores to  $17.0 \pm 0.8\%$  and box pores to  $51.8 \pm 0.8\%$  at the expense of the other types. This change is more significant after considering the pore distribution of a pure hexaisophthalate structure, such as that formed by QPTC and coronene, where 33% of the pores are star pores and 67% are box pores. This suggests that the inclusion of coronene into the TPTC

network at this concentration energetically biases the network towards forming a more regular hexagonal structure. Interestingly, when increasing the concentration to this level and even significantly higher we only very rarely observe any adsorption of coronene molecules into either the box or diamond pores, despite our DFT calculations suggesting that such adsorption is energetically favourable. We attribute this to the co-adsorption of nonanoic acid solvent molecules into the “empty” pores of the network. If solvent molecules are co-adsorbed into all the TPTC pores, then the energy change due to coronene adsorption will have to account for this, potentially making coronene adsorption unfavourable. We determine the density of adsorbed coronene for Figure 5.7c to be  $0.124 \pm 0.005$  molecules per  $\text{nm}^2$  ( $0.2 \pm 0.04$  molecules per  $\text{nm}^2$  if all the coronene in solution adsorbed).

Figure 5.7d is a larger scan of the network formed with coronene of concentration  $1 \times 10^{-4}$  mg/ml. Although at this magnification the TPTC molecules are difficult to resolve, the coronene molecules can still be clearly seen. The images shows that the smaller STM scans are representative of larger areas of the surface and that the density of adsorbed coronene molecules across the surface is relatively homogeneous.

### **5.3.2 Simultaneous Guest Deposition**

To further our understanding we have undertaken a second set of experiments to investigate the effect of introducing coronene to the system prior to TPTC network formation. To do this the coronene-nonanoic acid solution (at the required concentration) was mixed with a saturated TPTC-nonanoic acid solution. Following another 15 minutes of ultrasonication to ensure that the

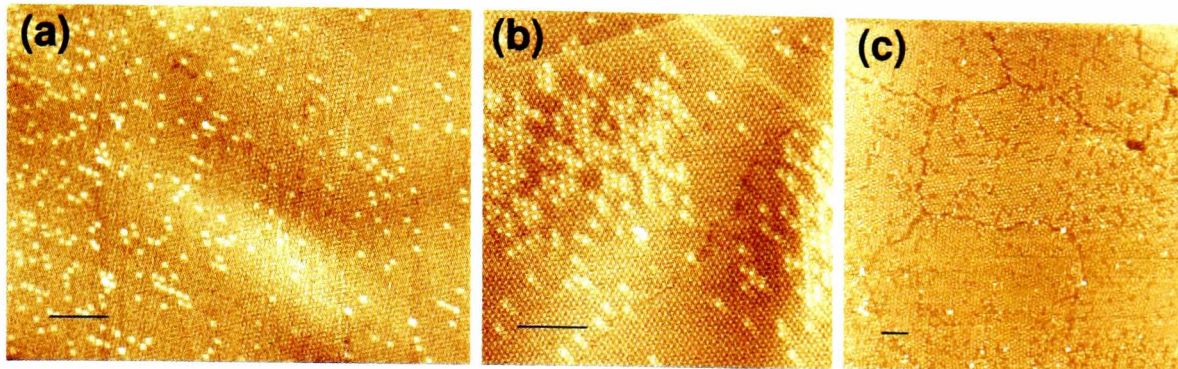


Figure 5.9: STM scans of the TPTC-coronene network formed by depositing the molecules simultaneously. The concentrations of coronene used were **(a)**  $1 \times 10^{-4}$  mg/ml (Imaging parameters:  $I = 80$  pA,  $V_{tip} = 1.1$  V), **(b)**  $1.24 \times 10^{-4}$  mg/ml (Imaging parameters:  $I = 10$  pA,  $V_{tip} = 1.2$  V) and **(c)**  $1.5 \times 10^{-4}$  mg/ml (Imaging parameters:  $I = 10$  pA,  $V_{tip} = 1.0$  V). All scale bars are 20 nm.

concentration of both molecules was even throughout the solution,  $10 \mu\text{l}$  was removed with a pipette and deposited onto a freshly cleaved HOPG surface.

Some example STM scans are shown in Figure 5.9. Note that the scans are of similar size to that in Figure 5.7d. Figure 5.9a shows a network formed from a  $1 \times 10^{-4}$  mg/ml solution of coronene. As in Figure 5.9d the TPTC molecules are difficult to resolve due to the magnification, but the co-adsorbed coronene molecules are clearly visible. The coverage of the TPTC template structure remains as high as when the molecules are deposited sequentially. However the coronene molecules do not adsorb homogeneously into it. This gives rise to areas within the TPTC template with a higher density of adsorbed coronene than others. As in the case of sequential deposition, the majority of coronene molecules adsorb into the hexaisophthalate pores of the TPTC network. Figure 5.9b and c show networks formed from the simultaneous of TPTC and coronene at concentrations  $1.24 \times 10^{-4}$  and  $1.5 \times 10^{-4}$  mg/ml. These images show an increase in the number and size of the areas with a high density of adsorbed coronene as the concentration in solution increases. In

Pore Type (%)	Star	Sunrise	Arrowhead	Diamond	Box
TPTC network ( $\pm 1.1\%$ )	13.3	18.4	19.8	1.3	47.3
TPTC-coronene ( $\pm 2\%$ )	22.2	10.3	11.0	0.3	56.3

Table 5.1: Pore statistics for the unperturbed TPTC and the TPTC-coronene network formed using coronene concentration  $1.5 \times 10^{-4}$  mg/ml and by depositing the molecules simultaneously.

Figure 5.9c it appears that the network is completely saturated with coronene and that no areas with a low density of adsorbed coronene could be found.

It would have been experimentally unfeasible to obtain an STM image large enough to perform a direct comparison of the network morphology between areas with a high and low density of adsorbed coronene. Instead we obtained scans from two different samples: One formed from a solution of coronene with concentration  $1 \times 10^{-4}$  mg/ml; the other from a solution with concentration  $1.5 \times 10^{-4}$  mg/ml. Assuming that the TPTC morphology is only dependent on the inclusion of coronene, it is then possible to compare larger scans of the two areas. Images of two such scans are shown in Figures 5.10a and c. The network with a low density of adsorbed coronene (Figure 5.10a) appears very similar in morphology to that observed for the pure TPTC network. Statistically there are slightly fewer star and more arrowhead pores than expected, though this may be due to under sampling. The image in Figure 5.10c shows an area with a high density of adsorbed coronene. There is a significant increase in the percentage of star pores (to  $22 \pm 2\%$ ) and the box pores (to  $56 \pm 2\%$ ). This occurs at the expense of the other types of pore as shown in Table 5.1.

As in Chapter 4, we utilize height function analysis to illustrate the morphology of the two STM images in Figure 5.10. Details regarding the conversion of an image into a rhombus tiling and the subsequent calculation of its

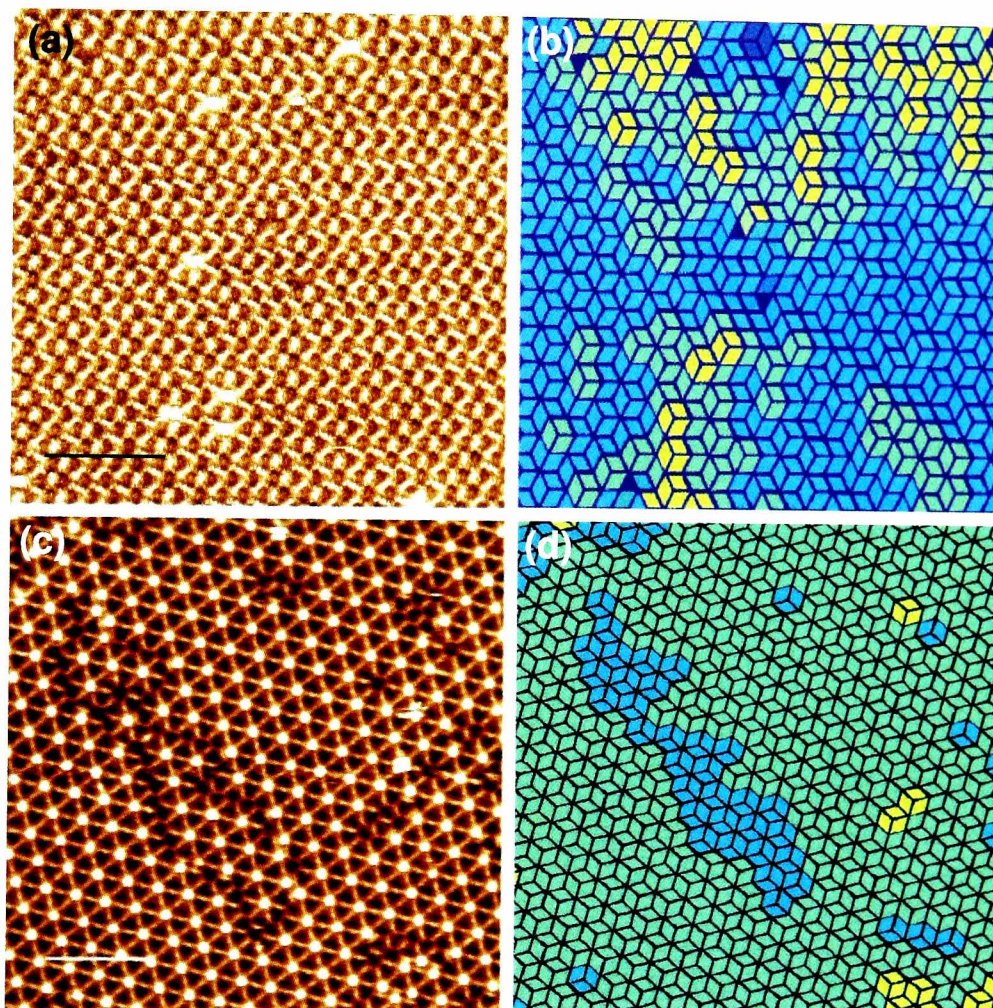


Figure 5.10: **(a)** An STM scan of the  $1.0 \times 10^{-4}$  mg/ml sample prepared by simultaneous deposition. The image was taken in an area with a low density of adsorbed coronene. Imaging parameters:  $I = 50$  pA,  $V_{tip} = 1.0$  V. **(b)** The corresponding height function of (a). **(c)** An STM scan of the  $1.5 \times 10^{-4}$  mg/ml sample prepared by simultaneous deposition. The image was taken in an area with a high density of adsorbed coronene. Imaging parameters:  $I = 30$  pA,  $V_{tip} = 1.0$  V. **(d)** The corresponding height function of (c). All scale bars are 10 nm.

height function can be found in Section 4.4.1. The height functions of Figures 5.10a and c are shown in 5.10b and d respectively. There is a great deal of similarity between Figure 5.10b and the height function associated with a pure TPTC network, as suggested by the similarity in the pore distribution. However, Figure 5.10d is considerably “flatter” than these due to the high percentage of star and box pores. It is clear that a more ordered network has formed. The reasons for this are less clear. We propose two possible explanations for the discrepancy in network morphology in these two areas: (i) crystallites of TPTC and coronene in a hexagonal structure form in solution and upon deposition adsorb onto the surface as a whole; (ii) the presence of coronene causes two different growth phases to occur, one in the presence of coronene, one without. Section 5.2 demonstrated the preferential formation of the QPTC-coronene hexagonal network at the expense of the QPTC parallel structure and on a shorter timescale. We propose a similar effect occurs for the TPTC-coronene system whereby the areas with a high density of adsorbed coronene form initially but because the supply of coronene at low concentrations is constrained, these areas are not able to form extensively across the surface allowing the pure TPTC growth phase to fill in between.

There are clear differences between the networks formed from the two experimental techniques described in this section. At high coronene concentrations there is a significantly lower percentage of star and box pores when both molecules are deposited sequentially. This suggests that the reordering of the network into a similar structure that is formed when molecular deposition is simultaneous is frustrated. We attribute this observation to the kinetic trapping of the network in the initially formed morphology. The small statistical

change in the pore distribution we do observe may be due to increased mobility of the molecules at the edges of TPTC domains and in areas around defects in the TPTC template network facilitating re-ordering.

## 5.4 Summary

In summary, we identify that understanding of supramolecular templates behaviour when guest species are introduced to them is crucial for success in templating the adsorption of a wide variety of molecular species. We demonstrate that guest molecules themselves may sufficiently perturb the energetics of the system such that a restructuring of the ordered network occurs. This in itself produces a different molecular template. For the QPTC template we discuss the desirable goal of removing the solvent from a network and successfully demonstrate that the formed structure is stable in air. We then probe the degree of control we can exert over the unusual network morphology observed for the TPTC molecule on HOPG. We do this by the introduction of the coronene guest species and observe small perturbations in the network statistics when the guest species is deposited after the TPTC network has already been formed. However we note that if the molecules are co-deposited we observe a very different statistical distribution pointing to the system being kinetically trapped in its original morphology when the molecules are deposited sequentially. We also observe a non-uniform adsorption of coronene into the TPTC network (from simultaneous deposition) which we suggest may be caused either by the formation of crystallites in solution or by different growth rates for the two different areas.

## Chapter 6

# Supramolecular networks formed on Au (111)

*In this chapter we present the adsorption and subsequent self-organisation of a variety of molecules on the Au (111) surface. We begin by examining the network formed by hexaazatrinaphthylene molecules, deposited from the solution phase. A previously unreported variation in the adsorbed layer is observed whereby the structure switches between different “domain orientations” frequently across the surface. We then present the adsorption of Tri(4-bromophenyl)benzene from ethanol and butanol solutions. Three distinct close-packed phases are identified, one of which exhibits a similar variation in domain structure to the hexaazatrinaphthylene network. Deposition is carried out initially at room temperature then subsequently at a series of elevated temperatures. The increased temperature results in the formation of a new dimerised phase produced from the covalent coupling of pairs of molecules. Larger trimerised species are observed, though no extended structure forms. Us-*

*ing an extensive covalently-bonded tri(4-bromophenyl)benzene network formed under UHV conditions, we are able to demonstrate the potential of this network as a template by using it to direct the adsorption of adamantanethiol molecules*

## **6.1 Introduction**

The Au (111) surface is widely used in the field of nanoscience because it has an atomically flat terrace structure. Terraces range in size from hundreds down to a few nm across. It is the atomically flat nature of these terraces that has been crucial for studying the deposition and subsequent ordering of molecules under both ambient[85, 86, 33, 87] and ultra-high vacuum (UHV)[88, 73, 16] conditions. In particular, the adsorption of thiol molecules onto the gold surface is highly relevant for biological and pharmaceutical applications as these molecules can be used to anchor species such as DNA strands.

In this chapter we present the adsorption of two molecules with triangular symmetry, 5, 6, 11, 12, 17, 18-hexaazatrinaphthylene (HATNA) and 1, 3, 5 Tri(4-bromophenyl)benzene (TBPB) on the Au (111) surface. The networks formed are compared to those presented in the literature. In the case of TBPB we alter our preparation technique to create TBPB dimers via the surface-mediated aryl–aryl coupling reaction. Finally we demonstrate that the adsorption of adamantanethiol molecules can be controlled using a polymerised TBPB network, produced under vacuum conditions, as a template.

## 6.2 The adsorption of Hexaazatrinaphthylene on Au (111)

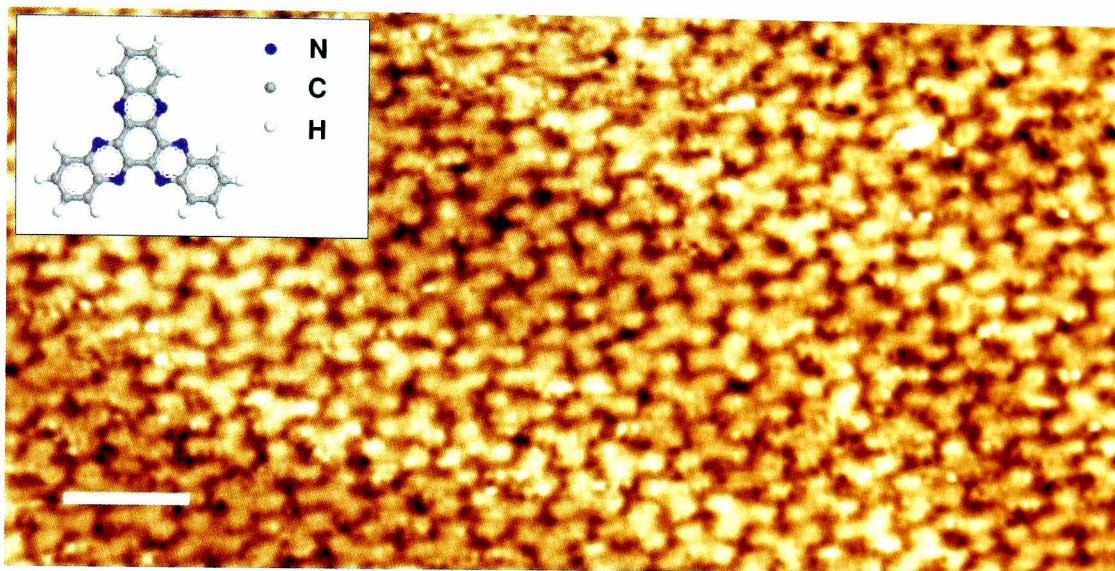


Figure 6.1: An STM image of the HATNA network on Au(111). A ball and stick schematic of the molecule is shown in the inset. Imaging parameters:  $I = 0.3$  nA,  $V_{tip} = 0.5$  V. The scale bar is 1 nm.

HATNA molecules (Figure 6.1 inset) were synthesised as described in the literature[89]. Saturated solutions of the molecule were prepared in ethanol (Sigma-Aldrich) and ultrasonicated immediately prior to deposition. Au (111) samples were purchased from George Albert[49] and prepared as described in Section 3.5.2. The deposition was performed by drop casting a  $10 \mu\text{l}$  drop of the HATNA-ethanol solution onto the Au surface at room temperature and pressure and allowed to dry naturally. The sample was then imaged with STM.

An example STM image is shown in Figure 6.1. Note that in addition to plane subtraction, flattening and a histogram equalisation, the image has been Gaussian smoothed in order to reduce image noise. The molecules orient themselves in one of four different orientations. Molecules then predominantly

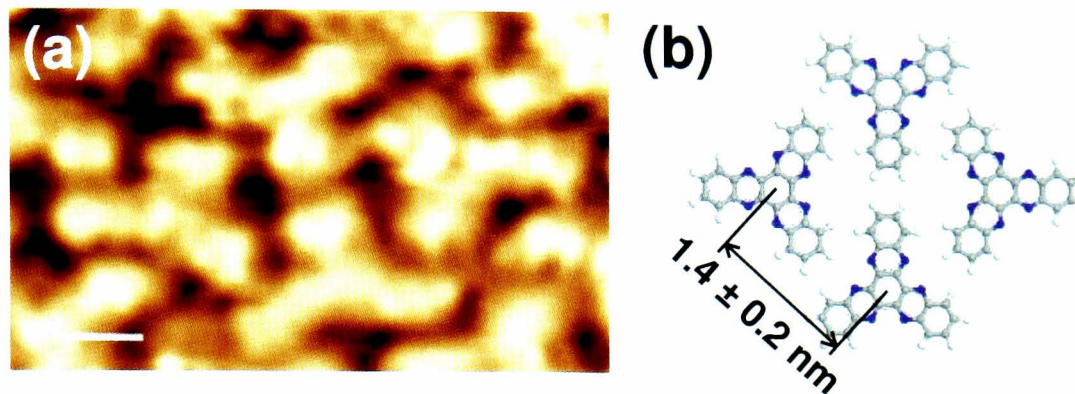


Figure 6.2: **(a)** A zoom showing the bonding geometry of the HATNA molecules. Imaging parameters:  $I = 0.3 \text{ nA}$ ,  $V_{tip} = 0.5 \text{ V}$ . The scale bar is  $2 \text{ \AA}$ . **(b)** The corresponding output of the DFT simulation of the junction.

form groups of four (one molecule in each orientation) in the arrangement shown in Figure 6.2a. The Au (111) herringbone reconstruction can be seen faintly through the HATNA network. The nearest neighbour distance is measured to be  $1.4 \pm 0.2 \text{ nm}$ . Drift in the STM image was taken account for by stretching the image until the three fold rotational symmetry of the molecule was correctly represented.

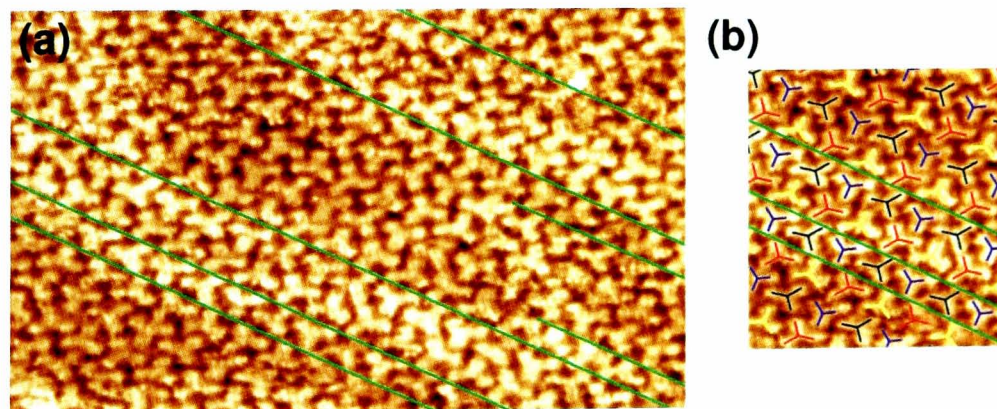


Figure 6.3: **(a)** Figure 6.1 with green lines illustrating the defect lines in the network. **(b)** A zoom of (a) with the molecules coloured by orientation to highlight the changes in morphology. STM imaging parameters:  $I = 0.3 \text{ nA}$ ,  $V_{tip} = 0.5 \text{ V}$ .

To test the stability of the junction shown in Figure 6.2a we perform DFT simulations on the group of four molecules. We determine that the configura-

tion is stable and the junction has a binding energy of 84 meV per molecule. Note that each molecule is involved in a total of two hydrogen bonding junctions giving a hydrogen bonding stabilisation of 168 meV per molecule. The model (Figure 6.2b) is predominately stabilised by four hydrogen bonding junctions between a C-H group and two nitrogen atoms. Our simulations did not include the effect of the substrate or solvent or any van der Waals bonding between C-H groups. We determine from these simulations a nearest neighbour separation of 1.23 nm, in agreement with our experimental determined value.

Closer examination of Figure 6.1 reveals that whilst the molecules form an extended network on the surface, the final network morphology is more complex than the simple four-membered group shown in Figure 6.2b. Rows of different molecular bonding junctions, parallel to one of the nearest neighbour vectors, run through the network. Either side of these “defect lines” (highlighted in green in Figure 6.3) the molecular bonding geometry in Figure 6.2b occurs, but across them there is a shift of half a unit cell in the structure. This behaviour has not been observed previously for HATNA molecules on Au (111)[90]. The majority of the lines run through the whole adsorbed network, though we observe the nucleation of some.

We analyse the ordering of the network by considering the orientation of individual HATNA molecules, as shown in Figure 6.3b. Considering rows of molecules parallel to the green line defects in Figure 6.3a, we are able to identify that only two of the four orientations are present in each row. The molecular orientations alternate between the two along these rows. For example molecules in the row above the top most green line in Figure 6.3b alternate between the red and yellow orientations. The row above that alternatives be-

tween the blue and black orientations and the next row back to red and yellow. In the structure characterised by the bonding geometry in Figure 6.2 there is also a relationship between the molecular orientations in neighbouring rows. Again taking top region of Figure 6.3b as an example, red molecules are next to blue ones in the next row, then back to red. Likewise, yellow molecules are next to those in the black orientation. However, across the line defect the rows are displaced by one molecular adsorption site (half a unit cell), thus red becomes next to black and blue to yellow. This give rise to a different bonding geometry at the line defect. We also note for the case where we observe line defects to nucleate in the middle of the HATNA network the cause is the adsorption of two molecules in the same orientation immediately next to one another. Typically line defects are separated by on average five molecular adsorption sites.

As noted before this behaviour has not been reported in previous work where the molecule was deposited using UHV techniques where the sample was annealed before imaging. We therefore postulate that this behaviour arises due to boundaries of domains with different substrate registries meeting commensurately. In UHV experiments these small domains reorder under annealing.

### **6.3 The adsorption and dimerisation of Tri(4-bromophenyl)benzene molecules on Au (111)**

Covalent coupling of molecules on metallic surfaces provides a new route to the formation of large molecules and extended nanostructures[91, 92, 93, 18, 94, 95, 96, 97, 98, 99]. There are several approaches to inducing such coupling based commonly on either the Ullmann coupling reaction[100], in which a carbon-halogen bond of an adsorbed molecule is cleaved, or a condensation reaction between amine and carbonyl groups[94, 95, 96]. Covalent coupling of molecules has recently been used to form graphene[101] strips and nanostructured templates[102] and there is great potential to form a wide range of functional polymeric systems using this approach. However, the work reported to date has been performed under ultra-high vacuum conditions, often in conjunction with single crystal metallic surfaces and it is highly desirable to develop an analogous, but methodologically simpler, technique compatible with solution deposition and surfaces which are stable under ambient conditions.

In this section we show that aryl–aryl coupling can be promoted on a metallic surface under ambient/liquid conditions. In particular we show that the molecule tri(bromophenyl)benzene (TBPB shown in Figure 6.4), a molecule which has previously been demonstrated to form covalent networks under vacuum conditions[102, 103, 104], can be dimerised to form 3,3.5.5-tetra(4-bromophenyl)-quarterphenyl (TBPQ) through aryl–aryl coupling on a gold

surface by the drop deposition of an ethanolic or butanolic solution of the parent compound. The conversion of TBPB monomers to TBPQ is confirmed using scanning tunnelling microscopy (STM) and time-of-flight secondary ion mass spectrometry (ToF-SIMS).

### **6.3.1 Room Temperature Experiments**

Au (111) on mica samples were purchased from Georg Albert[49]. Samples were used as new, but were cleaned prior to molecular deposition in an oxygen plasma as described in Section 3.5.2. TBPB was purchased from Sigma Aldrich at 97% purity. Saturated solutions of TBPB in two solvents; ethanol and butanol were prepared. Deposition was carried out at room temperature. A 10  $\mu$ l droplet of solution was removed using a pipette, deposited onto the sample and allowed to dry for one minute before being removed from the hot-plate. Images of the sample were acquired with STM under atmospheric conditions.

STM images of the surface following droplet deposition at room temperature are shown in Figure 6.4. It is possible to identify TBPB molecules, which are resolved as trigonal features in the images. Three different packing arrangements are observed for the TBPB monomers, as shown in Figure 6.4. Phase I (Fig. 6.4a)) is essentially equivalent to that observed for sublimed monolayers in vacuum[102, 103, 104], but Phase II (Fig. 6.4e)) and Phase III (Fig. 6.4g) have not been reported previously. Simple schematic models of these molecular phases are shown in Figs. 6.4 c, f and h, on which the unit cells are overlaid. For Phase I we determine the values of  $|\mathbf{a}|$  and  $|\mathbf{b}|$  to be  $16.8 \pm 0.4$  Å and  $24.1 \pm 0.5$  Å respectively, with an angle between them of  $58 \pm 2^\circ$ . For Phase

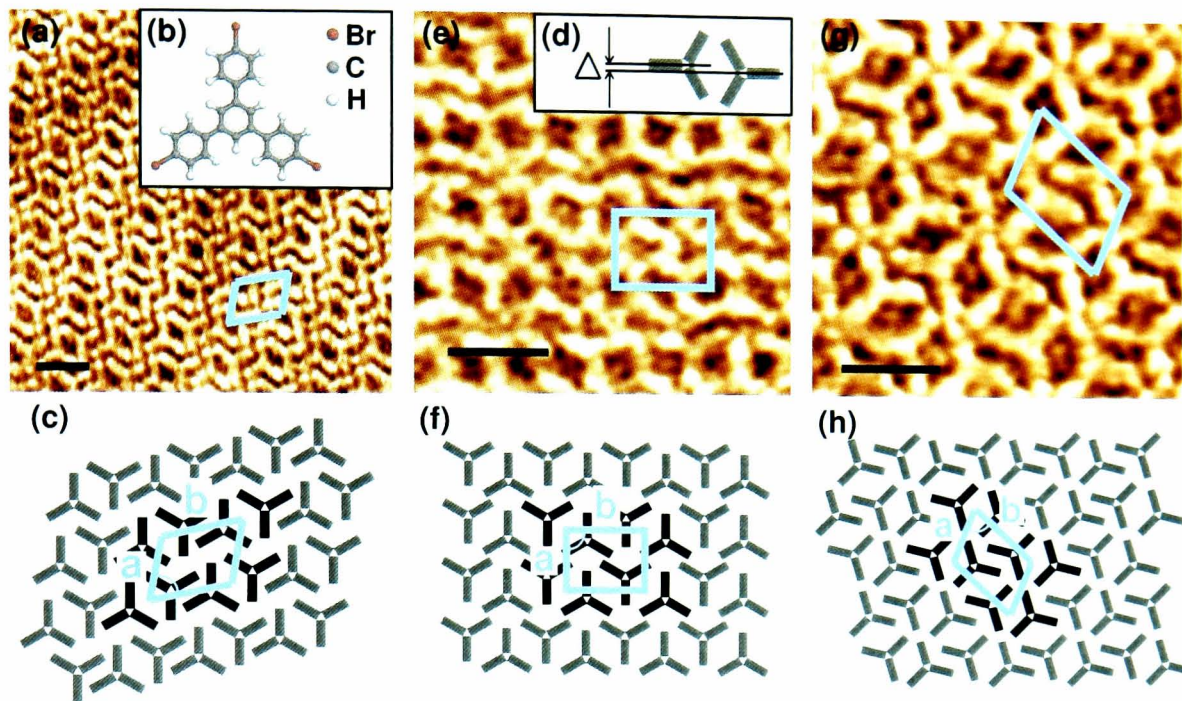


Figure 6.4: STM images of (b) TBPB adsorbed on the Au (111) surface at room temperature. The molecules have been observed to form three distinct phases; (a) Phase I, (e) II and (g) III. Diagrams highlighting the molecular packing of the three phases are shown in (c), (f) and (h) respectively. Molecules were deposited from solutions of ethanol ((a) and (e)) and butanol (g). Illustrated in (d) is a schematic diagram of the molecular pair which forms the basis of the regular arrangement for all three phases. The small offset of the two molecules is described by the parameter  $\Delta$ . Imaging parameters: (a)  $I = 0.4$  nA,  $V_{tip} = 0.6$  V; (e)  $I = 0.5$  nA,  $V_{tip} = 0.4$  V; (g)  $I = 0.5$  nA,  $V_{tip} = 0.4$  V. All scale bars are 2 nm. Unit cells are drawn for each phase.

II the values are determined to be  $16.7 \pm 0.4$  Å and  $19 \pm 1$  Å with an angular separation of  $90 \pm 5^\circ$ , while for Phase III the values are determined to be  $17.6 \pm 0.2$  Å and  $22.1 \pm 0.9$  Å with an angular separation of  $70 \pm 7^\circ$ . In each case we identify a two molecule basis (for all schematics the basis is centred on the vertices of the unit cells). The two molecules forming the basis are rotated by  $180^\circ$  with respect to each other and are slightly offset as illustrated in Fig 6.4d. We measure this offset,  $\Delta$ , to be  $2 \pm 1$  Å. We attribute this offset to the stabilization of this intermolecular junction by halogen bonding[105] as recently demonstrated for TBPB[104].

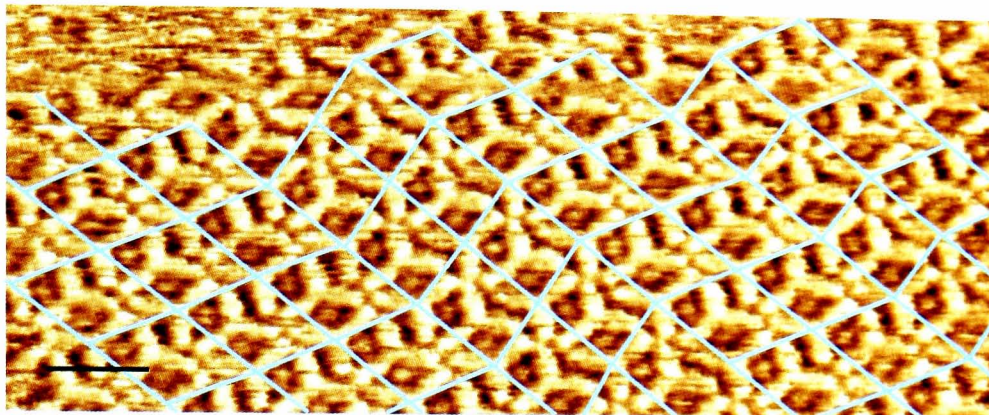


Figure 6.5: An image of an extended area of phase 1 of the TBPB network. The blue lines indicate the unit cell vectors. As can be seen from the image there are a series of mirror reflections of the vectors across the domain. The scale bar is 2 nm. Imaging parameters:  $I = 0.5$  nA;  $V_{tip} = 0.4$  V.

The unit cell we present for phase III formed by close-packed TBPB monomers, whilst being accurate, gives an incomplete picture of the extended network morphology we observe. The unit cell appears to randomly and commensurately change between two sets of angular parameters across the network in a similar fashion to the HATNA molecules discussed in Section 6.2. An example image is shown in Figure 6.5. The unit cells are shown in blue to illustrate the effect. The switching of the unit cell parameters appears to be non-periodic for our data (on 10-20 nm scale) and we only observe the switching to occur in one dimension. The two unit cells seem to be equivalent, related by a simple mirror transformation and thus the network can commensurately switch between the two cell orientations. This also suggests that the admolecule-admolecule bonding geometries are identical. Interestingly, such unit cell switching is not observed in the UHV experiments. It is likely that this effect is removed by the repeated annealing of the sample.

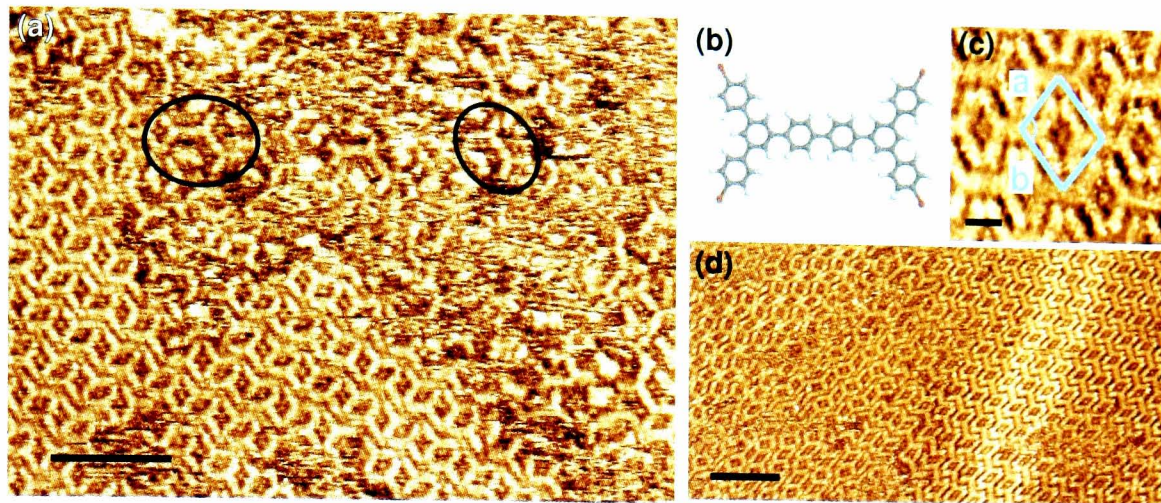


Figure 6.6: Aryl–aryl coupling of TPBP by drop deposition on heated substrates. **(a)** An image showing the TPBP network formed when the substrate was heated to 150°C prior to deposition from ethanol. The black circles illustrate a few examples of covalently bonded molecules. Imaging parameters:  $I = 0.2$  nA;  $V_{tip} = 0.3$  V. The scale bar is 5 nm. **(b)** A schematic diagram of the TPBP dimer. **(d)** An image showing the network formed at 200°C from ethanol. On the right hand side a new phase can be seen due to the formation of TPBP dimers. Imaging parameters:  $I = 0.5$  nA;  $V_{tip} = 0.5$  V. The scale bar is 5 nm. A zoom of the TPBP dimer phase is shown in **(c)**. The unit cell is drawn highlighting the molecular packing. The scale bar is 1 nm.

### 6.3.2 Elevated Temperature Experiments

To promote covalent bonding of TPBP molecules, the solution was deposited onto Au substrates which had been heated for five minutes in atmosphere. The substrate was heated at the desired temperature until evaporation was completed. Solutions were ultrasonicated immediately prior to deposition but not heated. Figure 6.6 shows examples of the resulting surfaces. Figure 6.6a shows that heating the substrate to 150°C leads to the appearance of a number of apparent bonding events at domain boundaries involving isolated groups of molecules (circled; monomer Phase II is also present in this image). These features are consistent with the formation of a covalent bond through aryl–aryl coupling arising from cleavage of C-Br bonds on neighbouring molecules

followed by the formation of a C-C bond which results in a quarterphenyl backbone to which four bromophenyl groups are attached. The molecular structure of the dimerised TBPB, TBPQ, is shown in Figure 6.6b. The length of the quarterphenyl backbone is determined to be  $13.1 \pm 1 \text{ \AA}$ , consistent with DFT simulations of TBPQ[102]. It is also possible for the TBPQ molecules to undergo further Ullman coupling reactions to form multiply connected species which are the precursors of extended polymers and we observe several examples where three TBPB molecules have combined to form a trimer.

Heating the Au sample to  $200^\circ\text{C}$  during deposition resulted in the emergence of an ordered phase of TBPQ as shown on the right of Figure 6.6d (on the left of this image are regions of monomer phase II and III). In this case we find that not only has the TBPB dimerised, but it has also been organized into extended regular structures. It is clear that the appearance of TBPQ in Figure 6.6d is very similar to those identified in Figure 6.6a and, furthermore, the length of the quarterphenyl backbone is identical in both cases, within experimental error. The values for  $|\mathbf{a}|$  and  $|\mathbf{b}|$  in the unit cell for the bonded phase are determined to be  $16 \pm 1 \text{ \AA}$  and  $17 \pm 1 \text{ \AA}$  respectively with an angle of  $93 \pm 14^\circ$  between them .

While our STM results show very clearly that the adsorbed molecules have undergone some changes as a consequence of annealing, it is difficult to identify the product unambiguously from STM images alone. In fact this is further complicated by the existence of other possible reaction products such as the partial loss of one or more of the remaining Br atoms attached to the dimer caused by further interaction with the surface. In addition there have been alternative bonding configurations involving Au atoms providing a connect-

ing link between halogen atoms. This type of metal co-ordination has been reported previously in vacuum studies of TBPB[104] and other halogenated molecules[106].

To distinguish between the formation of TBPQ and other possible products we have investigated the films formed at different temperatures using ToF-SIMS. This analytical technique provides a direct measurement of the mass spectra of surface-adsorbed species as discussed in Chapter 3. Figure 6.7 shows extracts from the full spectra over the relevant mass ranges for Au atoms, TBPB and TBPQ. The top row shows the spectra acquired for a control sample which was heated to 200°C before the deposition of a 10  $\mu$ l droplet of pure ethanol. In this case we observe the expected peak for Au+ ( $m/z = 196.96$ ) but no evidence of species with masses close to that of TBPB ( $C_{24}H_{15}Br_3+$ ,  $m/z=541.88$ ) or the TBPQ ( $C_{48}H_{30}Br_4+$ ,  $m/z=925.92$ ). Figure 6.7b and c show spectra for samples for which the TBPB molecules were deposited at room temperature, and 200°C, respectively. The Au peak is detected for all the samples. For the sample prepared at room temperature a peak corresponding to the TBPB monomer is clearly resolved, but there is no evidence for TBPQ indicating that dimerisation does not occur under these conditions. The sample heated to 200°C shows a significant peak for the dimer confirming that the molecule identified in Fig. 6.6b is present on the surface and that it is formed by heating the Au substrate. For this sample we also observe a significant reduction in the monomer peak height to a value of order 10% of that observed for room temperature deposition experiments. This indicates that a substantial fraction of TBPB has been modified through conversion to TBPQ. Finally Figure 6.7d shows the spectra taken from a HOPG sample which has also

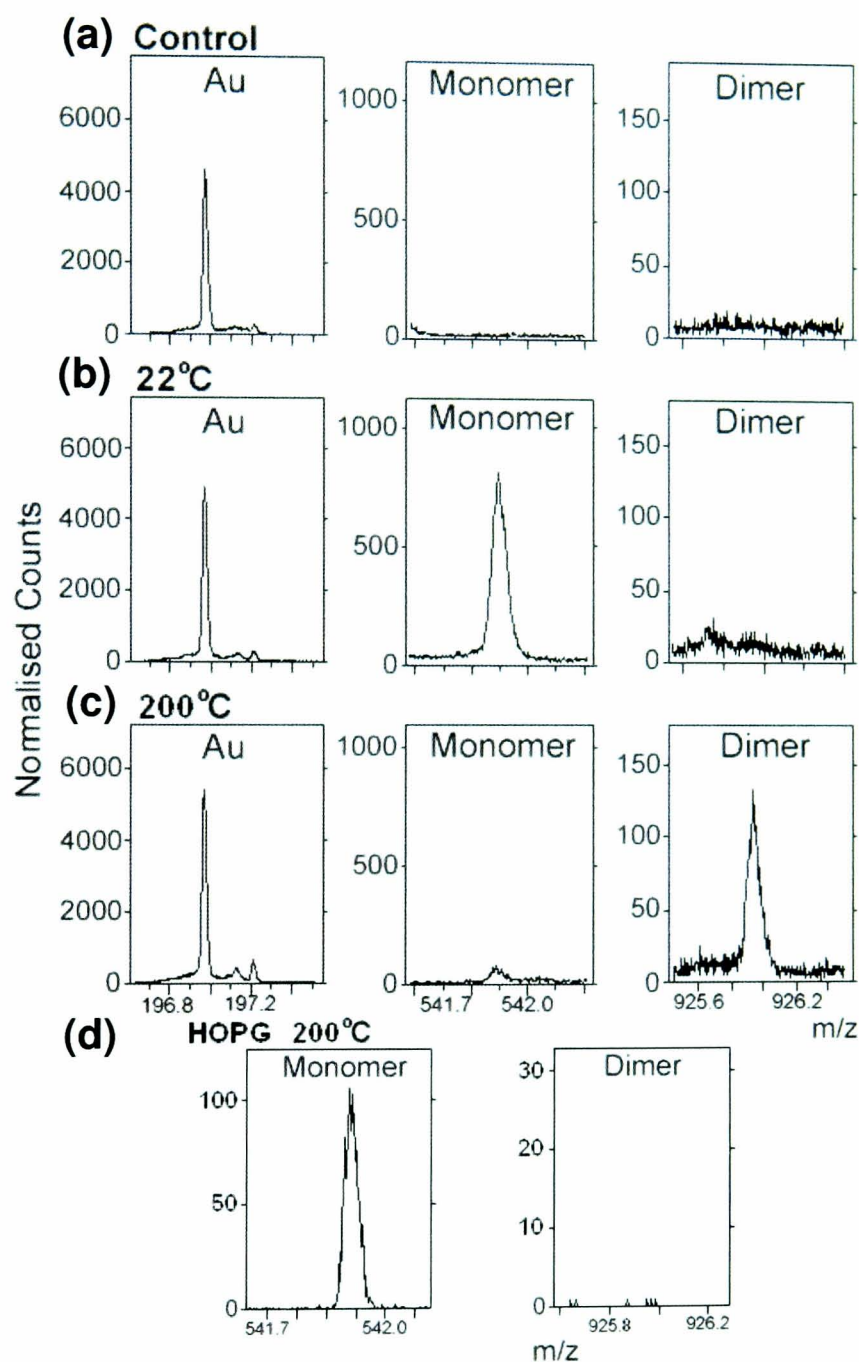


Figure 6.7: Secondary ion mass spectrometry of surfaces. Data shown for (a) a control Au sample exposed to ethanol whilst being heated to 200°C, (b) an Au sample with TBPB deposited at room temperature, (c) an Au sample with TBPB deposited at 200°C and (d) a HOPG sample with TBPB deposited at 200°C. The columns correspond to spectral data for Au (a-c only), the TBPB and TBPQ molecules. The data confirms that TBPQ formation arises from deposition on a heated Au substrate as discussed in the text.

been heated to 200°C prior to TBPB-ethanol deposition. This experiment was carried out to confirm that the gold substrate plays a role in the dimerisation of TBPB. A peak corresponding to the TBPB monomer can be clearly resolved from the spectra, however no peak is detected in the TBPQ mass region. Whilst this elegantly illustrates the importance of the substrate material and suggests that the gold atoms in the Au (111) surface play a catalytic role in TBPB dimerisation, the precise reaction procedure is still unknown.

We have also inspected the spectral regions which correspond to TBPB and TBPQ with attached gold atoms and/or with missing Br atoms. We have been able to identify small peaks corresponding to TBPB and TBPQ molecules with one Br atom missing. For the monomer the peak height was of the order of 30 counts for both the room temperature and 200°C sample. For the dimer the peak height corresponded to 20 counts and was present only in the 200°C sample. We have been unable to identify any other specific peaks corresponding to larger bonded species such as trimers. Our ToF-SIMS spectra specifically confirm that four Br atoms remain attached to TBPQ for the vast majority of molecules and only a relative small fraction undergo further fragmentation, for example through additional C-Br bond cleavage. In addition to this, no peaks corresponding to larger molecular species were found suggesting that only a very small number of TBPB molecules undergo more than one covalent bonding interaction.

## 6.4 Directing the adsorption of 1-adamantanethiols on Au (111)

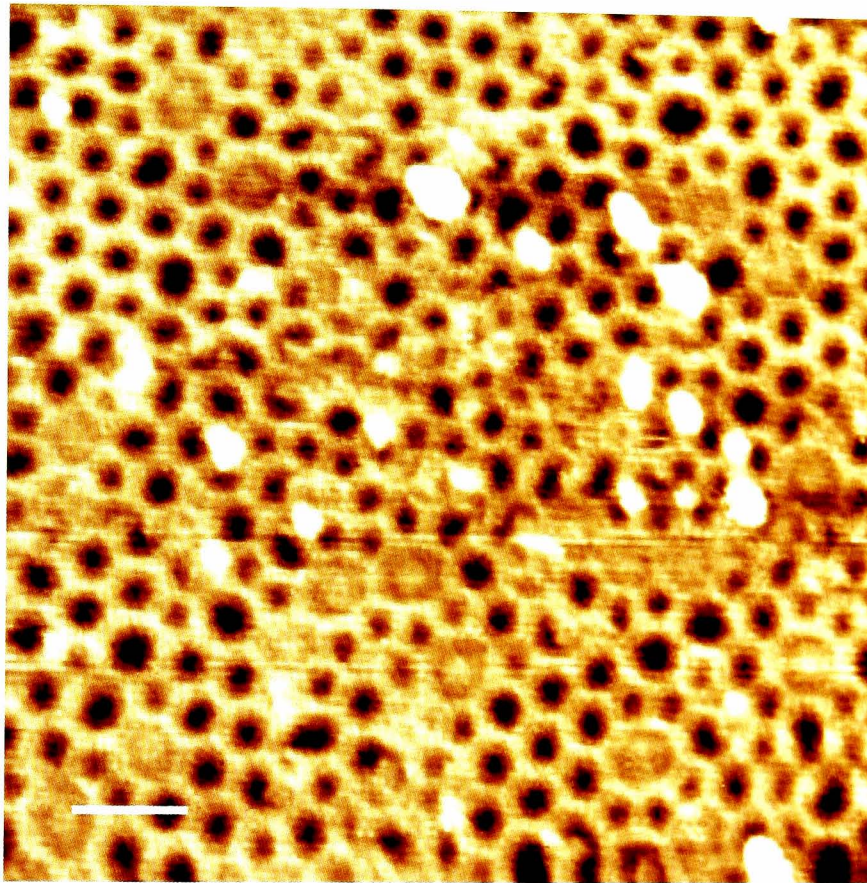


Figure 6.8: An STM image taken under UHV conditions of an extensively covalently-bound TBPB network. The image was taken at  $I = 20$  pA,  $V_{sample} = -2$  V. The scale bar is 5 nm.

In chapter 5 we discussed the changes induced in supramolecular networks caused by the introduction of additional molecular species. In this section we present the adsorption of 1-adamantanethiol molecules (Figure 6.9 inset) into a polymerised TBPB network. The adsorption of adamantane thiols on Au (111) has been studied before [107, 108, 109]. They have also been demonstrated to adsorb into strongly bound supramolecular structures [33]. For directing or templating thiol adsorption, it is critical that any molecular network is not

only strongly bound to the surface but has strong admolecule-admolecule interactions as well. Such binding is necessary as thiol molecules bind to the Au (111) surface through a sulphur gold metal coordination bond with an estimated binding energy of 160-200 kJmol<sup>-1</sup>[110, 111]. Such a strong guest-substrate interaction will simply disrupt any weakly bound supramolecular structure favouring the adsorption of more thiol molecules on the surface.

To template these thiol molecules, we utilise a completely covalently bonded TBPB network prepared under UHV conditions. Sample preparation and molecular deposition details can be found in our published work[102]. An example STM image is shown in Figure 6.8. The sample was removed from UHV conditions (in order for the liquid deposition of thiols) by venting the UHV chamber slowly to atmospheric pressure with nitrogen gas. High-resolution STM images showing both the template TBPB structure and the adsorbed adamantanethiol network at the same time could not be obtained under atmospheric conditions. We therefore demonstrate the directed adsorption of adamantanethiols into the TBPB polymerised network by the differences between a thiol network formed with and without the template structure.

### **6.4.1 Adsorption of 1-adamantanethiols on Au (111)**

To demonstrate the ordering of adamantanethiol molecules on the Au (111) surface, a thiol solution was prepared with approximately 1 mmol concentration and the sample submerged for ten seconds before being removed and washed in pure ethanol. The sample was then allowed to dry naturally. Figure 6.9 shows an example STM image of the resulting molecular network. The molecules appear as bright circular protrusions forming a hexagonally close-

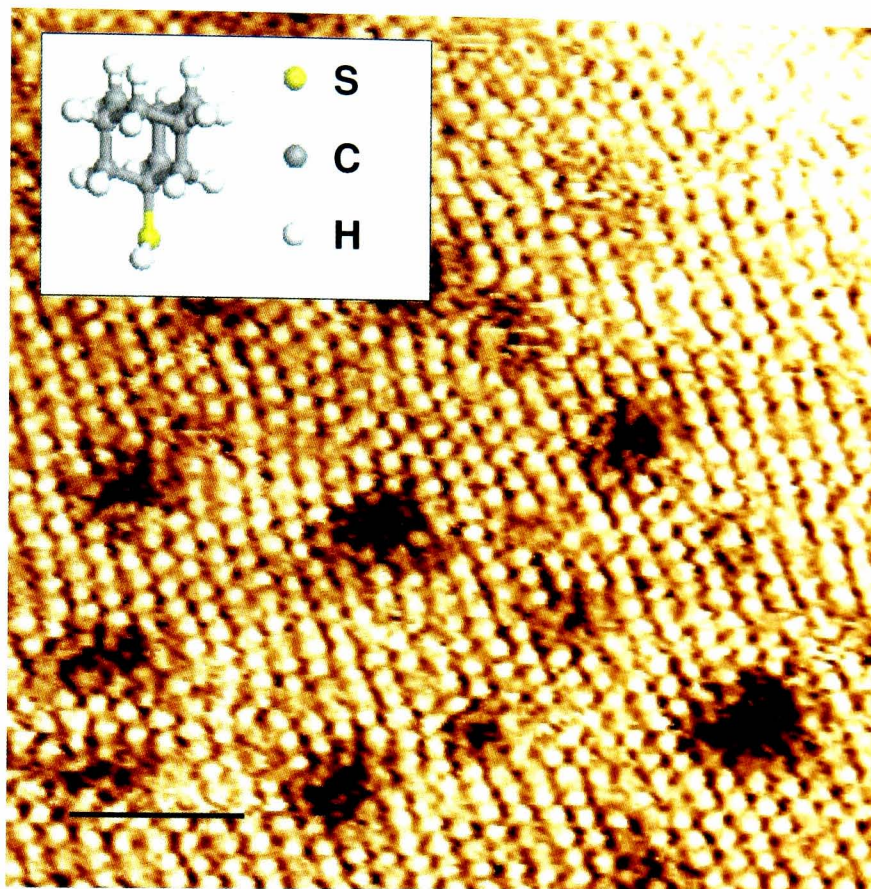


Figure 6.9: An image of adamantanethiols adsorbed on Au (111). Imaging parameters:  $I = 1$  nA,  $V_{tip} = 0.4$  V. The scale bar is 4 nm.

packed layer across the gold surface. Some darker regions of surface contrast are visible across the sample relating to lower areas of the gold surface[107]. The thiols bond to the surface through the sulphur group. The molecules then order to maximise the total number adsorbed on the surface as the admolecule-substrate bonding energy will be far in excess of any admolecule-admolecule contributions. We measure a nearest-neighbour molecular separation of  $6.5 \pm 0.8$  Å in agreement with values presented in the literature ( $6.9 \pm 0.4$  Å[109]).

### 6.4.2 Directed adsorption of 1-adamantanethiol molecules into the TBPB covalently-bound template network

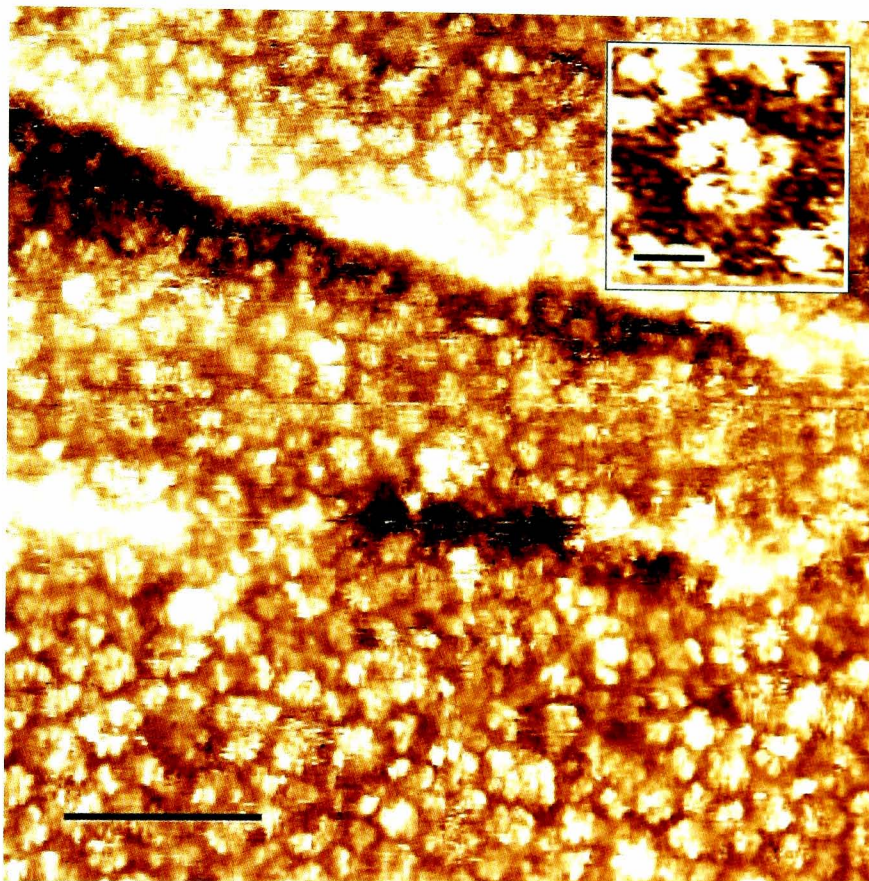


Figure 6.10: An imaging showing the adsorption of adamantanethiols into the TBPB network. The cellular nature of the network distinguishes it from a normal adamantanethiol structure suggesting the template network has directed the adsorption. The scale bar is 10 nm. A high resolution image of the network is shown in the inset (scale bar is 1 nm, STM Imaging parameters:  $I = 0.6$  nA,  $V_{tip} = 0.4$  V).

In Figure 6.8 we presented the template network formed by the surface-mediated bonding of TBPB molecules under UHV conditions. The porous nature of the network is clearly visible and we have demonstrated that it is suitable for hosting guest molecular species[102]. We deposit adamantanethiol molecules using a solution-based deposition technique as follows. A 1 mmol

solution of adamantanethiols dissolved in ethanol was prepared and the sample submerged in the solution for only 3 seconds before being washed in pure ethanol. The sample was then allowed to dry naturally after excess solvent had been removed. Once dried, 10  $\mu$ l droplet of 1-phenyloctance was deposited to improve the image quality. Images were then taken at the liquid-solid interface.

An example STM image of the network is shown in Figure 6.10. Despite the low image quality the cellular nature of the network is clearly visible through the ordering of the adamantanethiols. A higher resolution image is shown in the inset. Six adamantanethiol molecules can be observed adsorbed in the pore. The differences in the network morphology between a pure adamantanethiol network (Figure 6.9) and this one are clear. The cellular structure of Figure 6.10 is strongly suggestive that the covalently-bound TBPB template is directing the adsorption of the adamantanethiols as intended.

## 6.5 Summary

In summary, we have investigated the adsorption of a number of molecules on the Au (111) surface using solution-based deposition techniques using ethanol, and in one case butanol, as solvents. The close-packed phase formed by HATNA molecules is identified along with an apparent commensurability between two different relative adsorption geometries. A molecule with similar geometry but very different chemistry, namely TBPB, is subsequently presented. This molecule is observed to form two distinct close-packed phases on the Au (111) surface. In subsequent experiments we have utilised the chemical

properties of the molecule to trigger the covalent-coupling of TBPB molecules by heating the sample prior and during deposition to a series of elevated temperatures. On heating the substrate to 150°C we observe only relatively isolated incidences of covalent bonding involving only a few molecules at the edges of close-packed TBPB domains. Heating the sample to 200°C however results in the formation of extended domains of dimerised TBPB molecules in addition to previously observed close-packed phases. Finally we demonstrate the potential of the covalently-bonded TBPB network as a template by using a sample formed under UHV conditions with extended polymerised regions to nucleate the deposition of adamantanethiol molecules.

## Chapter 7

# Solubilised derivatives of perylene tetracarboxylic dianhydride adsorbed on graphite

*We have investigated the adsorption of a perylene tetracarboxylic dianhydride (PTCDA) derivative on to the highly-oriented pyrolytic graphite (HOPG) surface using STM. The molecule was deposited from 1-phenyloctane and imaged at the liquid-solid interface. The formation of the herringbone structure regularly formed by PTCDA is not observed as the additional propylthioether side groups inhibit the conventional weak hydrogen-bonding junction. A new structure therefore forms characterised by a single molecule unit cell which is stabilised through double C-H...O bonds. A model was derived from the experimental observations and its stability tested by density functional theory (DFT)*

*calculations.*

## **7.1 Introduction**

The molecule perylene tetracarboxylic dianhydride, PTCDA, has been widely studied as a prototype active material for organic electronic devices[10, 110]. PTCDA may be readily deposited by vacuum deposition and the properties of the resulting thin films have been investigated on a variety of different substrates including HOPG[13, 14], Ag(111)[112], Au(111)[11], Ag/Si(111)-( $\sqrt{3}\times\sqrt{3}$ )[12, 113, 9] and Cu(111)[114]. In recent studies the interest in sublimed monolayers of PTCDA has been extended through the demonstration of the covalent coupling of adsorbed PTCDA to a variety of amine compounds[15, 93, 115] leading to the identification of two-dimensional disordered polymers. This process is closely related to a reaction that occurs in the solution phase where the substitution of the anhydride group with an alkane chain attached via an imide group leads to a family of compounds which form one dimensional nanowires[18]. These imide derivatives are also very promising candidates as the active region of transistors and photovoltaic devices[116, 117, 118].

The addition of the imide-linked alkane chain promotes solubility of the resulting molecule but the anhydride group of the PTCDA is eliminated through this coupling. In fact, and despite the extensive literature describing the adsorption of PTCDA under vacuum conditions, there have been very few studies of solution deposition of PTCDA due to its limited solubility[119]. Nevertheless the controlled adsorption of arrays of molecules onto surfaces from a so-

lution phase has become increasingly relevant to the fields of nanoscience and nanotechnology for the purposes of fabricating small electronic devices and sensors[120, 121, 26].

In this chapter, we investigate the effect of a possible route to solubilising PTCDA which leaves intact the anhydride functionality and shows that such a modified derivative may be deposited on a substrate from solution. The solubility is increased by the introduction of a propyl chain attached to each side of the PTCDA molecule via a thioether link. The di(propylthio) perylene tetracarboxylic dianhydride (DPT-PTCDA) molecule is shown in Figure 7.1. In our work we use 1-phenyloctane as a solvent following the approach of Kaneda et al.[120] (these authors managed to acquire images of small domains of PTCDA on graphite, which we have had limited success in reproducing). Imaging of the molecule was performed using STM and took place at the liquid-solid interface and we propose a model for the structure derived from the experimental data and supported by density functional calculations.

## **7.2 Experimental details**

The DPT-PTCDA molecules were synthesised using the same procedure as summarised in previous work[74]. The molecules were dissolved in 1-phenyloctane (Sigma-Aldrich, 97% purity). The 1-phenyloctane/DPT-PTCDA solution was prepared as described in Chapter 3. 1-phenyloctane is a nonconductive solvent and has a sufficiently low vapour pressure as described in Section 3.6.2. The STM tip was therefore immersed in the solution droplet so that scanning took place *in-situ*, at the liquid-solid interface. All images

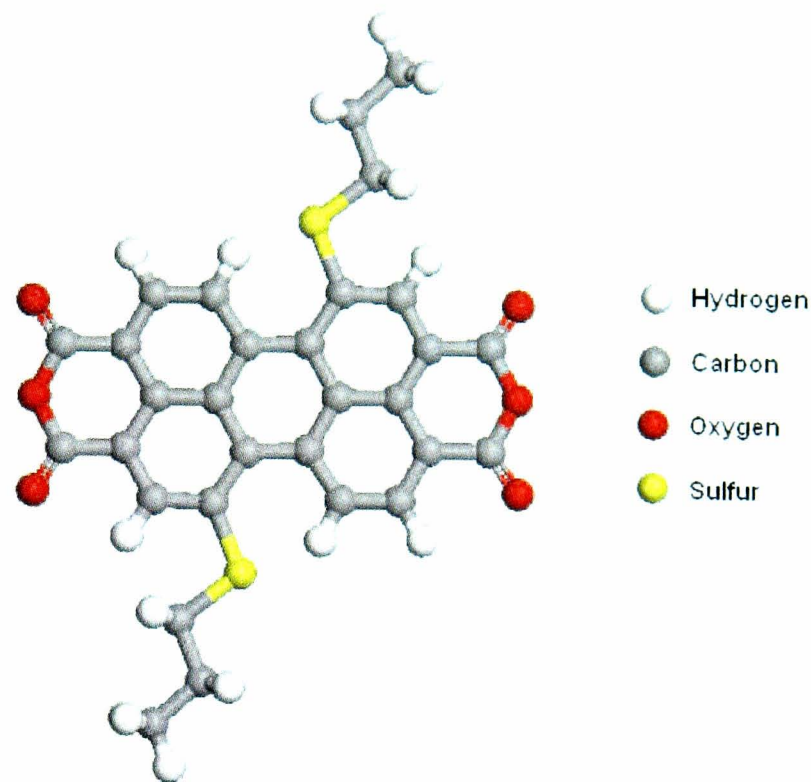


Figure 7.1: Schematic diagram showing the DPT-PTCDA molecule.

were taken at ambient temperature and pressure and acquired by operating the STM in constant current mode with positive tip bias.

### 7.3 The DPT-PTCDA network

Images of the DPT-PTCDA layer formed on the HOPG surface are shown in Figure 7.2. As can be seen from Figure 7.2a, the molecules form large, ordered domains with typical widths of  $\sim 100\text{nm}$  in size across greater than 80% of the surface. A periodic contrast variation can be observed across each of the DPT-PTCDA domains. The periodicity of this feature was measured from a number of scans taken in different directions and determined to be  $3.0 \pm 0.3\text{nm}$ . The contrast modulation is likely to be caused by the commensurability between the adsorbed layer and the underlying HOPG substrate, as previously reported[13.

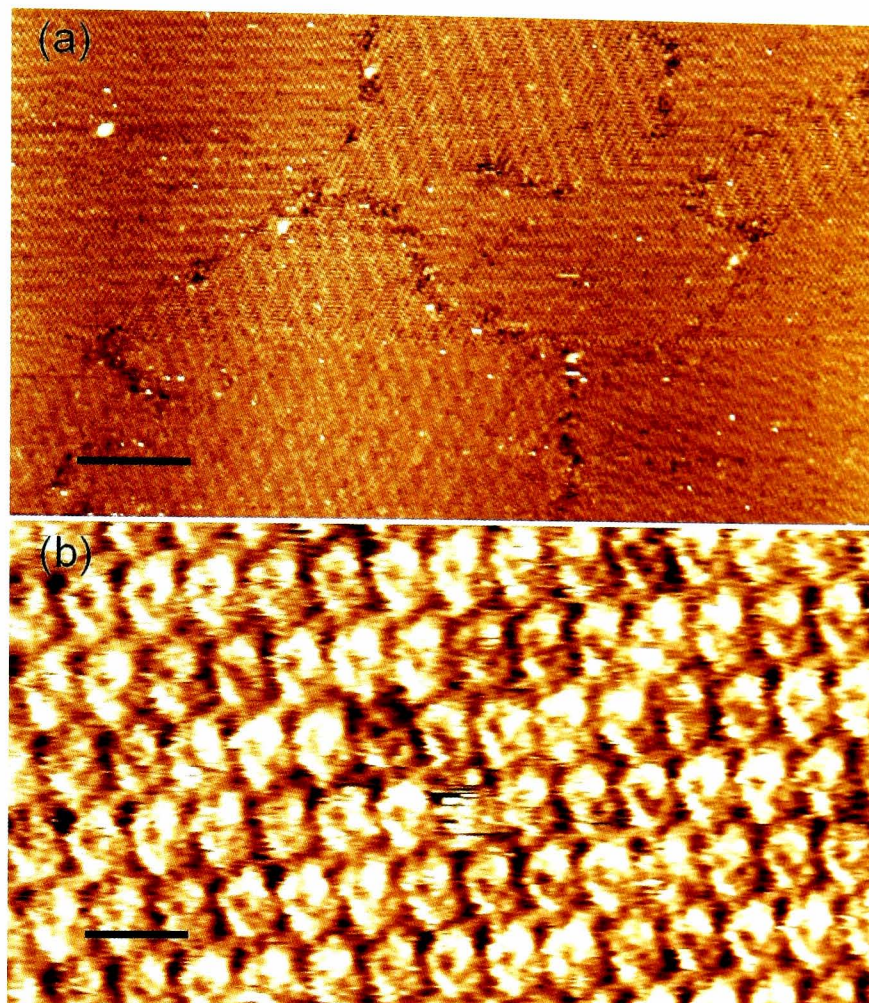


Figure 7.2: (a) An STM image of a DPT-PTCDA network on HOPG which demonstrates the size of the domains formed and the periodic contrast modulation. Scale bar 20nm. (b) A scan of the DPT-PTCDA network showing molecular contrast. Scale bar 2nm. Scanning parameters for both images: tunnel current,  $I = 30\text{pA}$ , tip voltage,  $V_{tip} = 1\text{V}$ .

14]. Figure 7.2b shows a smaller scan area of one of the domains where an ordered, repeating pattern can be observed. To better understand the images of the DPT-PTCDA layer, we computed the highest occupied molecular orbital (HOMO) of the DPT-PTCDA molecule by performing a density functional theory (DFT) calculation of the orbitals using the DMol<sup>3</sup> algorithm[122, 123]. An image of the HOMO of DPT-PTCDA produced by this calculation is shown in Figure 7.3a. The HOMO shown is similar to that presented by Swarbrick et al.[9] for PTCDA but with the addition of two lobes of probability amplitude

close to the sulfur atoms in the thioether groups. We propose that the sulfur atoms give rise to the small areas of higher conductance that appear as bright spots in the STM images. We therefore use the locations of these areas as a guide for determining the orientation of the molecules in the STM images, as shown in Figure 7.3b.

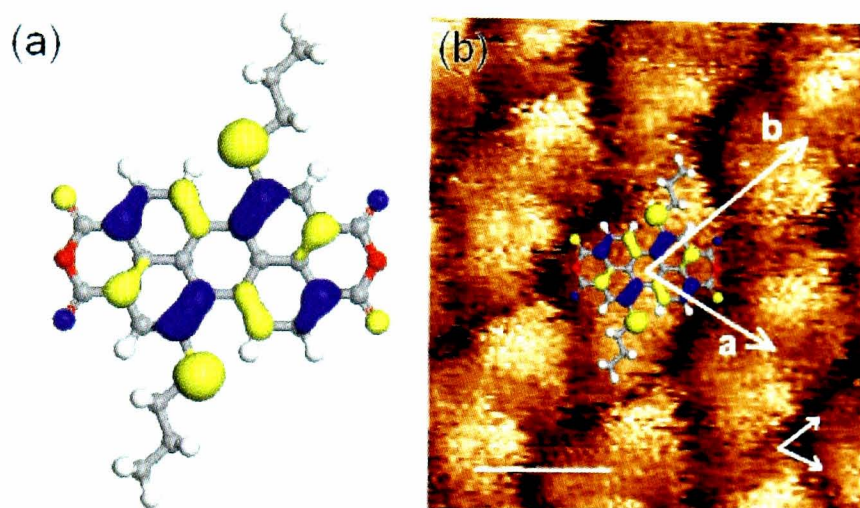


Figure 7.3: **(a)** Diagram showing the HOMO of the DPT-PTCDA molecule. **(b)** A diagram showing the HOMO of the DPT-PTCDA molecule overlaid onto an STM image ( $I = 60\text{pA}$ ,  $V_{tip} = 0.95\text{V}$ ) to illustrate the orientation of individual molecules in the network. The unit cell dimensions **a** and **b** are shown. Scale bar 1nm. The orientations of the graphite lattice vectors are shown as black arrows.

To compensate for thermal drift in the STM data, composite images containing both information about the adsorbed DPT-PTCDA layer and the graphite substrate were obtained. This was achieved by scanning the DPT-PTCDA layer with the appropriate tunnelling current and voltage and half way through the image changing the tunnel voltage to image the substrate beneath. Assuming that the thermal drift will be constant for the whole image, a measurement of the periodicity of the carbon atoms in the graphite substrate and subsequent comparison with the accepted values will determine the thermal drift. The drift can then be compensated for in measurements of

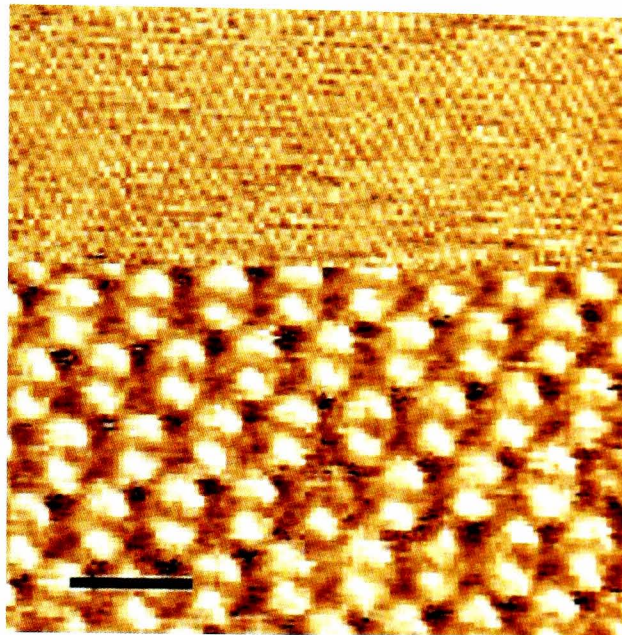


Figure 7.4: A composite image showing both the adsorbed DPT-PTCDA layer (bottom) and the graphite substrate (top) beneath. Image parameters: Bottom half at  $I = 60\text{pA}$ ,  $V_{tip} = 1\text{V}$ , top half at  $I = 60\text{pA}$ ,  $V_{tip} = 0.08\text{V}$ . The scale bar is 2nm.

the periodicity of the DPT-PTCDA layer. An example of such a composite image is shown in Figure 7.4. The image analysis was performed using the WSxM software[50]. The values for  $|\mathbf{a}|$  and  $|\mathbf{b}|$  were averaged from multiple split images taken in different scan directions of different areas of the monolayer, and were determined to be  $1.1\pm 0.1\text{nm}$  and  $1.3\pm 0.1\text{nm}$  respectively at angles of  $-16\pm 1^\circ$  and  $58\pm 3^\circ$  to one of the principal graphite axes.

A model of the DPT-PTCDA network is proposed as shown in Figure 7.5a. Within this model the molecules are predominantly stabilised by hydrogen bonding between the PTCDA-like cores of adjacent DPT-PTCDA molecules (as in Fig. 7.5b), and hydrogen bonding between the ends of the sidechains and the oxygen atoms (as in Fig. 7.5c). It has been well documented that 1-phenyloctane interacts only weakly with the HOPG substrate[119, 27], making the probability of the co-adsorption of solvent molecules unlikely and they are therefore omitted from the model.

In order to gain a better understanding of the stability of the proposed model, DFT calculations were performed using the DMol<sup>3</sup> package. Geometry optimisations were performed using the gradient-corrected functional (GGA) proposed by Perdew et al.[124] (PBE) and the double numerical plus polarisation (DNP) basis set was used for the orbitals. Simulations did not include any influence of the solvent or the substrate. The carbon, oxygen and sulfur atoms of all molecules in the simulation were constrained to be coplanar. This was to imitate the constraining effect of the surface on an adsorbed layer and to prevent the simulation from diverging due to the alkane side-chains coming out of a planar arrangement. Two geometry optimisations were performed to test the stability of each of the two principle hydrogen bonding junctions, illustrated in Figures 7.5b and 7.5c. These confirmed that both of these hydrogen bonding configurations are stable with binding energies determined to be -0.27eV and -0.20eV for Figure 7.5b and 7.5c respectively. The calculated values for  $|\mathbf{a}|$  and  $|\mathbf{b}|$  of 11.7Å and 13.9Å respectively, are in excellent agreement with the experimental results. We note also that our proposed arrangement is near close-packed so that there will be stabilisation due to van der Waals interactions in addition to the values calculated using this density functional approach.

## **7.4 Discussion and Conclusions**

Our results show that a large-area coverage of ordered PTCDA derivatives may be deposited from solution. The additional groups that promote solubility also have the effect of suppressing the interaction (between the anhydride

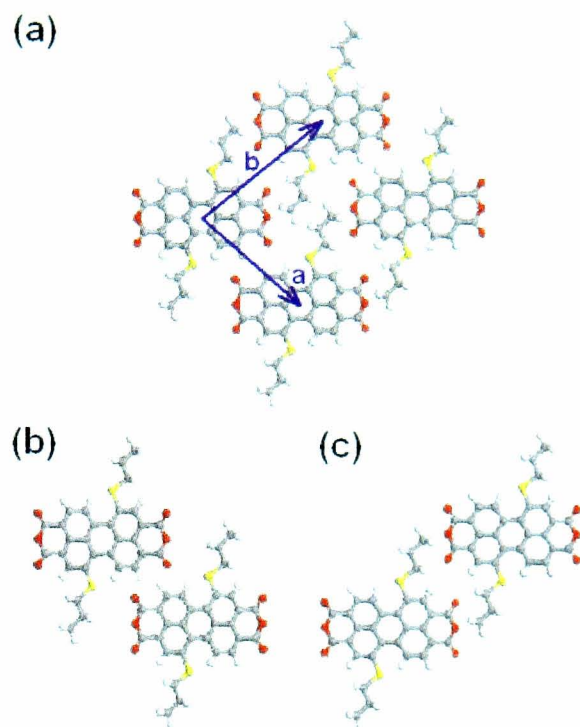


Figure 7.5: (a) Proposed model of DPT-PTCDA on HOPG. (b) The junction along the vector **a**. (c) The junction along the vector **b**.

group and the perylene core of a nearest-neighbour molecule) which stabilises the well-known herringbone configuration. This suppression can be understood as a simple steric effect and leads to the proposed configuration in which the perylene cores of the molecules within a given domain are all parallel. The formation of an adsorbed layer of a PTCDA derivative has not been previously reported for a PTCDA derivative and we conclude that the formation of this new structure is directly due to the presence of the alkane chain. In addition to van der Waals interactions the molecular arrangement is stabilised by hydrogen bonding between perylene cores (Figure 7.5b) and between the additional alkane chain and the anhydride group. The identification of the HOMO allows the S atom positions to be identified and underpins our model of the packing of DPT-PTCDA and its registry with the HOPG substrate.

PTCDA has a number of interesting properties though the poor solubility of

the molecule has limited solution-based studies. The new derivative of PTCDA which we report has propyl chains attached via thioether compounds to the sides of the PTCDA molecule, which, importantly, leaves the functionality of the anhydride group intact. This is particularly significant since it has been shown, in vacuum studies, that the anhydride group of PTCDA can act as a donor system in hydrogen bonded bimolecular junctions[113]. Hydrogen bonding has been widely studied as a route to the introduction and control of molecular order in two-dimensional molecular monolayers of sublimed perylene derivatives[32, 88, 125, 126]. More recently, this has been extended to solution deposition[33], but so far not for a derivative in which the anhydride group is present. We believe that the synthesis and properties of DPT-PTCDA will promote analogue studies of hydrogen bonding in a solution environment, including covalent coupling, and potentially, applications for organic electronic devices.

# Chapter 8

## Conclusions

This thesis has presented a series of studies into the supramolecular structures formed by a number of molecules. Understanding how these structures form is of critical importance if they are to be utilised to fabricate nanoscale architectures which can be used to direct the adsorption of guest molecular species. Such molecular templates are a desirable goal as in order to perform some experiments, guest species need to be isolated from one another. In Chapter 4 the deposition of two carboxylic acid species from nonanoic acid solutions on HOPG was shown. These molecules can form double hydrogen bonds with neighbours through the carboxylic acid moieties. The QPTC molecules form an ordered network where the quarterphenyl backbones arrange parallel to one another and molecules bond through four double carboxylic acid bonds. A periodic modulation of the molecular contrast is observed across domains of the network which is attributed to the relative adsorption positions of QPTC molecules with respect to the substrate. The second species TPTC forms a very different network. Whilst it has an underlying hexagonal symmetry of the

structure, there is no translational symmetry of the molecules. We characterise the morphology in terms of the orientation of the TPTC molecules around the network pores and subsequently by height and correlation functions utilised in theoretical discussions of lozenge rhombus tilings. The time-dependent evolution of the network is also studied. Topological defects corresponding to half adsorption site vacancies are observed to diffuse through the network causing a re-ordering of molecular orientations as they diffuse. Molecules at the edges of domains are observed to readily adsorb and desorb from the network leading to changes in the network morphology in these regions. Finally a technique for the tip-induced manipulation of the TPTC network is introduced. By scanning the network with a tip-specific range of voltage biases, the formation of a new close-packed phase of TPTC can be induced. The subsequent relaxation of these structures gives interesting insight to growth of molecular networks and the kinetic trapping of molecules in metastable conformations.

In Chapter 5 the concept of exerting control over molecular networks is developed by investigating the effect of the introduction of molecular guest species. We demonstrate that the introduction of coronene guest molecules to a preformed QPTC parallel network induces a change in the network morphology to a hexagonally ordered structure with the guest located at the vertices of QPTC molecules. We are able to restrict the conversion of the network morphology by the removal of the solvent and drying of the sample. The transition begins at the edges of QPTC domains as these molecules will have weaker binding to the bulk QPTC network. A similar structure is observed to form when perylene is used as the guest species. We then investigate the sequential deposition of coronene molecules into the TPTC network. The guest

preferentially adsorbs into the six-membered pore type, determined from gradually increasing the concentration. Little change in the network morphology is observed. However, when the molecules are deposited simultaneously we observe the non-uniform adsorption of coronene at low concentrations. At the higher concentrations a significant change in the network morphology occurs suggesting that in the sequential deposition case the network is kinetically trapped in the preformed structure.

In Chapter 6 we present studies of molecular adsorption on the Au (111) surface. HATNA molecules deposited from ethanol solutions are found to form stable supramolecular structures. Whilst a predominant bonding junction can be identified, the network appears to switch between two domain orientations. Straight lines parallel to one of the molecular unit cell vectors can be drawn separating domains. The adsorption of TBPB molecules is then presented. These molecules form three different phases on the Au (111) surface, one of which exhibits the same domain switching observed for HATNA molecules. To promote the covalent coupling of molecules through the bromine groups, the Au (111) surface is heated prior and during molecular deposition. For samples heated to 150°C, a number of individual bonding occurrences are observed with STM. At 200°C a new phase of the molecule formed comprised of covalently bonded TBPB dimers. ToFSIMS experiments show that a significant proportion of the TBPB are converted into dimers at 200°C. The dimers form by a surface-mediated aryl–aryl coupling reaction. The role of the substrate is clearly identified by a similar experiment using HOPG as the substrate which fails to show the presence of dimers. Finally an extensive covalently bound network formed under UHV conditions is shown to direct the formation of

adamantanethiol molecules deposited from solution.

The solution deposition of a solubilised PTCDA derivative is presented in Chapter 7. PTCDA molecules are particularly insoluble in solvents conventionally used for liquid STM experiments. By attaching alkane chains to the sides of the molecule, the solubility is greatly improved whilst leaving the anhydride functionality intact. Using 1-phenyloctane as a solvent, we demonstrate the adsorption of this PTCDA derivative on the HOPG surface. The presence of the alkane side chains inhibits the formation of the herringbone structure often observed for PTCDA. Instead the molecules form a new structure characterised by a single molecule unit cell which is stabilised through double C-H $\cdots$ O bonds.

# Bibliography

- [1] G. E. Moore, Electronics Magazine (1965).
- [2] R. P. Feynman, There's plenty of room at the bottom, 1959.
- [3] *Engines of Creation: The Coming Era of Nanotechnology* (Anchor Books, 1986).
- [4] D. M. Eigler and E. K. Schweizer, Nature **344**, 524 (1990).
- [5] J. Emsley, Chemical Society Reviews **9**, 91 (1980).
- [6] J. Sponer, J. Leszczynski, and P. Hobza, BIOPOLYMERS **61**, 3 (2001).
- [7] J. Venables, Surface Science **299**, 798 (1994).
- [8] J. V. Barth, G. Costantini, and K. Kern, Nature **437**, 671 (2005).
- [9] J. C. Swarbrick *et al.*, The Journal of Physical Chemistry B **109**, 12167 (2005).
- [10] S. R. Forrest, Chemical Reviews **97**, 1793 (1997).
- [11] I. Chizhov, A. Kahn, and G. Scoles, Journal of Crystal Growth **208**, 449 (2000).

- [12] J. B. Gustafsson, H. M. Zhang, and L. S. O. Johansson, *Physical Review B* **75**, 155414 (2007).
- [13] A. Hoshino, S. Isoda, H. Kurata, and T. Kobayashi, *Journal of Applied Physics* **76**, 4113 (1994).
- [14] C. Kendrick, A. Kahn, and S. R. Forrest, *Applied Surface Science* **104-105**, 586 (1996).
- [15] T. Wagner, A. Bannani, C. Bobisch, H. Karacuban, and R. Mller, *Journal of Physics: Condensed Matter* **19**, 056009 (2007).
- [16] R. Otero *et al.*, *Science* **319**, 312 (2008).
- [17] R. Kelly, Y. Lee, and L. Kantorovich, *Journal of Physical Chemistry B* **109**, 22045 (2005).
- [18] M. Treier, R. Fasel, N. R. Champness, S. Argent, and N. V. Richardson, *Physical Chemistry Chemical Physics* **11**, 1209 (2009).
- [19] M. Lackinger, S. Griessl, W. Heckl, M. Hietschold, and G. Flynn, *Langmuir* **21**, 4984 (2005).
- [20] M. Lackinger and W. Heckl, *Langmuir* **25**, 11307 (2009).
- [21] L. Kampschulte *et al.*, *Journal of the American Chemical Society* **130**, 8502 (2008).
- [22] L. Kampschulte *et al.*, *Journal of Physical Chemistry B* **110**, 10829 (2006).

- [23] S. Griessl, M. Lackinger, M. Edelwirth, M. Hietschold, and W. M. Heckl, *Single Molecules* **3**, 25 (2002).
- [24] S. Furukawa *et al.*, *Journal of the American Chemical Society* **128**, 3502 (2006).
- [25] J. Adisoejoso *et al.*, *Angewandte Chemie International Edition* **48**, 7353 (2009).
- [26] S. D. Feyter and F. C. D. Schryver, *Chemical Society Reviews* **32**, 139 (2003).
- [27] S. D. Feyter and F. C. D. Schryver, *The Journal of Physical Chemistry B* **109**, 4290 (2005).
- [28] A. S. Klymchenko *et al.*, *New Journal of Chemistry* **30**, 1420 (2006).
- [29] P. C. M. Grim, *Journal of Vacuum Science & Technology B: Microelectronics and Nanometer Structures* **15**, 1419 (1997).
- [30] K. Tahara *et al.*, *Journal of the American Chemical Society* **128**, 16613 (2006).
- [31] K. Tahara *et al.*, *Journal of the American Chemical Society* **131**, 17583 (2009).
- [32] J. A. Theobald, N. S. Oxtoby, M. A. Phillips, N. R. Champness, and P. H. Beton, *Nature* **424**, 1029 (2003).
- [33] R. Madueno, M. T. Raisanen, C. Silien, and M. Buck, *Nature* **454**, 618 (2008).

- [34] G. Binnig, H. Rohrer, C. Gerber, and E. Weibel, *Physical Review Letters* **49**, 57 (1982).
- [35] J. Tersoff and D. R. Hamann, *Physical Review Letters* **50**, 1998 (1983).
- [36] J. Tersoff and D. Hamann, *Physical Review B* **31**, 805 (1985).
- [37] J. Bardeen, *Physical Review Letters* **6**, 57 (1961).
- [38] N. D. Lang, *Physical Review Letters* **56**, 1164 (1986).
- [39] N. Lang, *Physical Review Letters* **55**, 230 (1985).
- [40] N. Lang, *Physical Review Letters* **58**, 45 (1987).
- [41] J. Wintterlin, H. Brune, H. Hofer, and R. Behm, *Applied Physics A-Materials Science and Processing* **47**, 99 (1988).
- [42] J. Lennard-Jones, *Transactions of the Faraday Society* **25**, 0668 (1929).
- [43] R. M. Feenstra and P. Martensson, *Physical Review Letters* **61**, 447 (1988).
- [44] R. Hamers, R. Tromp, and J. Demuth, *Physical Review Letters* **56**, 1972 (1986).
- [45] M. Crommie, C. Lutz, and D. Eigler, *Science* **262**, 218 (1993).
- [46] *Scanning Tunneling Microscopy* (Academic Press Inc., 1993).
- [47] C. Will, S. Chiang, R. J. Wilson, and P. H. Lippel, *Physical Review B* **39**, 7988 (1989).

- [48] J. V. Barth, H. Brune, G. Ertl, and R. J. Behm, *Physical Review B* **42**, 9307 (1990).
- [49] G. Albert, Physical vapour disposition - <http://www.georg-albert-pvd.de/index.html>.
- [50] I. Horcas *et al.*, *Review of Scientific Instruments* **78**, 013705 (2007).
- [51] D. N. Reinhoudt and M. Crego-Calama, *Science* **295**, 2403 (2002).
- [52] K. E. Maly, E. Gagnon, T. Maris, and J. D. Wuest. *Journal of the American Chemical Society* **129**, 4306 (2007).
- [53] M. Stohr, M. Wahl, H. Spillmann, L. H. Gade, and T. A. Jung, *Small* **3**, 1336 (2007).
- [54] H. Zhou *et al.*, *Journal of the American Chemical Society* **129**, 13774 (2007).
- [55] M. Lackinger, S. Griessl, T. Markert, F. Jamitzky, and W. M. Heckl, *The Journal of Physical Chemistry B* **108**, 13652 (2004).
- [56] K. Nath *et al.*, *Journal of Physical Chemistry C* **111**, 16996 (2007).
- [57] K. Nath *et al.*, *Journal of the American Chemical Society* **128**, 4212 (2006).
- [58] Y. Ye *et al.*, *Journal of Physical Chemistry C* **111**, 10138 (2007).
- [59] S. Stepanow, N. Lin, J. Barth, and K. Kern, *Chemical Communications*, 2153 (2006).

- [60] M. Simard, D. Su, and J. D. Wuest, *Journal of the American Chemical Society* **113**, 4696 (1991).
- [61] M. O. Blunt *et al.*, *Science* **322**, 1077 (2008).
- [62] X. Lin *et al.*, *Angewandte Chemie International Edition* **45**, 7358 (2006).
- [63] M. Blunt *et al.*, *Chemical Communications* , 2304 (2008).
- [64] M. Marschall *et al.*, *Nature Chemistry* **2**, 131 (2010).
- [65] H. W. J. Blote and H. J. Hilborst, *Journal of Physics A: Mathematical and General* **15**, L631 (1982).
- [66] R. Moessner, S. L. Sondhi, and E. Fradkin, *Physical Review B* **65**, 024504 (2001).
- [67] M. E. Fisher, *Physical Review* **124**, 1664 (1961).
- [68] D. B. Wilson, *The Annals of Applied Probability* **14**, 274 (2004).
- [69] H. Cohn, R. Kenyon, and J. Propp, *J. Amer. Math. Soc.* **14**, 297 (2001).
- [70] J. Linde, C. Moore, and M. G. Nordahl, *Discrete Mathematics and Theoretical Computer Science Proceedings* **23** (2001).
- [71] J. Garrahan, A. Stannard, M. Blunt, and P. Beton, *Proceedings of the National Academy of Sciences of the United States of America* **106**, 15209 (2009).
- [72] C. L. Henley, *Quasicrystals, the state of the art*, p. 459. World Scientific, Singapore, 1999.

- [73] L. M. A. Perdigao *et al.*, The Journal of Physical Chemistry B **110**, 12539 (2006).
- [74] L. M. A. Perdigao *et al.*, Chemistry - A European Journal **14**, 7600 (2008).
- [75] S. J. H. Griessl *et al.*, The Journal of Physical Chemistry B **108**, 11556 (2004).
- [76] S. J. H. Griessl *et al.*, Langmuir **20**, 9403 (2004).
- [77] D. Keeling, M. Humphry, P. Moriarty, and P. Beton, Chemical Physics Letters **366**, 300 (2002).
- [78] J. Teng, K. Wu, J. Guo, and E. Wang, Surface Science **602**, 358 (2007).
- [79] L. J. Whitman, J. A. Stroschio, R. A. Dragoset, and R. J. Celotta, Science **251**, 1206 (1991).
- [80] F. Silly *et al.*, Chemical Communications , 4616 (2008).
- [81] J. Lu *et al.*, The Journal of Physical Chemistry B **108**, 5161 (2004).
- [82] Z. Yang *et al.*, ChemPhysChem **6**, 65 (2005).
- [83] D. Wu, K. Deng, Q. Zeng, and C. Wang, The Journal of Physical Chemistry. B **109**, 22296 (2005), PMID: 16853903.
- [84] M. Blunt *et al.*, Nature Chemistry **3**, 74 (2011).
- [85] B. J. Gyarfas, B. Wiggins, M. Zosel, and K. W. Hipps, Langmuir **21**, 919 (2005).

- [86] S. Guo, D. P. Fogarty, P. M. Nagel, and S. A. Kandel, *The Journal of Physical Chemistry B* **108**, 14074 (2004).
- [87] H. Zhang *et al.*, *The Journal of Physical Chemistry C* **112**, 4209 (2008).
- [88] P. A. Staniec, L. M. A. Perdigo, A. Saywell, N. R. Champness, and P. H. Beton, *ChemPhysChem* **8**, 2177 (2007).
- [89] S. Barlow *et al.*, *Chemistry - A European Journal* **13**, 3537 (2007).
- [90] S. D. Ha, B. R. Kaafarani, S. Barlow, S. R. Marder, and A. Kahn, *The Journal of Physical Chemistry C* **111**, 10493 (2007).
- [91] S. Weigelt *et al.*, *Angewandte Chemie International Edition* **47**, 4406 (2008).
- [92] S. Weigelt *et al.*, *ACS Nano* **2**, 651 (2008).
- [93] M. Treier, N. V. Richardson, and R. Fasel, *Journal of the American Chemical Society* **130**, 14054 (2008).
- [94] L. Grill *et al.*, *Nat Nano* **2**, 687 (2007).
- [95] L. Lafferentz *et al.*, *Science* **323**, 1193 (2009).
- [96] J. A. Lipton-Duffin, O. Ivasenko, D. F. Perepichka, and F. Rosei, *Small* **5**, 592 (2009).
- [97] M. Matena, T. Riehm, M. Sthr, T. Jung, and L. Gade, *Angewandte Chemie International Edition* **47**, 2414 (2008).
- [98] M. I. Veld, P. Iavicoli, S. Haq, D. B. Amabilino, and R. Raval. *Chemical Communications* , 1536 (2008).

- [99] S. Hla, L. Bartels, G. Meyer, and K. Rieder, *Physical Review Letters* **85**, 2777 (2000).
- [100] M. Xi and B. E. Bent, *Journal of the American Chemical Society* **115**, 7426 (1993).
- [101] J. Cai *et al.*, *Nature* **466**, 470 (2010).
- [102] M. Blunt, J. Russell, N. Champness, and P. Beton, *Chemical Communications* **46**, 7157 (2010).
- [103] R. Gutzler *et al.*, *Chemical Communications* , 4456 (2009).
- [104] H. Walch, R. Gutzler, T. Sirtl, G. Eder, and M. Lackinger, *The Journal of Physical Chemistry C* **114**, 12604 (2010).
- [105] P. Metrangolo, F. Meyer, T. Pilati, G. Resnati, and G. Terraneo, *Angewandte Chemie International Edition* **47**, 6114 (2008).
- [106] C. J. Villagomez, T. Sasaki, J. M. Tour, and L. Grill, *Journal of the American Chemical Society* **132**, 16848 (2010).
- [107] C. Schoenenberger, J. A. M. Sondag-Huethorst, J. Jorritsma, and L. G. J. Fokkink, *Langmuir* **10**, 611 (1994).
- [108] J. Songaghuethorst, C. Schonenberger, and L. Fokkink, *Journal of Physical Chemistry* **98**, 6826 (1994).
- [109] A. A. Dameron, L. F. Charles, and P. S. Weiss, *Journal of the American Chemical Society* **127**, 8697 (2005).
- [110] F. Schreiber, *physica status solidi (a)* **201**, 1037 (2004).

- [111] J. C. Love, L. A. Estroff, J. K. Kriebel, R. G. Nuzzo, and G. M. Whitesides, *Chemical Reviews* **105**, 1103 (2005).
- [112] K. Glockler *et al.*, *Surface Science* **405**, 1 (1998).
- [113] J. Ma *et al.*, *The Journal of Physical Chemistry B* **110**, 12207 (2006).
- [114] N. Nicoara, Z. Wei, and J. M. Gomez-Rodriguez, *The Journal of Physical Chemistry C* **113**, 14935 (2009).
- [115] M. Treier *et al.*, *Nano Letters* **9**, 126 (2009).
- [116] A. L. Briseno *et al.*, *Nano Letters* **7** (2007).
- [117] A. J. Breeze *et al.*, *Applied Physics Letters* **81**, 3085 (2002).
- [118] P. R. L. Malenfant *et al.*, *Applied Physics Letters* **80**, 2517 (2002).
- [119] J. Y. Kim and A. J. Bard, *Chemical Physics Letters* **383**, 11 (2004).
- [120] Y. Kaneda, M. E. Stawasz, D. L. Sampson, and B. A. Parkinson, *Langmuir* **17**, 6185 (2001).
- [121] F. Rosei *et al.*, *Progress in Surface Science* **71**, 95 (2003).
- [122] B. Delley, *The Journal of Chemical Physics* **92**, 508 (1990).
- [123] B. Delley, *The Journal of Chemical Physics* **113**, 7756 (2000).
- [124] J. P. Perdew, K. Burke, and M. Ernzerhof, *Physical Review Letters* **77**, 3865 (1996).
- [125] W. Chen *et al.*, *Journal of the American Chemical Society* **130**, 12285 (2008).

*List of figures*

---

- [126] M. Stohr *et al.*, *Angewandte Chemie International Edition* **44**, 7394 (2005).

# List of Figures

1.1	The IBM logo written with Xe atoms . . . . .	3
2.1	Guanine-Cytosine hydrogen bonding junction . . . . .	9
2.2	Illustrations of sigma and pi bonds . . . . .	11
2.3	Illustrations of networks formed when kinetic and thermodynamic growth effects dominate . . . . .	16
2.4	Images of PTCDA and PTCDI networks . . . . .	18
2.5	The adsorption of TMA on HOPG . . . . .	20
2.6	Structures formed by a DBA derivative . . . . .	22
3.1	A 1D Finite Quantum Barrier . . . . .	27
3.2	Energy level diagrams of two materials brought into electrical contact . . . . .	28
3.3	Illustrations of the Agilent 4500 series SPM . . . . .	35
3.4	Schematic of a piezoelectric scan tube . . . . .	37
3.5	STM feedback mechanisms . . . . .	38
3.6	The Atomic structure of HOPG . . . . .	43
3.7	The Atomic structure of HOPG . . . . .	44
3.8	An alternative contrast of atomically resolved HOPG . . . . .	45

3.9	An image of the Au (111) Surface . . . . .	47
3.10	Nonanoic Acid adsorbed on HOPG . . . . .	50
3.11	Molecular structure of ethanol and butanol . . . . .	51
3.12	Molecular structure of phenyloctane . . . . .	52
4.1	Carboxylic acid dimer . . . . .	60
4.2	Atomic structure of the TPTC and QPTC molecules . . . . .	61
4.3	An STM scan of the QPTC network . . . . .	63
4.4	FFT enhancement of the QPTC network . . . . .	64
4.5	Schematic of QPTC adsorption on HOPG . . . . .	65
4.6	An STM image of the impure QPTC network . . . . .	66
4.7	An STM image of the TPTC network . . . . .	68
4.8	The two bonding geometries of TPTC . . . . .	69
4.9	Figure illustrating the different TPTC pore types . . . . .	70
4.10	The conversion from STM image to rhombus tiling . . . . .	72
4.11	The scheme for height function determination . . . . .	73
4.12	Rhombus tiling of a 100x100 nm <sup>2</sup> image and its corresponding height function . . . . .	74
4.13	The Correlation Function for the TPTC network . . . . .	76
4.14	Illustration of possible defect creation mechanisms and defect diffusion . . . . .	79
4.15	Images showing the creation of a molecular vacancy . . . . .	81
4.16	Images of an edge of the TPTC network . . . . .	82
4.17	Analysis of the network re-structuring at a domain edge . . . . .	83
4.18	Images of showing the disruption of the TPTC network . . . . .	85

4.19	The close-packed TPTC structure . . . . .	86
4.20	Sequential Scans showing TPTC close-packed relaxation . . . . .	87
4.21	Graphs showing TPTC close-packed relaxation against time . . . . .	88
5.1	The Guest molecular species . . . . .	95
5.2	The QPTC-coronene network . . . . .	96
5.3	STM images of a dried network . . . . .	99
5.4	QPTC-perylene network . . . . .	101
5.5	DFT simulations of perylene adsorption . . . . .	102
5.6	A high resolution scan of the QPTC-coronene network . . . . .	103
5.7	Scans of the TPTC-coronene network . . . . .	105
5.8	Schematic diagrams of the different TPTC pore types . . . . .	106
5.9	Scans showing the non-homogenous adsorption of coronene . . . . .	110
5.10	STM scans and height functions of the TPTC-coronene network . . . . .	112
6.1	HATNA molecules on Au(111) . . . . .	117
6.2	HATNA bonding junction . . . . .	118
6.3	Line defects in the HATNA structure . . . . .	118
6.4	The phases of TBPB on Au (111) . . . . .	123
6.5	Phase 1 extended structure . . . . .	124
6.6	The dimerisation of TBPB . . . . .	125
6.7	ToFSIMS data confirming the dimerisation of TBPB . . . . .	128
6.8	The TBPB porous covalent network . . . . .	130
6.9	Adamantanethiols on Au (111) . . . . .	132
6.10	Adamantanethiols adsorbed in the TBPB network . . . . .	133
7.1	DPT-PTCDA structure . . . . .	139

*List of figures*

---

7.2	STM data of adsorbed DPT-PTCDA molecules . . . . .	140
7.3	HOMO of DPT-PTCDA as calculated by DFT simulations . . .	141
7.4	STM scan of the DPT-PTCDA and underlying substrate . . . .	142
7.5	DFT simulations of the different DPT-PTCDA bonding ar- rangements . . . . .	144